SHEAR INDUCED MIXING AND SELF-ORGANIZATION IN IMMISCIBLE ALLOYS DURING SEVERE PLASTIC DEFORMATION

BY

SALMAN NOSHEAR ARSHAD

DISSERTATION

Submitted in partial fulfillment of the requirements
for the degree of Doctor of Philosophy in Materials Science and Engineering
in the Graduate College of the
University of Illinois at Urbana-Champaign, 2014

Urbana, Illinois

Doctoral Committee:

Assistant Professor Shen Dillon, Chair
Professor Robert Averback
Professor Pascal Bellon
Professor Jian-Min Zuo

ABSTRACT

Metals and alloys processed by severe plastic deformation (SPD) techniques are gaining widespread interest for applications where bulk nanostructured materials are desired. This dissertation research focuses on understanding the underlying mechanisms and evolution of the microstructure in Cu-Ag, an immiscible alloy, during SPD. The two key features of SPD processing that will be presented are shear induced chemical mixing of alloying elements at room temperature and self-organization at elevated temperatures. Shear induced mixing mechanism in a moderately immiscible system is often attributed to the glide of dislocations but the details of how such dislocation glide effects mixing remains an unresolved issue. Self-organization in an immiscible system is a result of the competition between shearing induced mixing and thermally induced phase separation. Understanding the effects of temperature and shearing rate during processing by SPD is limited which hinders the validation of relevant models. In this thesis, a combination of high energy ball milling (BM) and high pressure torsion (HPT) experiments are performed on a model Cu-Ag system between room temperature and 400 °C at strain rates ranging from 0.1 to 6.25 s^{-1}. Characterization of the shear induced mixing and self-organization is carried out by X-ray diffraction (XRD), scanning electron microscopy (SEM), transmission electron microscopy (TEM), and atom probe tomography (APT). The experimental results support the prediction of a 'superdiffusive' model for shear induced mixing in Cu-Ag system, where the dissolution rate of particles is controlled by the rate of dislocation glide across interfaces. Moreover, the steady state Ag sizes during self-organization at elevated temperatures exhibited limited strain rate dependence and

low apparent activation energy (0.39 eV). At 400 °C, shear enhanced diffusion is observed at highest deformation rates. The results suggest that shear induced vacancies play a dominant role during self-organization.

To

Kiran, Ahmed, Ali & Soha

ACKNOWLEDGMENTS

I would like to thank my advisor Professor Shen J. Dillon and co-advisor Professor Robert S. Averback for providing me an opportunity to work in the field of nanostructured alloys. Their expert advice and guidance was always there to help me throughout the progress of this thesis. In addition, I thank the other dissertation committee members, Professor Pascal Bellon and Professor Jian-Min Zuo, for their inputs and feedback.

I thank our collaborators, Mohsen Pouryazdan and Dr. Julia Ivanisenko at Karlsruhe Institute of Technology, Germany, and Dr. Daria Setman at University of Vienna, Austria, for helping with the high pressure torsion experiments. I also acknowledge the Northwestern University Center for Atom Probe Tomography (NUCAPT) for use of their facility and Timothy Lach for doing the experiments there. I would also like to acknowledge the National Science Foundation for providing the funding support to carry out this research. I am also grateful to Fulbright program of Institute of International Education (IIE) and United States Educational Foundation in Pakistan (USEFP) for funding me initially for my graduate studies in University of Illinois.

I also acknowledge the staff members of Center of Microanalysis of Materials at University of Illinois who have been very helpful in training and use of the advanced characterization facilities. I would like to thank Miao Wang, Elvan Ekiz, and Shimin Mao with whom I constantly discussed issues and challenges faced in this research. Moreover,

I thank Dr. Nhon Vo, Dr. Daniel Schwen, and Dr. Fuzeng Ren with whom I had very useful discussions The company of other colleagues and friends, Ke, Yin, Bo, Lin, and Kyong, Sezer, Brad, Xuan, made my graduate life fun and joyful.

Finally, I am grateful to my beautiful wife, Kiran, and my three lovely kids, Ahmed, Ali and Soha, who made my stay in USA very enjoyable and comfortable and gave me great happiness. Moreover, my parents and siblings have always encouraged me throughout this thesis and I thank them for their prayers and unyielding support.

TABLE OF CONTENTS

LIST OF ABBREVIATIONS

SPD	Severe Plastic Deformation
BM	Ball Milling
ARB	Accumulative Roll Bonding
ECAP	Equal Channel Angular Pressing
HPT	High pressure torsion
KMC	Kinetic Monte Carlo
fcc	Face Centered Cubic
Cu	Copper
Ag	Silver
Co	Cobalt
Fe	Iron
Ta	Tantalum
Mo	Molybdenum
Nb	Niobium
Ni	Nickel
GPa	Giga Pascal
MD	Molecular Dynamics
3D	Three Dimensional
MC	Monte Carlo
bcc	Body Centered Cubic
V	Vanadium
MSRD	Mean Square Relative Displacement
XRD	X-ray Diffraction
EDX	Energy Dispersive X-ray Spectroscopy
DSC	Differential Scanning Calorimetry
STEM	Scanning Transmission Electron Microscopy
SEM	Scanning Electron Microscopy
RD	Radial Direction
ND	Normal Direction
TD	Transverse (shear) Direction
TEM	Transmission Electron Microscopy
APT	Atom Probe Tomography
Si	Silicon
SAED	Selected Area Electron Diffraction Pattern
HAADF	High Angle Annular Dark Field
LEAP	Local Electrode Atom Probe
FIB	Focused Ion Beam
NUCAPT	Northwestern University Center for Atom-Probe Tomography
Ga	Gallium

LIST OF SYMBOLS

K	Kelvin
$\dot{\varepsilon}$ or $\dot{\gamma}$	Strain rate
Ω	Short range order parameter
c	Number fraction of atoms
N_i^j	Average number of nearest neighbors of type j around atoms of type
D_{shear}	Diffusion caused by shear induced atomic displacements
$D_{thermal}$	Diffusion caused by thermally activated jumps
ϕ	Forcing parameter
D_{eff}	Effective diffusion coefficient
σ^2	Mean square relative displacement
R	Pair separation distance
Δt	Time interval
R_{ij}	Distance between atoms i and j
t_k	Particular time of instant
N	Number of atoms in the system/simulation cell
$R_{p,i}$	Initial particle radius
$D_{p,i}$	Initial particle diameter
n_p	Number density of precipitates
g	Geometrical factor
b	Magnitude of the Burgers vector
π	pi
Γ_{sh}	Frequency of dislocation glide OR shear induced atom jump frequency
A	Interfacial area
V_p	Volume fraction of precipitates/particles
C_B	Molar fraction of precipitates/particles
$\Delta\varepsilon_{dis}$	Characteristic strain to mix/dissolve
ΔH_m	Heat of mixing
R_n	Precipitate radius for the initial configuration with *n* precipitates
γ_e	Characteristic experimental strain for mixing
R_{ss}	Steady state length scale or pair separation distance
Å	Angstrom
T	Temperature
η	Ratio of the frequency of shear induced atomic jumps to the frequency of thermally activated jumps
eV	Electron volt
kJ	Kilo joules
at. %	Atomic percent
L_g	Glide length of the dislocation
C_v^{ss}	Vacancy concentration at the steady state
Γ_v	Vacancy jump frequency
C_v	Vacancy concentration

C_{sat}	Maximum vacancy concentration that a solid can support
C_v^{th}	Equilibrium thermal vacancy concentration
D_{therm}^{p}	Thermal pair diffusion coefficient
D_{shear}^{p}	Shear induced pair diffusion coefficient
F_{vac}	Number of vacancy jumps per unit time
d^3	Number of atoms in the computational cell
a_o	Nearest neighbor distance
Ψ	Production rate of the excess vacancies
σ	Stress
Ω_o	Atomic volume
Q_f	Vacancy formation energy
ζ	Neutralization effect of vacancy emitting and vacancy absorbing jogs
c_j	is the concentration of thermal jogs
C_{ex}	Excess vacancy concentration
D_v	Vacancy diffusivity
Λ	Annihilation rate of vacancies
ρ	Dislocation density
L	Grain size or size of the computational cell
κ	Describes the distribution of dislocations ($\kappa = 1$ for homogeneous distribution and $\kappa = 10$ for a cell-like substructure)
C_{ss}	Steady state excess vacancy concentration
ρ_{ss}	Steady state dislocation density
ε or γ	Shear strain
r	Radial distance on the HPT sample
n	Number of cycles of HPT
t	Thickness of the HPT sample at a given radial position
σ_y	Yield strength
σ_o	Intrinsic yield stress
k	Strengthening coefficient
mol	Mole
μm	Micrometer
T_a	Annealing temperature
°C	Degree centigrade
Pa	Pascal
rpm	Revolutions per minute
L_p	Particle length
kV	Kilo volt
mA	Milli ampere
D	Average crystallite size estimated from XRD
κ	Dimensionless shape factor crystallite size measurement from XRD
β	Full width at half maximum of the XRD peak
λ	X-ray wavelength

θ	Bragg angle
$\bar{l}$	Total length of the chord divided by the number of intersecting grain boundaries
ω	Shape factor used in calculation of grain radius by linear intercept method
H	Hardness
P_{max}	Maximum load during nanoindentation
$A(h_c)$	Tip area function
h_c	Contact depth during nanoindentation
h_{max}	Maximum indent depth
S	Stiffness

CHAPTER 1

INTRODUCTION

1.1. MOTIVATION

Nanostructured metals and alloys have been widely studied in recent decades owing to their potential to exhibit superior properties and performance as compared to their coarse-grained equivalents. These materials are promising for use in a broad range of applications ranging from biomedical to structural applications. Nanostructured metals and alloys are polycrystalline materials with microstructural features less than 100 nm in size. Nanostructural design is particularly attractive for developing new high-strength alloys, which are inherently strong due to the high density of grain boundaries and interfaces [1,2,3,4,5]. This strengthening results from the interfaces serving as barriers to dislocation motion. This grain size effect on strength is expressed by the well-known Hall-Petch relationship [6,7] which shows that the strength increases linearly with the inverse square root of the grain size. This relationship has been demonstrated for a wide variety of metals and alloys with grain sizes from micrometer down to few tens of nanometer length scales. However, it has been shown by computer simulations [8] and experiments on pure Copper [9] that below a certain grain size inverse Hall-Petch relationship maybe observed which means strength saturates or decreases with decreasing grain size. This softening is attributed to the greater grain boundary dislocation activity as

compared to the interior of the grain. This behavior may impose an upper limit on how strong nanocrystalline metals and alloys can become.

The relative simplicity of the single phase materials make them ideal for investigation of the basic mechanisms associated with their processing, structure and performance. These materials have received the most attention in the literature, with much of the experimental effort focused on idealized thin film samples. The potential for application of bulk nanostructured materials increases significantly if multi-phase alloys are utilized. Interfaces in multiphase alloys can then be tailored with greater flexibility to obtain specific properties [10]. Nanostructuring of multiphase thin film alloys has also been investigated in a number of model systems that are typically produced by thin film deposition methods. Nanostructure design in bulk two-phase materials, however, has been slower to develop and their processing remains a challenge.

Severe plastic deformation (SPD) has attracted practical interest as it offers a simple yet efficient means to synthesize nanostructured alloys with highly non-equilibrium microstructural and chemical constituents [11,12,13]. SPD is a “top-down” processing technique in which a typically coarse-grained metal or alloy is subjected to a high amount of shear strain resulting in nanometer scale grain sizes. The evolution to the nanometer sized grains is complex but typically involves dislocation generation and multiplication, formation of dislocation cells and sub-grains, and their transformation to high angle grain boundaries [12,13]. Historically, the most popular approach to the SPD processing is the high-energy ball milling (BM) [14,15,16] which has been successfully

used to process a variety of nanostructured metals and alloys. BM easily accesses high strains and is simple and inexpensive. However, BM is a powder processing technique which cannot be used for fabricating bulk metals and alloys. Also, critical information about the total strain and strain rate cannot be defined easily in these experiments. Precise knowledge of the process parameters is likely to be important for both understanding the fundamental mechanisms for nanostructure development during SPD and subsequently engineering alloys with predictable microstructure and properties. Experimentally validated fundamental models for interpreting and predicting nanostructure evolution during SPD are still lacking.

1.2. SCOPE AND AIMS OF THIS DISSERTATION

This dissertation research focuses on understanding the underlying mechanisms and evolution of the microstructure during processing of bulk nanocomposite alloys by SPD under controlled processing conditions. This thesis focuses on two of major aspects of processing by SPD; forced chemical mixing of alloying elements and self-organization during thermodynamic relaxation [17,18,19]. Forced chemical mixing refers to the athermal relocation of atoms induced by sustained shear deformation [20,21,22] which can force an otherwise immiscible system to mix. There has been a number of simulation studies on shear induced mixing in systems with different properties such as heat of mixing, lattice mismatch, crystalline and interface structure, et cetera, but a detailed experimental study to investigate these models is still lacking. Self-organization describes the development of compositional inhomogeneities that select a particular length scale

that is the steady state of the system under given processing conditions such as temperature and shearing rate. Self-organization is possible in immiscible systems where the two mechanisms of shearing and thermal diffusion of vacancies act in competition, shearing tends to homogenize the alloy while thermally activated diffusion tends to order it. These self-organized nanostructures have the potential to improve the performance where high strength is desired. Moreover, the high interfacial area and defect density present in these materials can trap point defects, for example, during irradiation.

The goal of this PhD thesis research is to experimentally study these two processes and advance the science of processing of nanostructured metal alloys by SPD. The first part of this dissertation research focuses on the mechanisms of shear induced mixing and how well it is predicted by previous MD simulations and model predictions. A second related question is which strain paths do model systems follow to mix immiscible phases with low heats of mixing. For example, simple shear strain will elongate the particle in the direction of the shear but the occurrence and nature of instabilities during particle elongation, the degree of co-deformation, and the role of grain boundaries and triple lines are not well understood. The third aspect of the research focuses on the role of shearing rate and temperature on the length scales of self-organization and how well it can be controlled. The mechanical properties of these nanostructured alloys will also be investigated briefly to emphasize the potential of this route of processing for making ultra-high strength alloys.

This thesis is organized as follows. First, the background knowledge is provided about shear induced mixing and self-organization in metal alloy systems with emphasis on experiments and simulation results in Chapter 2. Next, the details of the experimental procedures used in this thesis are presented in Chapter 3. In Chapter 4 and 5, the results of shear induced mixing and self-organization are presented, respectively. Finally, the thesis is concluded in Chapter 6.

1.3. REFERENCES

[1] Chokshi, A.H., A. Rosen, J. Karch, and H. Gleiter, Scripta Metallurgica, 1989. 23(10): p. 1679-1683.

[2] Schuh, C.A., T.G. Nieh, and H. Iwasaki, Acta Materialia, 2003. 51(2): p. 431-443.

[3] Nieman, G.W., J.R. Weertman, and R.W. Siegel, Scripta Metallurgica, 1989. 23(12): p. 2013-2018

[4] Dao, M., L. Lu, R.J. Asaro, J.T.M. De Hosson, and E. Ma, Acta Materialia, 2007. 55(12): p. 4041-4065.

[5] Suryanarayana, C., Advanced Engineering Materials, 2005. 7(11): p. 983-992.

[6] E.O. Hall, Proceedings of the Physical Society of London Section B 64 (1951) 747-753.

[7] N.J. Petch, Journal of the Iron and Steel Institute 174 (1953) 25-28.

[8] J. Schiotz, F.D. Di Tolla, K.W. Jacobsen, Nature 391 (1998) 561–563.

[9] C.E. Carlton, P.J. Ferreira, Acta Mater. 55 (2007) 3749–3756.

[10] Koch, CC, R.O. Scattergood, K.L. Murty, JOM (2007) 59, p. 66-70.

[11] R. Z. Valiev, N. A. Krasiinikov and N. K. Tsenev, Materials Science and Engineering A137 (1991) 35-40.

[12] R.Z.Valiev ,T.G.Langdon,Prog.Mater. Sci. 51 (2006) 881.

[13] R.Z.Valiev, R.K.Islamgaliev and I.V.Alexandrov, Prog Mater Sci 45 (2000) 103

[14] Gilman PS, Benjamin JS. Annu Rev Mater Sci 1983;13:279.

[15] Ma E, Atzmon M. Mater Chem Phys 1995;39:249.

[16] Suryanarayana C. Prog Mater Sci 2001;46:1.

[17] Martin, G. and P. Bellon, Driven alloys, in Solid State Physics - Advances in Research and Applications, Vol 50. 1997, Academic Press Inc: San Diego. p. 189-331.

[18] J. Ye, J.-wen Liu, R. a. Enrique, P. Bellon, Scripta Materialia 49 (2003) 969-975.

[19] P. Bellon and R. Averback, Scripta Materialia 49, 921-925 (2003).

[20] C.C. Koch and J.D. Whittenberge, Intermetallics 4, 339-355 (1996).

[21] F. Delogu, M. Pintore, S. Enzo, F. Cardellini, V. Contini, A. Montone, V. Rosato, Philosophical Magazine 76 (1997) 651-662.

[22] P. Bellon, R. Averback, Physical Review Letters 74 (1995) 1819-1822.

CHAPTER 2

BACKGROUND

Nanostructured metals and alloys processed by severe plastic deformation (SPD) techniques such as high energy ball milling (BM), accumulative roll bonding (ARB), equal channel angular pressing (ECAP), wire drawing, or high pressure torsion (HPT) are gaining widespread interest for applications where bulk nanostructured materials are desired [1]. All these processes are well known to refine the microstructure to nanometer length scales [2]. Nanostructured materials processed by SPD can be termed as 'driven systems' [3] if they are forced into a non-equilibrium state. An alloy is termed as 'driven' when it is subjected to a sustained external forcing so that the alloy components and defects (e.g. dislocations) are forced to move "ballistically" which means these movements are not affected by thermodynamic considerations. These materials remain in nonequilibrium conditions as a result of the steady state reached by the sustained external forcing and such materials are thus called 'driven systems'. One example of a driven system is a single or multi-phase metal/alloy subjected to SPD by a process such as in high energy BM [4,5,6,7,8]. In this case, the continuous fracturing and shearing is the sustained external forcing. BM is a 'top-down' powder processing technique, which typically uses hardened steel balls in a high speed vibrating or rotating steel vial to continuously mechanically weld, fracture and re-weld powder particles. This process is capable of achieving a number of outcomes that otherwise are not possible by other techniques e.g. refining the microstructure to sub-micron length scales [9],

homogeneously dispersing the second phase particles in a matrix [10], triggering chemical reactions at low temperatures [11], synthesizing novel crystalline and quasi-crystalline phases [12], forming amorphous phases [13], and extending solid solubility limits in immiscible systems [14]. Processing of nanostructured materials by SPD is reviewed in detail by Valiev et al. [15,16,17].

During SPD, the solid solubilities can potentially be extended as much as to completely mix and homogenize the system. The atoms during such a process are forced to move down their concentration gradients. For a miscible system, increased thermal diffusion by vacancy jumps at elevated temperatures also contributes to atomic mixing. However, in an immiscible system these two mechanisms act in competition; shearing tends to homogenize the system by forcing atoms to move down their concentration gradients, whereas, thermal diffusion tends to phase separate them by forcing atoms to move down their chemical potential gradients. In order to study such driven systems these two competing mechanisms can be decoupled to develop models for each in isolation. The relative rates of these two competing events will dictate the final steady state of the system. G. Martin [18] introduced a forcing parameter which is simply the ratio of the forced atomic jump frequency to the thermally activated vacancy jump frequency. How these external forcing conditions affect the steady state microstructural evolution is not well studied experimentally. In the absence of external forcing, thermodynamic considerations alone can predict the microstructural evolution; however, the theoretical framework needs to be modified to account for external forcing conditions in driven systems. Moreover, such driven systems can potentially be relaxed in a

controlled way to tune the steady state microstructures. One way of relaxing is through thermal diffusion, which can cause chemical decomposition and phase separation.

This dissertation research is an experimental investigation of the use of SPD as the external forcing mechanism to study the microstructural evolution in immiscible alloys under controlled shearing rate and temperature. In particular, the focus will be on the two key features of processing of nanostructured metal alloys by SPD; (1) forced chemical mixing of alloying elements and (2) self-organization [19,20,21]. Forced chemical mixing refers to the athermal relocation of atoms induced by sustained shear deformation [22,23,24,25]. Self-organization here means the development of compositional inhomogeneities that select a particular length scale that is the steady state of the system. Self-organization is possible in immiscible systems where the two mechanisms of shearing and thermal diffusion of vacancies act in competition, shearing tends to homogenize the alloy while thermally activated diffusion tends to phase separate it.

The effect of these two competing mechanisms on the final microstructure was studied by Kinetic Monte Carlo (KMC) simulations almost two decades ago [25] in a face center cubic (fcc) $A_{50}B_{50}$ alloy by changing the shearing rates at 400 K as illustrated in the Figure 2.1. In these simulations the atomic planes are randomly shifted along (111)<110> slip systems while a vacancy is allowed to diffuse. The rate of exchange of the vacancy with the neighboring atom is governed by the standard rate theory [26]. The time between the two shearing events was randomly chosen to give a desired average shearing frequency. At low shearing rates the interface roughens but the alloy remains macroscopically phase separated. At high shearing rates the system homogenizes.

However, at intermediate strain rates the system exhibits nanoscale compositional patterning at a length scale which may be controlled by varying the strain rate and temperature. The use of rigid lattice and constant vacancy concentrations used in this simulation makes it difficult to compare the results to real systems; nevertheless, the results are promising for tuning the microstructure by changing the relative contribution of these two atomic jump events. Such a scheme provides new control variables that can be used to tune the microstructures of engineering materials at nanometer length scale. Shear induced mixing and self-organization will be discussed in the next two sections with emphasis on identifying the underlying mechanisms and key unknowns. The role of shear-induced vacancies during high temperature deformation will also be highlighted.

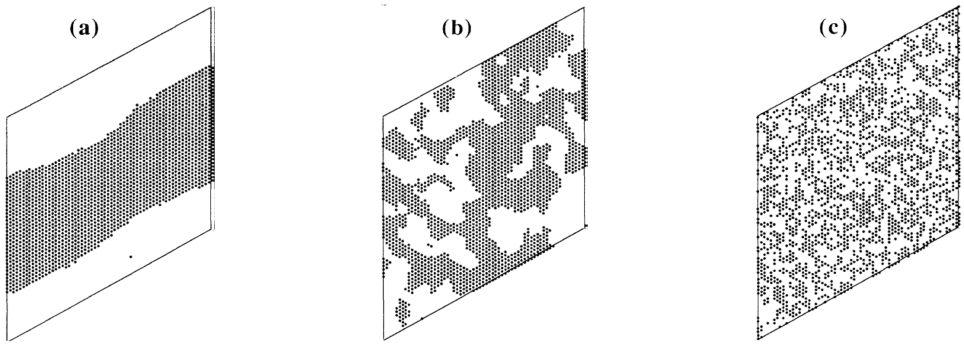

Figure 2.1. Typical steady-state microstructures observed for strain rates of (a) $\dot{\varepsilon} = 1s^{-1}$, (b) $\dot{\varepsilon} = 1000\ s^{-1}$, and (c) $\dot{\varepsilon} = 100{,}000\ s^{-1}$ when planes are shifted along (111)<110> slip system in a fcc $A_{50}B_{50}$ alloy and vacancies are allowed to diffuse at 400 K. (Black discs for B atoms) [25].

2.1. SHEAR INDUCED MIXING IN HETEROGENEOUS SYSTEMS

Sustained shear deformation is known to force the mixing of chemical constituents in many immiscible alloy systems. The mechanism explaining this mixing

behavior is often attributed to the glide of dislocations across interfaces. For example, Cu and Ag, which are immiscible, can be forced to mix by dislocation glide [25] given that the deformation occurs at low enough temperatures to suppress the phase separation by thermal diffusion. Full solid solutions have been experimentally reported in a number of systems, for example in Cu-Ag [27,28], Cu-Co [29], and Cu-Fe [30,31] systems when subjected to SPD at low temperatures. The initial explanation of mixing in such systems was based on the ballistic atom relocations during sustained shear deformation. This means that most binary systems can be forced to mix into homogeneous solid solutions if the thermal diffusion is suppressed. However, some immiscible systems such as Ni-Ag [32], Cu-Ta [33], Cu-Mo [34], Cu-Nb [35] and Ag-Fe [36] showed very limited solid solubilities even after milling them at cryogenic temperatures approaching 100 K. This indicates that the shear induced mixing is not truly ballistic in such systems and other factors need to be accounted.

A number of reasons have been proposed for the lack of shear induced mixing in certain alloys highlighted above even though they are subjected to high energy BM for extended periods of time. One simple argument is that the plastic strain is localized in one of the phases and the two phases are not co-deformed [37]. This is due to quite dissimilar shear moduli; for example, 30 and 80 GPa for Ag and Ni, respectively, and 42 and 122 GPa for Cu and Mo. Although such driven systems are under non-equilibrium conditions, some authors have suggested that equilibrium properties, such as heat of mixing, could prevent complete mixing in some immiscible systems [4,38]. Thermal diffusion is also suggested to control phase separation even at low temperatures [39]. A review [4] of different material systems subjected to high energy BM suggests that such

considerations can be important but a systematic understanding does not exist. In a recent experimental study [40], Wang et al. made significant improvements in the current understanding of limited shear induced mixing by showing in the ternary Ag-Cu-Ni system that localization of plastic strain and thermal diffusion do not account for limited enhancements in solubilities in Ag-Ni system but rather it is driven by chemical bias in the atomic exchanges by shearing.

2.1.1. Shear induced mixing studied by molecular dynamics (MD) simulations

Several authors [41,42] have used 3D MD simulations to study the effect of heat of mixing, lattice mismatch, and interface characteristics of a binary A-B alloy to shed light on the factors influencing the shear induced mixing. Odunuga et al. [41] used MD simulation to study the response of a binary 3D crystalline alloy subjected to sustained plastic deformation at low temperatures. Four different initial states were used; (1) B precipitate in A-matrix, (2) A precipitate in B-matrix, (3) Random, and (4) $L1_2$ Ordered. These different initial configurations allowed studying the effect of the initial state on the final state because if the final state is a true steady state of the system under given sustained external forcing then it shouldn't matter if the initial state was completely phase separated or random or an intermediate.

A short range order parameter, Ω, was used to study the microstructural evolution in these systems under sustained shearing. This parameter was originally used by Lund and Schuh to study the microstructural evolution in 2D binary alloys under shearing at low temperatures [43]. Ω is defined as:

Eq. 2-1 $$\Omega = \frac{\frac{c}{1-c}N_A^B + \frac{1-c}{c}N_B^A}{N_A^A + N_B^B} - 1$$

where c is the number fraction of A atoms, and N_i^j are the average number of nearest neighbors of type j around atoms of type i (i,j = A or B). This parameter varies from -1 for fully decomposed structure to 0 for a random alloy to positive values for chemically ordered structures; therefore, it allows to easily distinguish between these three states and their intermediates.

All alloys were subjected to cyclic compressive strains of ~24 % along the normal of the faces of the simulation cell. Figure 2.2(a) shows the result of the evolution of **Ω** with time for different initial configurations. Details of the initial configuration and results can be found in Ref. [41]. The main conclusion of this MD simulation study was that a large positive heat of mixing and a large lattice mismatch alone cannot account for the limited forced chemical mixing and that the only case where mixing is restricted is when the plastic deformation is localized in one phase possibly due to the quite different shear moduli. To study the mechanism of mixing, all nearest neighbor atoms were identified at a certain time and their pair separation distance was recalculated at a later time. Figure 2.2(b) shows the histogram of change in the pair separation distance for run no. 3 when an appropriate initial time and interval is selected. It shows a first and second peak at around 1.4 Å and 2.5 Å, respectively. Interestingly, these distances correspond to the modulus of burgers vector of $\frac{1}{6}\langle 112\rangle$ partial and $\frac{1}{2}\langle 110\rangle$ perfect dislocations, respectively. The inset in Figure 2.2(b) shows the precipitate in yellow cut by partial (green) and perfect dislocations (red). Moreover, slip was observed to initiate at precipitate-matrix interface by half loops which expanded either side of the interface.

Misoriented precipitates generally resulted in different slip systems being activated in the matrix and the precipitate causing dislocations to pile up at the interface. This can change the relative orientation of the precipitate. It was shown that slip is mostly restricted to the matrix for the run no. 4 because of the substantial difference in the shear modulus of the matrix and the precipitate.

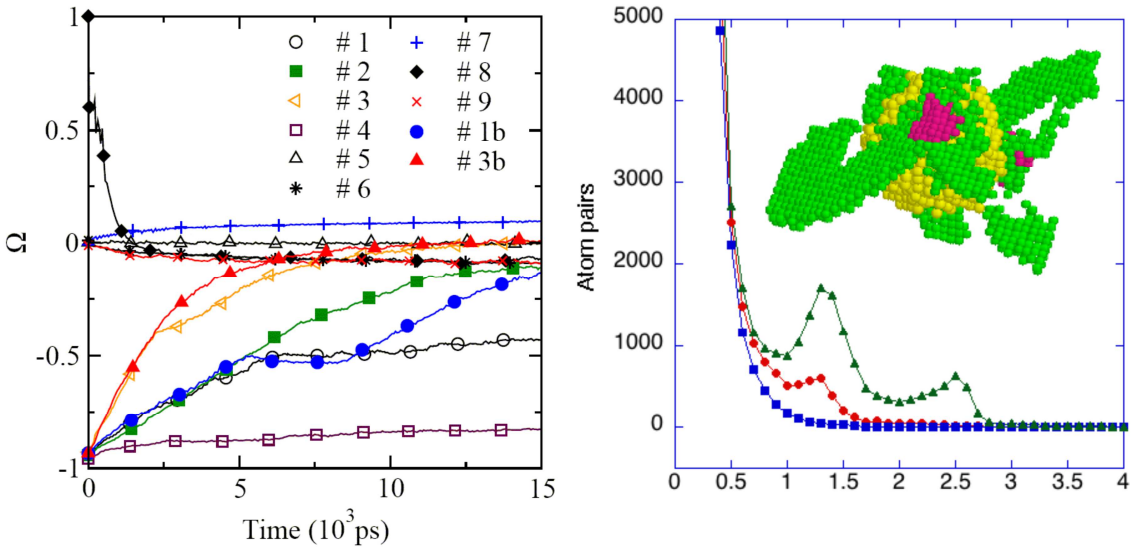

Figure 2.2. (a) Evolution of the chemical short-range order parameter Ω for different alloy systems. The details of the different run numbers can be found in Ref. [41]. (b) Histogram of the change in separation distance of atoms that were first nearest neighbors at t =5 ps, recorded at 6 ps (square), 8 ps (circle) and 15 ps (triangle), for run No. 3. The inset displays, at 8 ps, the *B* atoms of the precipitate in yellow, the pairs of atoms belonging to the peak near 1.4Å in green and to the peak near 2.5Å in red.

The effect of the difference in the tetragonal shear moduli between the two phases on the amount of chemical mixing was also studied by MD simulation in another study [44]. It was found that when the difference is greater than a certain threshold value the chemical mixing is greatly restricted. They also showed that when the difference in the

tetragonal shear moduli is not too great the initial strain hardening of one phase can make the difference smaller resulting in co-deformation during the later stages of shearing. This was also observed in the MD simulations discussed below.

Other factors such as the role of crystal and interface structures were studied by Ashkenazy et al. [42] using MD simulations on various two phase alloys. The samples were deformed cyclically by biaxial compression with strain of 20 % in each cycle. For reference and starting with a very simple case, atomic mixing in a single component fcc metal was studied under the assumption that dislocations do not interact with each other and the grain boundaries. Because of such simplicity, a KMC simulation approach similar to [25] was employed. An initial spherical precipitate of pure Cu in a pure Cu matrix (representing a single component system) becomes distorted after a strain of 6 with little chemical mixing representing a rough interface. At strains of 60 it completely mixes and homogenizes as shown in Figure 2.3 (top-left figures in a & b marked as MC). MD simulation for pure Cu also showed very similar results as the MC simulations. The similarity between the two simulation methods suggests that the shear induced mixing in homogeneous systems is not greatly influenced by the details of the shearing process as long as slip occurs on the multiple slip systems.

Next, shear mixing of fcc precipitates were studied by introducing Ag and Ni spherical precipitates in Cu matrix. Ni and Cu have very similar lattice sizes and a very small heat of mixing. However, shear modulus of Ni is considerably higher than that of Cu. Ag and Cu, on the other hand, have very different lattice sizes and have a moderate heat of mixing. The shear modulus of Ag is considerably smaller than that of both Cu and Ni. Figure 2.3(a & b) shows that the qualitative mixing behavior of these two systems is

quite similar. In contrast to fcc precipitates, the bcc precipitates in Cu show quite different mixing behavior as shown by the morphologies in Figure 2.3(a &b) for Fe, V, and Nb precipitates. V and Nb precipitates show very limited mixing because they are hardly deformed during shearing and maintain their spherical morphology even after strains of 60. Fe, on the other hand, shows very little mixing initially (similar to V and Nb) but experiences considerable shearing during the later stages. It was noted that the Fe particle forms fcc coherent interface with Cu when strain in each cycle exceeds 15 % which allows the dislocations to cut through the interface easily. Another observation is that an amorphous region forms around Nb and V precipitates (more pronounced in Nb) but not around Fe due to the small size misfit of Cu-Fe system.

The observations in Figure 2.3 qualitatively highlight the difference in the mixing behavior of fcc versus bcc precipitates in a Cu matrix. For fcc precipitates in a fcc matrix, the dislocations can easily cut through the interface promoting mixing, whereas with a bcc precipitates this doesn't happen. While chemical mixing happens in both systems, it is far more efficient in the former. The quantitative analysis of mixing will be discussed in the next section and how it can be experimentally studied.

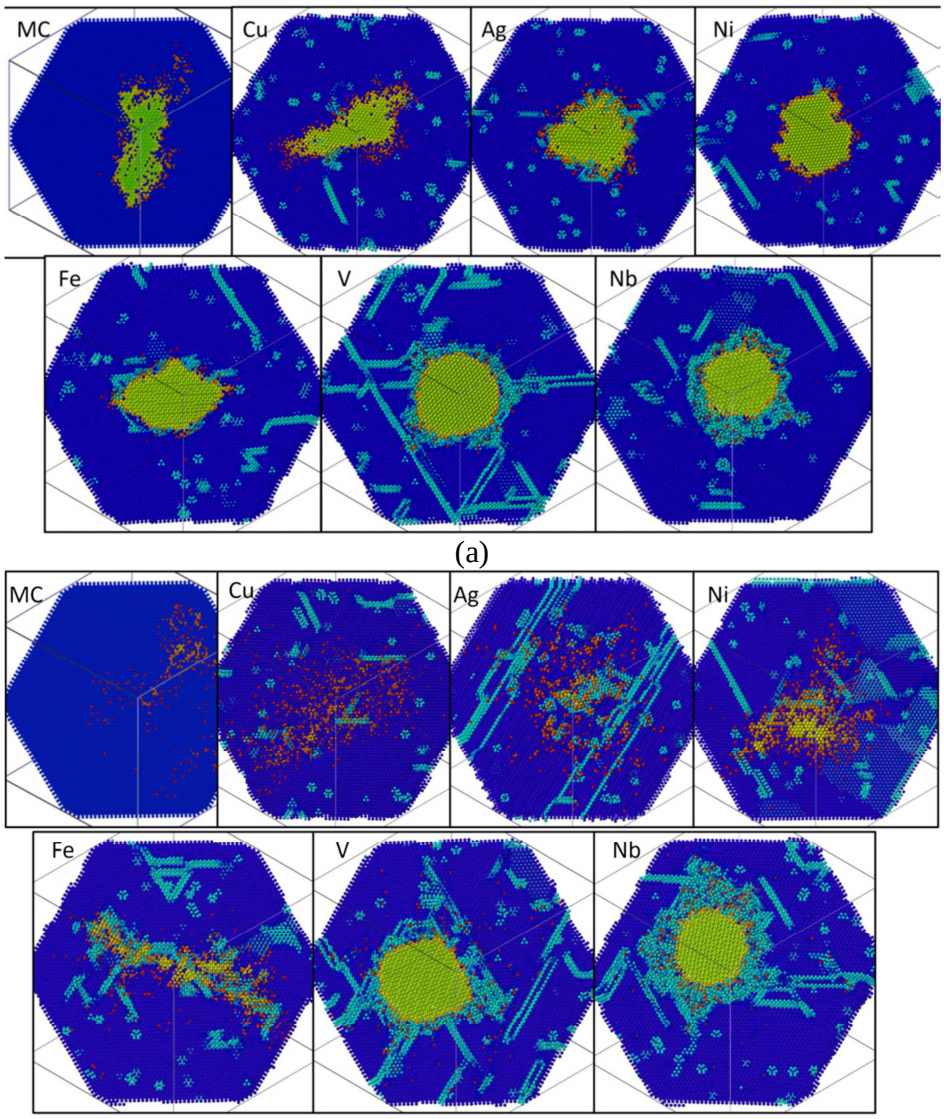

Figure 2.3. (a) Morphology of spherical particles in Cu after a strain of 6.0. The left-most configuration is from a MC simulation of a Cu precipitate in a Cu matrix. The rest of the configurations are from MD simulations of precipitates in a Cu matrix. The particle material is indicated in each panel. Color indicates the structural factors for the matrix atoms; blue are fcc atoms and gray are atoms positioned in a locally non-pure fcc environment (e.g. a stacking fault or next to a point defect). For the particle atoms color indicates local mixing; green indicates that most of the neighbors are from the particle and red indicates that most atoms are from the matrix. (b) Same as (a) but after a strain of 60.

2.1.2. Quantitative analysis of shear induced mixing

The steady state microstructures of systems under sustained external forcing depend on the relative strength of the external forcing versus thermally activated jumps [18]. The external forcing in case of SPD is the shearing frequency. The forcing parameter, thus, can also be written as the ratio of the transport caused by shearing only (D_{shear}) to the diffusion caused by thermally activated jumps ($D_{thermal}$) [45]:

Eq. 2-2 $$\phi = \frac{D_{shear}}{D_{thermal}}$$

D_{shear} relates to the relative motion of the atoms by shearing along deformation slip planes. If the pair separation distances are R_i and R_f at times t_i and t_f, then an effective diffusion coefficient can be written as

Eq. 2-3 $$D_{eff} = \frac{\partial \sigma^2(R,\Delta t)}{12 \partial \Delta t}$$

where $\sigma^2(R,\Delta t)$ is the mean square relative displacement of all atom pairs initially separated by R after a time interval Δt. Quantitative understanding of shear-induced mixing has been greatly aided by using the mean square relative displacement (MSRD) between pairs of atoms [41,50,46]. This quantity, σ^2, when analyzed by MD simulation of shearing describes the relocation of the atoms during shear-induced mixing and is defined as:

Eq. 2-4 $$\sigma^2(R, t_1, t_2) = \left(\sum_{i=1}^{N} \sum_{j=1}^{z(R,t)} \left[\left(R_{ij}\right)_{t_2} - \left(R_{ij}\right)_{t_1} \right]^2 \right) / 2 \sum_{i=1}^{N} z(R,i)$$

where R_{ij} is the distance between atoms i and j, t_k is a particular instant of time, z(R,i) is the number of such pairs at distance R, and N is the number of atoms in the system. σ^2 describe atoms relocations in terms of relative coordinates of the atoms. This time dependent MSRD enables identification of the atomic mechanisms of mixing.

2.1.3. Superdiffusive nature of shear induced mixing

The dependence of D_{eff} on the pair separation distance R and on time Δt is worth examining. For thermally activated diffusion, e.g. those assisted by vacancies or liquid diffusion, σ^2 is independent of R, and it increases linearly with time as shown in Figure 2.4(a) for liquid Cu. Diffusive mixing, therefore, gives $\sigma^2 \alpha (\Delta t)^1$. However, it was shown for cyclic compressive strains on a model A-B alloy (which closely represent Cu-Ag system) σ^2 increases faster than linearly with time [41] as shown in Figure 2.4(b). This suggests that shear mixing is not a simple diffusive process. The D_{eff} defined in Eq. 2-3 was calculated in MD simulation of cyclic compression of a model 3D crystalline alloy [46] and found to be proportional to R for separation distances $\leq$ L, where L is the size of the computational cell. This interesting behavior can be understood simply on geometric arguments that the probability of a dislocation passing between a pair of atoms is proportional to their separation distance R and this distance increases with time during shear deformation. In the simulations, periodic boundary conditions were used so the dislocations are mostly generated in pairs. Assuming that the separation distance between the pair of generated dislocations is randomly chosen, then the probability that two atoms at a distance R apart will be displaced with respect to one another by the glide of the pair of dislocations is proportional to $R(L-R)/L^2$. This leads to superdiffusive nature of shear

induced mixing dominated by dislocation glide where the probability of a dislocation to pass through a pair of atom is proportional to R and this distance increases with time. The simulation data fitted well to such dependence. This dependence of diffusion coefficient on R during shearing provides us the basis for visualizing self-organization in alloys during SPD. Phase separation by thermal diffusion is independent of R, however, mixing by shearing is proportional to R. Thus, under suitable conditions of shearing and thermal diffusion one can expect the system to be in steady state with a particular length scale. The self-organization behavior will be discussed in more detail in Section 2.2. At this point, this linear dependence of diffusion coefficient on R should be evaluated in a polycrystalline material.

2.1.4. Crossover from superdiffusive to diffusive mixing

To study the dependence of D_{eff} in a polycrystalline material MD simulations were done using $(18.1nm)^3$ nanocrystalline Cu system with an initial grain size of 5 nm. The system is deformed by 12 % uniaxial compression at 100 K. Figure 2.4(b) shows that the D_{eff} is proportional to R at small distances. At larger distances, however, it becomes independent of R as would happen, for example, in thermal diffusion. The distribution of separation distances at a given time was found to be exponential. So, by fitting the data with an exponential relaxation, a crossover length of ≈ 2.37 nm was determined from the decay length. This is about one half the grain size, therefore, for a polycrystalline material of 5 nm grain size it is expected that the superdiffusive mixing behavior will crossover to diffusive mixing at half the grain size. It should be noted that at these small grain sizes the deformation is dominated by grain boundary sliding and grain rotation

[47,48]. At 5 nm grain sizes the dislocation glide contributes only ≈30 % to the total plastic strain, whereas, the contribution increases to ≈90 % at 20 nm grain sizes. Therefore, for larger grain sizes which might be encountered in real experiments, it is expected that dislocation glide will dominate the plastic deformation and the crossover length would be much greater than one-half the grain size.

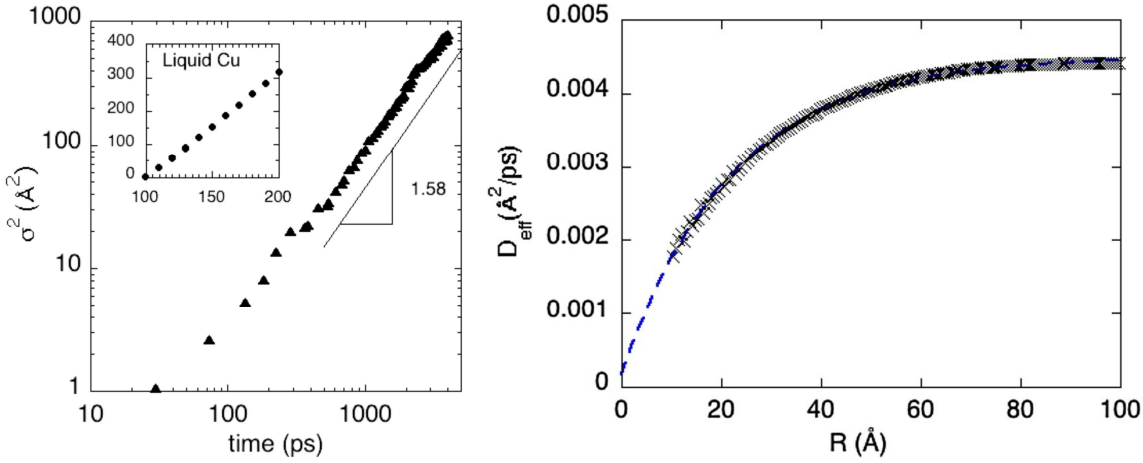

(a) (b)

Figure 2.4. (a) Evolution of the MSRD, σ^2, with time. Notice the power-law regime with an exponent ≈ 1.58. Inset shows the MSRD calculated for liquid Cu at 1600 K, yielding a linear regime, and (b) D_{eff} for the relative displacement of pairs of atoms as a function of the pair separation distance R in nanocrystalline Cu of size $(18.1\ nm)^3$ with an initial grain size of 5 nm (subjected to 12 % compression in MD simulations at a rate of 6×10^8 s^{-1} at 100 K). [46].

2.1.5. Testing superdiffusive mixing in real experiments

It is generally not practical to use the MSRD analysis on the experimental data from plastic deformation of bulk nanocrystalline materials. However, this difficulty can be overcome by using geometric arguments to estimate the mixing rate and the strain to mix for superdiffusive mixing. In a binary A-B system, the rate of mixing is analogous to

the rate of creating new A-B bonds per unit time (or strain) and the strain to mix is the strain required to achieve the maximum possible A-B bonds. In a binary A-B system with B precipitates of initial size $R_{p,i}$, assuming that the dislocations can easily cut through the particles with a probability proportional to their size, the initial rate of mixing is proportional to the rate of creation of the interfacial area at the A-B interface. This rate per unit volume L^3 is equal to the number density of precipitates (n_p) times the probability that a precipitate will be cut by a dislocation ($2R_{p,i}/L$) times the interfacial area created ($g2\pi R_{p,i}b$) times the frequency of dislocation glide (Γ_{sh}) [46]:

Eq. 2-5 $$\frac{d(A/L^3)}{dt} = n_p \frac{2R_{p,i}}{L} g2\pi R_{p,i} b\Gamma_{sh} = \frac{3gV_p}{R_{p,i}}\dot{\varepsilon}$$

where g is a geometrical factor considering that the dislocations cut precipitates at different distances from the center and b is the magnitude of the Burgers vector. The equation is further simplified by taking into account the volume fraction of the precipitates ($V_p = n_p 4\pi R_{p,i}^3/3$) and the relationship between the strain rate and Γ_{sh} ($\dot{\varepsilon} = b\Gamma_{sh}/L$).

If measureable experimentally, the evolution of **Ω** (defined in Eq. 2-1) can track the mixing process. The initial rate of mixing when expressed in terms of **Ω** takes the form:

Eq. 2-6 $$\frac{d\Omega}{dt} = \frac{3g}{4}\frac{V_p}{C_B(1-C_B)}\frac{b}{R_{p,i}}\frac{d\varepsilon}{dt}$$

where C_B is the molar fraction of precipitates. The mixing rate for given initial volume fraction of the precipitates V_p, thus, is proportional to $1/R_{p,i}$. The characteristic plastic

strain required to mix pre-existing precipitates in the absence of thermal diffusion can then be estimated as

Eq. 2-7 $$\Delta\varepsilon_{dis} = \frac{16}{3}\frac{c_B(1-c_B)}{V_p}\frac{R_{p,i}}{b}$$

The key result is that the initial mixing rate scales as $1/R_{p,i}$ and the strain to mix is proportional to $R_{p,i}$. If mixing were to be simply diffusive the strain to mix would scale quadratically with $R_{p,i}$. Further MD simulations were done to test this dependence of the dissolution rate and the strain to mix on the initial precipitate size. Biaxial compression of $A_{75}B_{25}$ alloy (with a positive heat of mixing of ΔH_m = 15.6 kJ/mol) with 1, 10, 30, 50 and 70 initial precipitates was carried out. Figure 2.5 shows the result which clearly indicates that the initial rate of mixing is greater for the smaller precipitates. Also smaller precipitates need less strain to completely mix and the data collapse on one curve when scaled according to Eq. 2-7. 3D MD simulation [25,41, 42,46,49, 50] has shown that shear induced mixing proceeds by dislocation glide across interfaces in systems such as Cu-Ag.

The predictions of Eq. 2-7 had not been tested experimentally at the outset of this research.

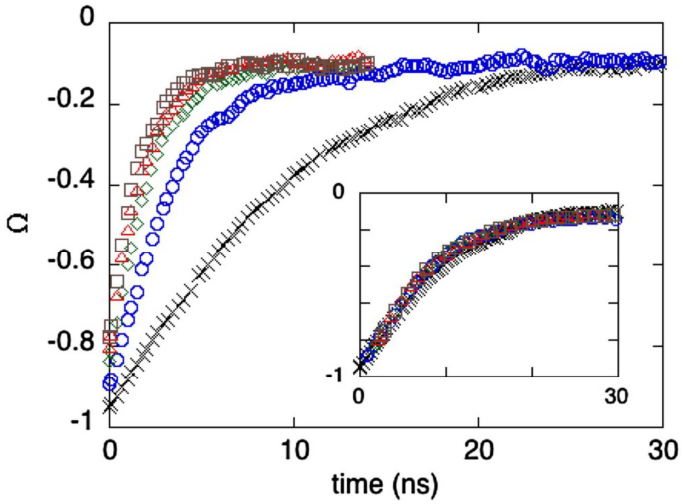

Figure 2.5. Evolution of the mixing parameter Ω during the dissolution of nanoprecipitates forced by biaxial compression of a crystalline $A_{75}B_{25}$ alloy in MD simulations, containing initially 1 (×), 10 (o), 30 (◊), 50 (Δ), and 70 (□) pure *B* precipitates. The inset shows the collapse of data onto one master curve when time is rescaled as $t(R_1/R_n)^{\alpha}$ with α = 1.05, where R_n is the precipitate radius for the initial configuration with *n* precipitates.

2.1.6. Previous experimental studies on quantifying shear induced mixing

A quantitative measurement of strain to mix in an immiscible system was done by Pouryazdan et al. [51]. They used high pressure torsion experiments to study the mixing behavior in $Ag_{60}Cu_{40}$ eutectic alloy. The eutectic alloy was made by repeatedly melting and cooling high purity (99.99 %) pellets of Ag and Cu to homogenize it before casting in water cooled Cu mold. This produced the typical eutectic lamellar structure with an average thickness of Ag and Cu of ≈120 nm and ≈45 nm, respectively. X-ray diffraction (XRD) scans on the samples after deforming for different number of cycles is systematically shown in Figure 2.6(a). The as-cast alloy shows the distinct (111) and (200) peaks for both Ag and Cu. After only 1 cycle of deformation, the Ag(111) peaks

shift towards the right with a small shoulder to the left which is due to the un-mixed Ag. This becomes even less noticeable after 3 cycles ($\gamma \approx 141$) before completely disappearing after 5 ($\gamma \approx 295$) cycles. The peaks have broadened indicating grain size refinement and the intensities from Cu rich phase also disappear. This indicates that a single fcc phase of fully mixed Ag and Cu has formed. The lattice parameter from the main peak is 3.94 Å which matched well with the rapidly quenched $Ag_{60}Cu_{40}$ solid solution [52]. More quantitative analysis was done using differential scanning calorimetry (DSC) studies on the HPT processed samples. The total stored enthalpy plotted against the strain (Figure 2.6(b)) shows saturation after 10 cycles of HPT. The characteristic experimental strain for mixing, γ_e, estimated by the intersection of the linearly extrapolated low and high strain regimes (Figure 2.6(b)) was found to be 350. The formation of a homogenous solid solution was also verified by scanning transmission electron microscope (STEM) images combined with energy dispersive X-ray spectroscopy (EDX) elemental mapping. The lattice parameter calculated from the rings of the fcc solid solution was 3.96 Å which matched well with the XRD result.

This experimental study was done on only one initial length scale. Similar studies on a range of length scale are needed to verify the superdiffusive nature of mixing and how the strain to mix and rate of mixing varies with initial length scale. Moreover, in this study an initial thick sample of 1.0 mm was reduced to 0.1 mm after only one cycle of deformation. A reduction in the sample thickness by a factor of 10 added another uncertainty in comparing it to simulation and model predictions. Also, starting with initial equiaxed microstructures will help to better relate it to the geometrical model presented in the Section 2.1.5.

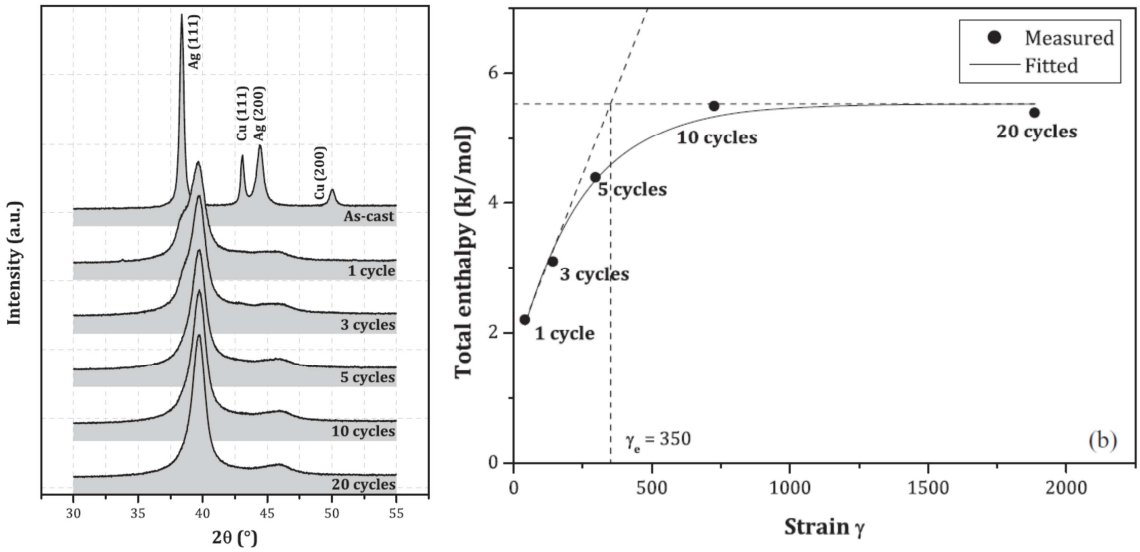

(a) (b)

Figure 2.6. (a) XRD scans of $Ag_{60}Cu_{40}$ eutectic alloy in the as-cast and after different number of HPT cycles, and (b) Total stored enthalpy of the same alloy computed from DSC measurements plotted as a function of strain.

Sun et al. [53] reported a critical strain of 592 to mix millimeter sized Cu and Ag samples corresponding to a composition of $Cu_{59}Ag_{41}$ by atomic percent. The samples were deformed by the constrained configuration of high pressure torsion in which the deformation is possibly localized near the surface. So, the actual strain experienced by the sample near the surface could be multiple times of the reported value of 592. The issue of homogeneity in high pressure torsion processed samples will be discussed in the next chapter on experimental procedures.

2.2. SELF-ORGANIZATION AND ITS STEADY STATE LENGTH SCALES

The superdiffusive nature of the shear induced mixing helps to rationalize the self-organization during sustained shearing at elevated temperatures. We have seen in the MD simulations discussed in the previous section that D_{eff} during shearing is a linear function of pair separation R, whereas, relocations of pair of atoms during thermal diffusion is uncorrelated and, thus, the thermal pair diffusion is independent of R. These two relative diffusion coefficients of two atoms separated by a distance R is schematically illustrated in the Figure 2.7. At small length scales, the thermally activated diffusion dominates and phase separation occurs. At larger length scales shear mixing dominates and the system randomizes. The naive hypothesis is that the steady state length scale (R_{ss}) of the compositional patterning should be approximately determined by the intersection of these two lines [54]. It is assumed that the mixing will be superdiffusive in nature and the deformation is homogeneous. Also shearing and thermal decomposition are assumed to be independent. This hypothesis for the dependence of length scales on temperature or shearing rate has not been adequately studied experimentally and no firm conclusion about these dependencies can be presently drawn. It should be noted that shearing will always produce excess vacancies [55,56] and they will need to be accounted for in any model. The role of shear-induced vacancies will be discussed later. MD simulations have addressed the role of temperature and heat of mixing on the phase separation during high temperature SPD. KMC simulations have addressed factors (e.g. strain rate), which might be more relevant in real experiments to control the length scales

based on Figure 2.7. First couple of examples of self-organization in real experiments will be discussed followed by the simulation results.

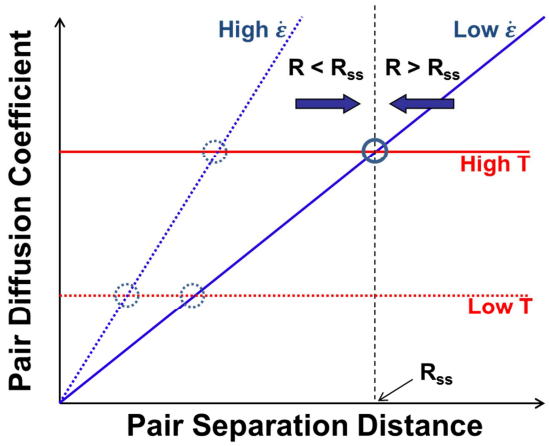

Figure 2.7. Schematic illustration of the proposed patterning length scale model based on the pair diffusion coefficients of shearing and thermal diffusion.

2.2.1. Previous experiments on self-organization

Herr et al. [57] ball milled Ag and Cu and showed that at room temperature a homogenous fcc solid solution is formed and at 423 K a two-phase decomposed microstructure is formed. These two extremes were also predicted in the early KMC simulation model [25] where the competition between the shear induced mixing and thermally induced phase separation were explained in terms of the parameter η. This parameter is the ratio of the frequency of shear induced atomic jumps to the frequency of thermally activated jumps. A large η value results in a homogenous solid solution and a small η results in a phase separated structure. The intermediate values η where the competition between the two frequencies is potentially more interesting in terms of controlling the length scales in the patterning regime were experimentally explored by

BM experiments by Klassen at al. [27]. Ag-Cu system is good for such a study since it achieves a fully mixed and a phase separated state within a narrow range of temperature which is convenient for the high temperature BM experiments. It was shown, by XRD studies, that various steady state microstructures can be stabilized between the homogeneous FCC alloy after milling at temperatures below room temperature and the fully decomposed two-phase mixture after milling at 473 K as shown in the Figure 2.8(a). Up to 423 K the patterns can be fitted assuming the presence of three phases; one homogeneous alloy and the other two phase separated states. The intensity of the homogenous alloy peak decreased with increasing milling temperature. From the integral intensities of the peaks the relative fraction of the alloyed phase was estimated which decreased from 70 % at 316 K to 17 % at 473 K. Differential scanning calorimetry (DSC) measurements showed that the stored enthalpy is released in two stages after milling. The first peak contains the enthalpy related to the chemical decomposition while the second peak is attributed to the grain growth processes. The stored chemical enthalpy decreased with increasing milling temperature as expected. This dependence of stored chemical enthalpy on milling temperature was described by a simple rate equation approach taking into account the independent rate constants for shear induced mixing and thermally induced demixing reactions. The chemical part of the stored enthalpy is plotted in Figure 2.8(b) as a function of milling temperature and the fit is linear within the accuracy of the experimental data. The apparent activation energy, which refers to the chemical decomposition upon milling, was determined from the plot to be 0.114 ± 0.004 eV which is much smaller than for the vacancy migration in either Ag (0.66 eV) or Cu (0.80 eV) [58], and for purely thermal decomposition of $Cu_{50}Ag_{50}$ alloys (≈1 eV) [59,60]. Thus, the

analysis showed that the stored chemical enthalpy during milling has weak temperature dependence. Mixing process is not simply the independent processes of shearing and thermal decomposition by the equilibrium vacancies. Shorter decomposition times during milling indicated that the diffusion is enhanced by milling. This is attributed to the supersaturation of vacancies created by shearing [55,56] and it was concluded that the decomposition reaction by milling has a weak temperature dependence. Due to the use of BM the shearing rate effect could not be investigated.

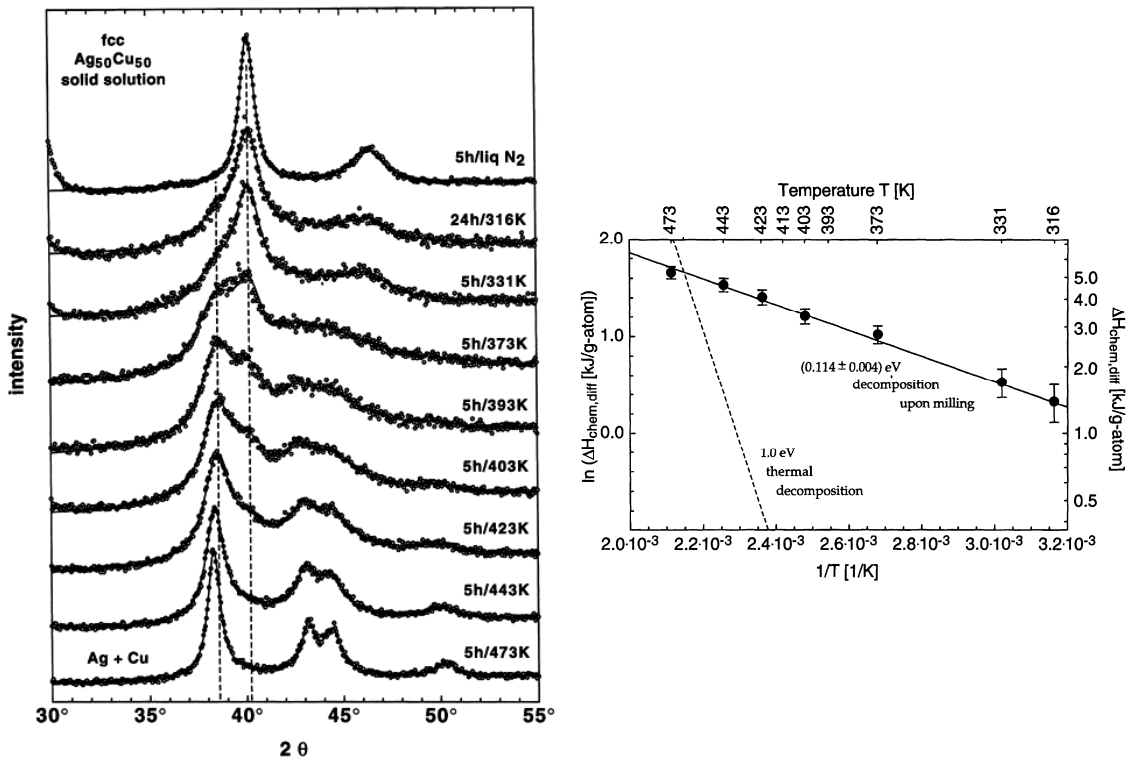

(a) (b)

Figure 2.8. (a) XRD patterns of steady states obtained after milling an $Ag_{50}Cu_{50}$ alloy at different temperatures. The initial powder was prepared by BM the elemental powders at 316 K for 24 hours. (b) Arrhenius plot for the chemical enthalpies stored in $Ag_{50}Cu_{50}$ after milling at different temperatures. The enthalpies have been corrected by subtracting each value of the maximum stored chemical enthalpy measured after cryo-milling, i.e. 5.6 kJ/g-atom. [27].

In another related study, atom probe tomography analysis on ball milled powders of $Cu_{50}Ag_{50}$ showed that the compositional patterns exhibited length scales of ~ 1 nm, 3-5 nm, and 5 – 10 nm at milling temperatures of 393 K, 423 K, and 453 K (Figure 2.9), respectively [70]. This is the first direct experimental verification of the earlier predictions that the length scales should increase as the milling temperature is increased [25]. These length scales when fitted to an Arrhenius plot yielded an apparent activation enthalpy of 0.4 to 0.59 eV, which is between 0.7 eV for vacancy migration enthalpy in Cu and ~0.33 eV for vacancy migration enthalpy in grain boundaries or along dislocations in Ag [70]. However, this calculation is only a rough estimate due to the uncertainty in the measurement of the length scale. Moreover, Cu and Ag phases had enhanced solubilities relative to the equilibrium solubility as opposed to the mutual solubility of the order of 0.1 at. % predicted by the KMC simulation [25]. This large mutual solubility can possibly explain the weak temperature dependence of the stored chemical enthalpy in the previous study [27]. By equating the diffusion coefficient for forced chemical mixing to the thermal one, the authors proposed that the steady state length scale of the compositional patterning R_{ss} should correspond to:

Eq. 2-8 $$R_{ss} \approx \frac{L_g a^2 C_v^{ss} \Gamma_v}{b^2 \Gamma_{sh}}$$

where L_g is the glide length of the dislocations (~grain size in nanocrystalline materials), b is the magnitude of the Burgers vector, a is the vacancy jump distance (for fcc a=b), C_v^{ss} is the vacancy concentration at the steady state, Γ_v is the vacancy jump frequency, and Γ_{sh} is the shear induced atom jump frequency. The two dominant terms contributing to the temperature dependence in Eq. 2-8 are Γ_v and C_v^{ss}. Γ_v follows an Arrhenius type

dependence with an activation enthalpy similar to vacancy migration enthalpy in pure Cu and pure Ag (bulk, grain boundary, or pipe diffusion depending on the controlling migration path). The C_v^{ss} can be estimated from a rate equation model [27,61,62]:

Eq. 2-9 $$\frac{dC_v}{dt} = X\left(1 - \frac{C_v}{C_{sat}}\right)\Gamma_{sh} - Y(C_v - C_v^{th})\Gamma_v$$

The production of excess vacancies by non-conservative motion of dislocations is accounted in the first term on the right hand side. This concentration saturates when $C_v = C_{sat} \approx 10^{-3} - 10^{-2}$ at. % (the maximum vacancy concentration a solid may support) [70]. The elimination of vacancies at sinks is accounted in the second term where C_v^{th} is the equilibrium vacancy concentration. The details of the microstructure such as grain size and dislocation density is accounted in the terms X and Y and, thus, display a weak temperature dependence. However, in this study this temperature dependence is ignored because in the temperature range of interest the microstructural changes are expected to be small. Two limiting cases were discussed; (1) At low temperature and high strain rates, Γ_v/Γ_{sh} becomes infinitely small and $C_v^{ss} \approx C_{sat}$. Therefore, vacancy concentration becomes independent of temperature and the patterning length scale would be dominated by the Arrhenius behavior of Γ_v. (2) At high temperature and low stain rates, $C_v^{ss} << C_{sat}$, and the product $C_v^{ss}\Gamma_v$ becomes independent of temperature and linearly proportional to Γ_{sh}. In this regime, thus, the patterning length scale should be independent of milling temperature and shearing rate. The results in this study hint that the systems are in low temperature regime where $C_v^{ss} \approx C_{sat}$. However, more work is required over a broader range of temperatures and, more importantly, over a range of shearing rates (varying the forcing frequency) to come to any firm conclusion.

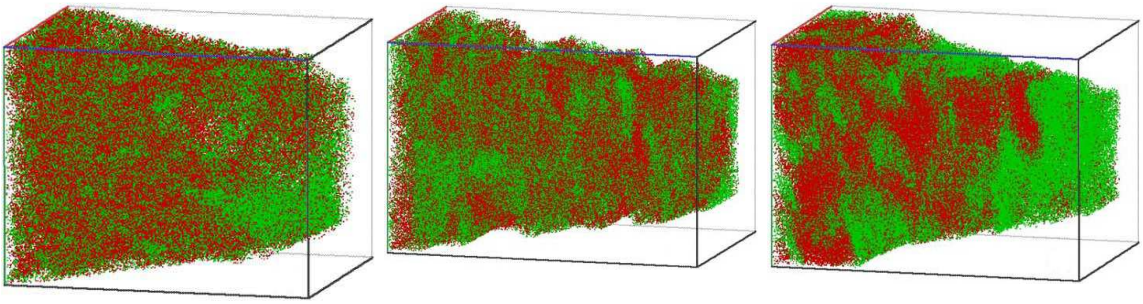

(a) **(b)** **(c)**

Figure 2.9. 3D APT reconstruction map for $Cu_{50}Ag_{50}$ ball milled at (a) 393 K, (b) 423 K, and 453 K. Vertical length of the box is 20 nm for all figures. Only Cu and Ag atoms are shown in red and green, respectively [70].

2.2.2. Length scales predicted by KMC simulation

The predictions of the patterning length scale in the simple model presented in Figure 2.7 were also tested by the KMC simulation [54]. The simulations also looked into the morphologies and solubilities of two-phase alloy as a function of the strain rate. At low temperatures and high strain rate the system tends to homogenize, whereas, at high temperatures and low strain rates the solubilities approach their equilibrium values. In the intermediate regimes, it is not well known what governs the solubilities. The BM experiments by Klassen et al. [27] did show that solubilities vary with milling temperature at an unknown, but fixed, shearing rate. Rigid lattice KMC simulations of a crystal under shear in presence of thermal diffusion is performed similar to [27]. The thermal pair diffusion from the KMC simulations is simply computed as:

Eq. 2-10 $$D^{p}_{therm} = 2F_{vac}\frac{a_o^2}{d^3}$$

where F_{vac} is the number of vacancy jumps per unit time, d^3 is the number of atoms in the computational cell, and a_o is the nearest neighbor distance. The pair diffusion coefficient due to shear is computed as:

Eq. 2-11 $$D^{p}_{shear}(R) = a_o^2 F_{shear} d^{-1} \left(\frac{R}{a_o}\right)$$

where F_{shear} is the frequency at which dislocations are inserted in the simulation cell and d is the number of atomic planes. The factor (R/a_o) accounts for the number of atomic planes having a constant probability of a dislocation passing between the pair separated by distance R.

The selection of the dislocation glide plane is random which is a good approximation for a coherent system where dislocations can glide across interfaces with little hindrance. The shear induced pair diffusion coefficient was equated with the thermally activated pair diffusion coefficient to yield the steady state length scale, R_{ss}, as:

Eq. 2-12 $$R_{ss} = \frac{a_o}{d^2} \frac{F_{vac}}{F_{shear}}$$

A Fourier transform based analysis, where the microstructural length scales were estimated from the first moment of the structure factor, showed good agreement with the Eq. 2-12 as shown in the Figure 2.10(a) for varying temperatures, alloy concentrations, and cell sizes. The dashed line represents Eq. 2-12. Linearity of all the curves is maintained over 3 – 4 orders of magnitude of strain rate and is close to the model prediction. For a 15 % alloy the length scale at 600 K is ~3 times more than that at 400 K which is due to a lower effective thermal diffusion coefficient at 400 K. Also it is shown that for 50 % alloy the size of the simulation cell doesn't affect the length scale at a

particular temperature and shearing rate, thus, the finite size of simulation cell doesn't result in inaccuracies. Moreover, the length scales increased with increasing solute concentration. The inset in Figure 2.10(b) shows that the vacancy jump rate increases with the shearing rate due to the faster hopping of vacancies since shearing doesn't produce vacancies in this KMC simulation. At high shearing rates the vacancy jump frequency becomes independent of the shear rate. Figure 2.10(a) which plots length scales versus F_{vac}/F_{shear} takes into account this effect by directly counting the vacancy jumps. The dependence of solubility on strain rate (Figure 2.10(b)) showed three regions; at very low strain rates the samples approached thermodynamic equilibrium solubility, at intermediate strain rates the solubility scaled as (strain rate)$^{1/3}$, and at high strain rates the samples become nearly solid solution. This shows that the solubility can be completely tuned between the equilibrium solubility and the fully mixed solid solution by changing the shearing rate.

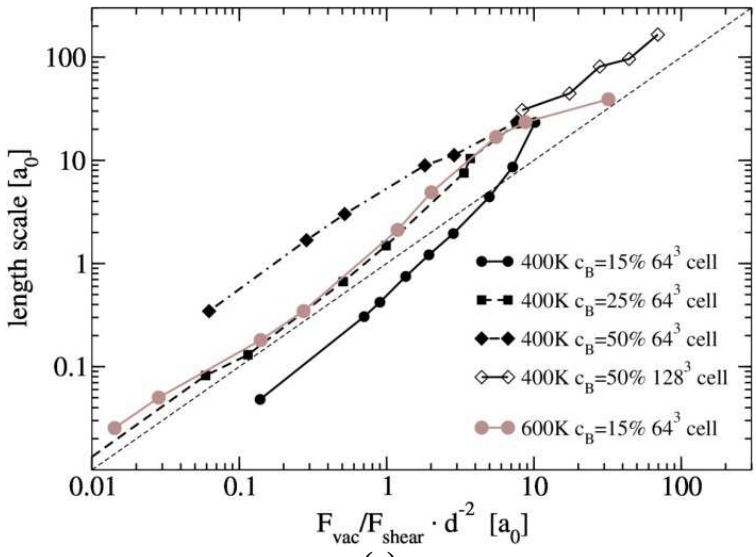

(a)

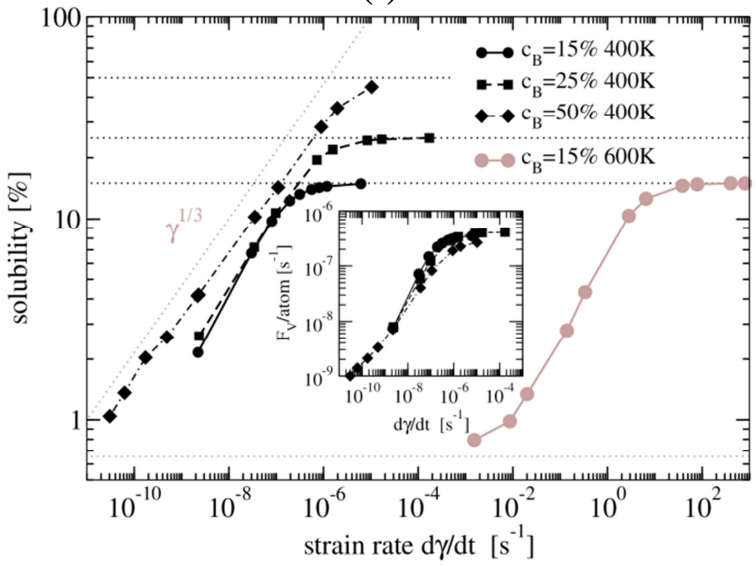

(b)

Figure 2.10. (a) Length scale at steady state versus predicted length scale $F_{vac}/F_{shear)}*d^{-2}$, and (b) Dependence of solubility of B atoms on strain rate. Inset shows vacancy jump rate as a function of stain rate [54].

In understanding the dynamic competition between shearing induced mixing and thermally induced decomposition in experiments, it is important to study the effect of shearing on thermal diffusion coefficient via shear-induced vacancies as well as the faster hopping of vacancies. Both of these effects will alter the ratio F_{vac}/F_{shear} and will make

direct comparison with experiments much more challenging. In the KMC model above it is shown in the inset in Figure 2.10(b) that F_{vac} increases with F_{shear} at 400 K which is due to the faster hopping of vacancies since shearing doesn't produce vacancies in this model. At higher shearing rates F_{vac} becomes constant. This behavior is attributed to trapping of vacancies at some lattice sites. At low shearing rates the vacancies remain trapped until shearing changes their local environment enough to force them to free them. It was found in these simulations, for example, at 400 K that jump frequencies of vacancies surrounded by only one kind of atom is ~120 times slower than at sharp (111) interfaces. At higher shearing rates the local environment is changing rapidly compared to fastest vacancy jump frequency, thus, it becomes nearly independent. In real experiments, it's very difficult to decouple the effect of faster hopping of vacancies and shear-induced excess vacancies. Shear induced vacancies during high temperature deformation, however, have been modeled [55,56] and the results will be presented in the next section and discussed in terms of how length scales in real experiments could differ from those predicted in Figure 2.7. This KMC simulation also investigated if the increased solubilities during shearing is due to the Gibbs-Thomson effect as suggested previously [63]. It was shown that the enhancement of solubility by shearing at 600 K was well above the theoretical solubility by Gibbs-Thomson equation. Moreover, the solubility decreased after shearing stopped. It was concluded, therefore, that the solubility is dominated by the kinetic processes (shearing) rather than the thermodynamic effects (Gibbs-Thomson).

2.2.3. Role of shear induced vacancies

The presence of excess vacancies stimulates diffusion and precipitation processes. Thus, shear-induced excess vacancies during high temperature deformation will also affect how the system chooses a particular length scale as discussed in the previous section. The production and annihilation of vacancies by plastic deformation at elevated temperature has been treated by a phenomenological model [55].

At elevated temperatures the nonconservative motion of the thermal jogs in addition to the conventional jogs contribute to the generation of excess vacancies. The production rate of the excess vacancies, Ψ, can be expressed as:

Eq. 2-13 $$\Psi = \chi \frac{\sigma \Omega_o}{Q_f} \dot{\varepsilon} + \zeta \frac{c_j \Omega_o}{4b^3} \dot{\varepsilon}$$

which is proportional to the strain rate. The constant χ in the first term on right hand side is ~0.1 [64,65], σ is the stress, Ω_o is the atomic volume, Q_f is the vacancy formation energy, ζ takes into account the neutralization effect of vacancy emitting and vacancy absorbing jogs [66], c_j is the concentration of thermal jogs, and b is the magnitude of the Burgers vector.

The annihilation of vacancies at sinks (grain boundaries, dislocations etc) is diffusion controlled. It depends on the vacancy super-saturations C_{ex}, the sink density and the vacancy diffusivity D_v, and the annihilation rate can be expressed as:

Eq. 2-14 $$\Lambda = \frac{D_v \rho}{\kappa^2} C_{ex} + \frac{D_v}{L^2} C_{ex}$$

where ρ is the dislocation density, L is the grain size, κ describes the distribution of dislocations (κ=1 for homogeneous distribution and =10 for a cell-like substructure). The net rate of production of shear induced excess vacancies is $\frac{dC_{ex}}{dt} = \Psi - \Lambda$. Thus,

Eq. 2-15 $$\frac{dC_{ex}}{dt} = \chi \frac{\sigma \Omega_o}{Q_f} \dot{\varepsilon} + \zeta \frac{c_j \Omega_o}{4b^3} \dot{\varepsilon} - \frac{D_v \rho}{\kappa^2} C_{ex} + \frac{D_v}{L^2} C_{ex}$$

At a given temperature and strain rate the excess vacancy concentration tends to a steady state value which depends on the stress, concentration of thermal jogs, dislocation density, grain size, vacancy formation energy and vacancy diffusivity. At constant strain rate the steady state excess vacancy concentration was estimated to be

Eq. 2-16 $$C_{ss} = \left(\frac{\chi \sigma}{Q_f} + \frac{\zeta c_j}{4b^3}\right)\left(\frac{\rho_{ss}}{\kappa^2} + \frac{1}{L^2}\right)^{-1} \frac{\Omega_o}{D_V} \dot{\varepsilon}$$

where ρ_{ss} is the steady state dislocation density.

For further details of the model the reader is referred to Ref. [55]. As an example, Figure 2.11 shows the dependence of the steady state excess vacancy concentration with temperature and strain rate for ferrite and austenite. The excess concentration decreases with temperature but can be significantly greater than the thermal equilibrium one for appropriate strain rates. For example, at strain rates > 10 s^{-1}, the austenite shows several orders of magnitude higher vacancy concentration. The effect is larger in austenite because of its close packed structure which slows down diffusivity and vacancy annihilation. In ferrite, on the other hand, similar vacancy concentrations are attained at roughly 300 K lower temperatures.

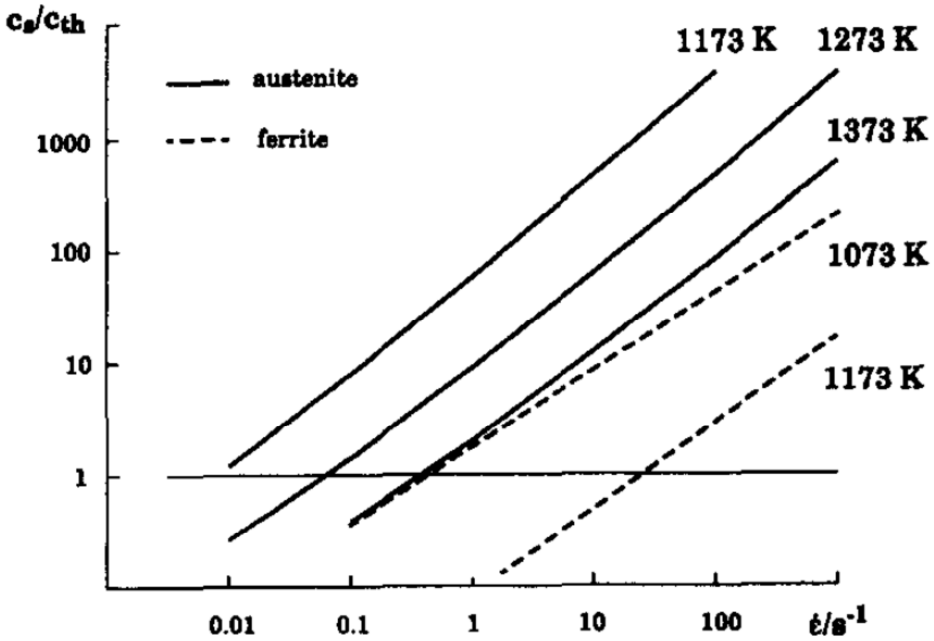

Figure 2.11. Dependence of the steady state excess vacancy concentration on temperature and strain rate for austenite (solid lines) and ferrite (dashed lines) [55].

Based on this model, the dashed lines in the Figure 2.12(a) shows the total vacancy concentration (thermal + shear-induced) with increasing strain rate and temperatures for Cu using the parameters and constants given in the Table 2.1. The thermal concentration of vacancies is shown by the solid lines for comparison. Above a certain strain rate, which depends on the temperature, the shear induced vacancies starts to dominate. Higher strain rate is needed for shear induced vacancies to dominate at higher temperatures because of the higher annihilation rate. Thus, it can be seen that depending on the temperature and strain rate, the shear induced vacancies will directly affect the F_{vac}/F_{shear} ratio during actual experiments. The change of these ratios with strain rate and temperature will be discussed next in view of their influence on the predicted length scales Figure 2.7.

n	4.5
Qdef	2.04 eV
k	8.62E-05 eV/K
A	38.8 MPa
ζ	0.499788594
ζ_o	10
χ	0.1
κ	10
Q_f	1.05 eV
Q_m	0.74 eV
D_{vo}	2.50E-05 m^2/s
Q	2.51 eV
L	1.50E-08 m
β_o	700 MPa
μ	4.52E+10 J/m^3
ν	0.3
Ω_o	1.18E-29 m^3
b	2.55E-10 m
Ej	8.51751E-20 eV
a	2.56E-10 m

Table 2.1. Parameters and constants used in the excess vacancy concentration calculations for pure Cu.

The vacancy jump frequency was used to calculate the total number of jumps per second at a particular temperature and strain rate. This quantity is related to F_{vac}. From the density of dislocations, the mean dislocation spacing and velocity was estimated for each temperature and strain rate. This gives the frequency of shearing which is directly related to the imposed strain rate. The ratio, F_{vac}/F_{shear}, is plotted in Figure 2.12 (b) for Cu. It is interesting to note that in the regime where shear induced vacancies become dominant the ratio F_{vac}/F_{shear} doesn't increase significantly by increasing the imposed strain rate. That means in this regime the length scales cannot be controlled by changing the strain rate which is analogous to the sink elimination regime for alloys under irradiation. For example, in Cu at a temperature of 300 °C and at strain rates above 0.1 s^{-1}

the ratio F_{vac}/F_{shear} doesn't change and so the length scales are expected to be independent of the shearing rate. However, at strain rates less than 0.1 s^{-1}, the length scales would increase with decreasing strain rate as predicted by Figure 2.7. We can thus see that there are two regimes; at higher temperatures and low strain rates the length scales would be strongly dependent on the strain rate, and at lower temperatures and high strain rates the length scales would be weakly dependent on the strain rates. Length scales are expected to be more controllable at higher temperatures because of the less influence of the shear induced vacancies. It should be noted that these calculations are just approximate and show the general trend. In real systems, there will be a break down in assumptions of constant sink density, strain accommodation by a single strain rate independent process, the lack of considerations of defect solute interactions, and the large uncertainty associated with the values of the physical parameters utilized in the model. Also, the total number of vacancies produced at equivalent strain under different strain rates is unlikely to be equivalent. Shearing will generate vacancies in events such as dislocations cutting one another. Competing deformation process such as grain boundary sliding and twinning may be strain rate dependent and the total defect production may vary slightly.

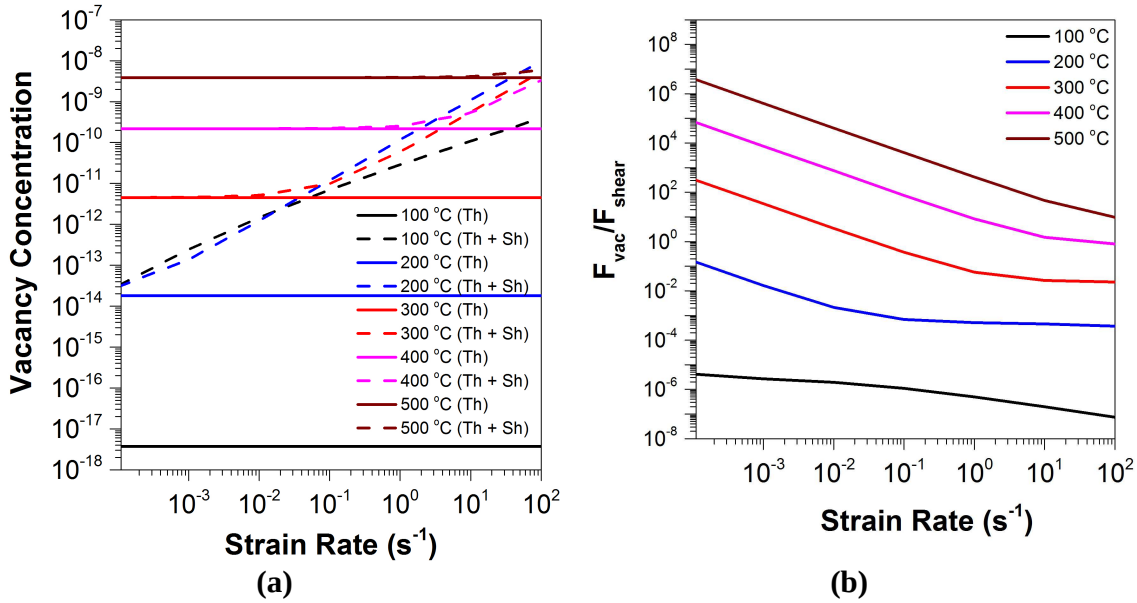

Figure 2.12. (a) Total vacancy concentration (Th + Sh) compared to the thermal only (Th) for increasing temperatures and strain rates in Cu, and (b) The estimated ratio of F_{vac}/F_{shear} with increasing strain rates and temperatures in Cu.

Experimental evidence of self-organization during high energy BM at elevated temperatures exists in studies by X-ray diffraction and differential scanning calorimetry [67], transmission electron microscopy [68], atom probe field ion microscopy [69], and atom probe tomography [70,71]. However, there is little direct experimental verification of the intuitive models and simulation results [54,70] for the length scales with varying strain rates and temperatures. The naive model in Figure 2.7 and KMC simulation results in Figure 2.10 should be carefully compared to real experiments based on the estimated effect of the faster hopping of vacancies and the shear-induced vacancies on the predicted length scales as shown in Figure 2.12. The use of ball milling presents a major challenge in that the strain rate and total strain are not well defined. This limits our ability to quantitatively interpret the results in the context of known materials properties such as

vacancy diffusivity and shear-induced mixing rate, and hinders the validation of an appropriate model.

2.3. SEVERE PLASTIC DEFORMATION BY HIGH PRESSURE TORSION

There are a number of well-known SPD techniques that can be employed in this thesis research. In accumulative roll bonding (ARB) the material to be processed is rolled into ≈50 % thick sheet, cut into two pieces, stacked together, and then rolled again [72]. This procedure is repeated multiple times until desired microstructure is achieved. In equal channel angular pressing (ECAP), a billet is pressed multiple times through a die which has two channels typically at 90° [17]. This procedure is also repeated multiple times and during each cycle the cross-section dimensions are preserved. In both ARB and ECAP the total amount of strain in each cycle is roughly on the order of 1. According to the Eq. 2-7, which was derived on geometrical arguments for the total strain to mix spherical precipitates of initial radius $R_{p,i}$, the strain to mix a $Cu_{90}Ag_{10}$ alloy with $R_{p,i}$ of 100 nm is ≈ 1200. A recent study on $Ag_{60}Cu_{40}$ eutectic alloy reported a strain of ≈350 to fully mix the lamellar structure of wavelength ≈165 nm [51]. The use of ARB or ECAP would require hundreds of cycles to achieve such a high level of strain and, therefore, are not practical to use.

High pressure torsion (HPT) [73,74,75] as a SPD technique has received considerable interest recently because the combination of high compressive stress and

torsional straining results in large plastic strains without fracture. The strain at any point is

Eq. 2-17 $\varepsilon = 2\pi rn/t$

where r is the radial position, n is the number of full rotations, and t is the actual thickness of the sample at that position. The strain varies from zero in the center to the maximum value at the edge which is advantageous in my research for studying the microstructural changes with strain, strain rate, and temperature. For example, the total strain at r = 4mm for a sample deformed by 10 cycles in HPT is ≈1000 assuming the thickness is 250 μm.

In HPT, the sample can be processed in either unconstrained configuration, between flat anvils, or quasi-constrained configurations, between anvils having cavities [76] as shown in Figure 2.13. Most of the recent research on HPT processing has been focused on quasi-constrained configurations where plastic deformation does not propagate homogeneously through the sample thickness [73,77]. In fact, in these cases, plastic deformation is localized near the surface and the actual strain experienced by this surface layer could be 1 – 2 orders of magnitude larger than that estimated from Eq. 2-17. Therefore, achieving homogeneous deformation through thickness is critical to precisely relate any microstructural changes with the processing variables. HPT can be performed in a continuous cycle where the anvil rotates in one direction only. One continuous cycle is full 360° rotation of the anvil. Alternatively, it can be performed in a back and forth cycle where one of the anvils is rotated by +90° and -90°. Thus, the strain in one continuous cycle is twice that in one back and forth cycle.

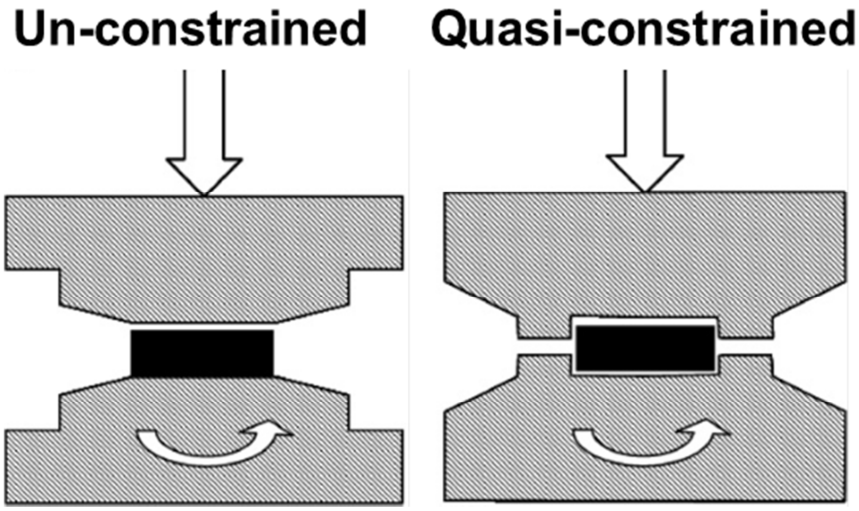

Figure 2.13. Schematic of un-constrained and quasi-constrained configuration in high pressure torsion [76].

2.4. MECHANICAL PROPERTIES

The grain size has a significant effect on the mechanical properties of metals and alloys. The relationship between grain size (L) and yield strength (σ_y) is given by the well-known Hall-Petch relation according to which the yield strength increases as the inverse square root of the grain size (diameter).

Eq. 2-18 $$\sigma_y = \sigma_o + kL^{-1/2}$$

where σ_o is intrinsic yield stress (a material constant) and k is the strengthening coefficient. Coarse grained materials (grain sizes above 1 μm) obey this relationship very well. In general, ultra-fine grained materials (grain sizes in 100 nm - 1 μm range) still obey this relation [78].

Nanostructuring is particularly attractive for developing new high-strength alloys with superior strength/weight ratio which are inherently strong due to the high density of grain boundaries and interfaces [79,80,81,82,83]. However, in nanostructured metals and alloys with grain sizes < 100 nm deviation from this Hall-Petch relationship has been reported [84,85]. This deviation can be of varying nature. For example, in materials with 20-100 nm grain size, the strength still continues to increase but with a reduced Hall-petch coefficient. In other materials, the strength might saturate below a critical grain size (typically on the order of 10nm). Yet, some materials show a decreased strength below this critical grain size. This change in strength is usually attributed to the change in the dominant deformation mechanism. The strength comes from the dislocation pile ups near the grain boundaries [86,87]. With decreasing grain size, the number of dislocations that can pile up decreases because of limited space in grain interiors for dislocation glide [88]. Below a critical grain size, the deformation is dominated by the grain boundary based mechanisms and dislocation based mechanisms become less dominant. Further reduction in the grain size may result in the softening which is known as the inverse Hall-petch relation [89,90,91]. This sets the limit on how strong the nanostructured material can be and poses an interesting scientific challenge to overcome this barrier. Producing such fine grain sizes of 10nm or less is extremely difficult and at these scales the material is near its amorphous state. Solid solution hardening, second-phase particle hardening and grain boundary hardening can collectively contribute to the strength. Schuh et al. [92] studied the effect of solid solution strengthening in Ni and Ni-W alloys with grain sizes less than 10 nm. Ni-W showed finer grain sizes and slightly higher hardness than pure Ni. A standard model for substitutional solid solution strengthening which is based on the

elastic dislocation-solute interactions [93] was used and showed a negligible increase in the hardness by solid solution strengthening. It was concluded that the solid solution strengthening from W is roughly one order of magnitude less than the intrinsic hardness of Ni and significantly smaller than grain boundary strengthening. Thus, the hardening in pure Ni and in Ni-W alloys can be explained by grain boundary hardening only. The breakdown in Hall-petch occurred at a grain size of ≈8 nm which is less than the previously reported value of ≈14 nm for pure Ni suggesting that alloying had delayed the Hall-petch breakdown.

In this thesis research, it is expected that by using the principles of forced chemical mixing and self-organization at nanometer length scales, a variety of microstructures can be obtained. For example, a complete solid solution, a completely phase-separated or an intermediate state (where fine second phase particles are present in addition to some solid solubility) can potentially be fabricated by controlling the SPD conditions. The strength of these materials will be explored to further investigate the dependence of their mechanical properties on their microstructural features and length scales.

2.5. REFERENCES

[1] Raabe D et al. MRS Bull 2010;35:982.
[2] Valiev RZ, Islamgaliev RK, Alexandrov IV. Prog Mater Sci 2000;45:103.

[3] Martin, Georges and Bellon, Pascal. “Driven Alloys.” *Solid State Physics* 50 (1997): 189–331.

[4] Gilman PS, Benjamin JS. Annu Rev Mater Sci 1983;13:279.

[5] Ma E, Atzmon M. Mater Chem Phys 1995;39:249.

[6] C. Suryanarayana, Progress in Materials Science 46, 1-184 (2001).

[7] D.B. Witkin and E J. Lavemia, Prog. Mater. Sci. 5 1 ,1 (2006)

[8] E. Ma, Prog. Mater. Sci. 50, 413 (2005)

[9] E. Hellstem, H J. Fecht, C. Garland and W.L. Johnson. In: L.E. McCandlish, D.E. Polk, R.W. Siegel and B.H. Kear, Editors, Multicomponent ultrafine microstructures 132, Mater. Res. Soc, Pittsburgh, PA,137-142 (1989)

[10] J.J. deBarbadillo, F.H. Froes and R. Schwarz, Editors, Mechanical alloying for structural applications, ASM International, Materials Park, OH (1993).

[11] G.B. Schaffer and P.G. McCormick,. Appl. Phys. Lett 55, 45 (1989)

[12] C. Suryanarayana and H. Jones, Internal J. Rapid Solidification 3,253 (1988)

[13] C.C. Koch, O.B. Cavin, C.G. McKamey and J.O. Scarbrough, Appl. Phys. Lett 43, 1017(1983)

[14] C. Gente, M. Oehring and R. Bormann, Phys. Rev B 48, 13244 (1993)

[15] R. Z. Valiev, N. A. Krasiinikov and N. K. Tsenev, Materials Science and Engineering A137 (1991) 35-40.

[16] R.Z.Valiev ,T.G.Langdon,Prog.Mater. Sci. 51 (2006) 881.

[17] R.Z.Valiev, R.K.Islamgaliev and I.V.Alexandrov, Prog Mater Sci 45 (2000) 103

[18] Martin G, *Phys Rev B* 30, 1424 (1984)

[19] Martin, G. and P. Bellon, Driven alloys, in Solid State Physics - Advances in Research and Applications, Vol 50. 1997, Academic Press Inc: San Diego. p. 189-331.

[20] J. Ye, J.-wen Liu, R. a. Enrique, P. Bellon, Scripta Materialia 49 (2003) 969-975.

[21] P. Bellon and R. Averback, Scripta Materialia 49, 921-925 (2003).

[22] C.C. Koch and J.D. Whittenberge, Intermetallics 4, 339-355 (1996).

[23] C. Suryanarayana, Progress in Materials Science 46, 1-184 (2001).

[24] F. Delogu, M. Pintore, S. Enzo, F. Cardellini, V. Contini, A. Montone, V. Rosato, Philosophical Magazine 76 (1997) 651-662.

[25] P. Bellon, R. Averback, Physical Review Letters 74 (1995) 1819-1822.

[26] C. P. Flynn, Point Defects and Diffusion (Clarendon Press, Oxford, 1972), p. 310.

[27] T. Klassen, U. Herr, and R. S. Averback, Acta Mater. 45, 2921 (1997).

[28] F. Delogu et al., Philos. Mag. B 76, 651 (1997).

[29] C. Gente, M. Oehring, and R. Bormann, Phys. Rev. B 48, 13244 (1993).

[30] Ma E, Atzmon M. Mater Chem Phys 1995;39:249.

[31] Quelennec X, Menand A, Le Breton JM, Pippan R, Sauvage X. Philos Mag 2010;90:1179.

[32] Xu J, Herr U, Klassen T, Averback RS. J Appl Phys 1996;79:3935.

[33] Xu J, He JH, Ma E. Metall Maters Trans A 1997;28A:1569.

[34] Botcharova E, Freudenberger J, Schultz L. JMater Sci 2004;39:5287.

[35] Wang M., Averback R., Bellon P., Dillon S., Acta Mater 2014;62;276.

[36] E. Ma, J.-H. He, and P. J. Schilling, Phys. Rev. B 55, 5542 (1997)

[37] A. Da Pozzo, S. Palmas, A. Vacca, F. Delogu, Scripta Mater, 67 (2012), p. 104

[38] A. R.Yavari, P. J. Desre, and T. Benameur, Phys. Rev. Lett. 68, 2235 (1992)

[39] E. Ma, J.H. He, P.J. Schilling, Phys Rev B, 55 (1997), p. 5542

[40] M. Wang et al., Acta Materialia 66, 1-11 (2014)

[41] S. Odunuga, Y. Li, P. Krasnochtchekov, P. Bellon, and R. Averback, Physical Review Letters 95, 93-96 (2005).

[42] Y. Ashkenazy, N.Q. Vo, D. Schwen, R.S. Averback, and P. Bellon, Acta Materialia 60, 984–993 (2012).

[43] A. Lund and C. Schuh, Physical Review Letters 91, 1-4 (2003).

[44] Delogu F. J Appl Phys 2008;104:073533.

[45] Odunuga, S, PhD Thesis, 2007

[46] P. Bellon, R. Averback, S. Odunuga, Y. Li, P. Krasnochtchekov, and A. Caro, Physical Review Letters 99, 1-4 (2007).

[47] J. Schiotz, F. D. Di Tolla, and K.W. Jacobsen, Nature 391, 561 (1998).

[48] N. Vo, R. Averback, P. Bellon, S. Odunuga, a. Caro, Phys. Rev. B 77 (2008) 1–9.

[49] D. Raabe, S. Ohsaki, and K. Hono, Acta Materialia 57, 5254–5263 (2009).

[50] Vo NQ, Odunuga S, Bellon P, Averback RS. Acta Mater 2009;57:3012.

[51] M. Pouryazdan, D. Schwen, D. Wang, T. Scherer, H. Hahn, R.S. Averback, P. Bellon, Phys. Rev. B 86 (2012) 144302.

[52] R. K. Linde, J. Appl. Phys. 37, 934 (1966)

[53] Y.F. Sun, H. Fujii, T. Nakamura, N. Tsuji, D. Todaka, M. Umemoto, Scr. Mater. 65 (2011) 489–492.

[54] D. Schwen, M. Wang, R.S. Averback, and P. Bellon, In preparation.

[55] M. Militzer, W.P. Sun, and J.J. Jonas, Acta Metallurgica Et Materialia 42, 133–141 (1994).

[56] S.-H. Song, X.-M. Chen, and L.-Q. Weng, Materials Science and Engineering: A 528, 7196–7199 (2011).

[57] Herr, U. and Samwer, K., in *Solid-State Transformations*, ed. W.C. Johnson, J.W. Howe, D.E. Laughlin and W.A. Soffa. TMS, Warrendale, 1994, p. 1039.

[58] Ehrhart, P., in *Atomic Defects in Metals*, Landolt-Boernstein, New Series III, Vol. 25, ed. H. Ullmaier. Springer, Berlin, 1991

[59] R.K. Linde, Trans. Met. Soc. AIME, 236 (1966), p. 58

[60] S. Mader, A.S. Nowick, Acta metall., 15 (1967), p. 215

[61] Pochet P, Tominez E, Chaffron L, Martin G. Phys Rev B 1995;52:4006.

[62] Meckin H, Estrin Y. Scripta Metall 1980;14:815.

[63] A. R. Yavari, Mater Sci Eng A 179/180 (1994) 20.

[64] H. Mecking and Y. Estrin, *Scripta metall.* 14, 815 (1980).

[65] G. Saada, *Acta metall.* 9, 166 (1961).

[66] C. R. Barrett and W. D. Nix, *Acta metall.* 13, 1247 (1965).

[67] T. Klassen, U. Herr, and R.S. Averback, Acta Materialia 45, 2921-2930 (1997).

[68] S. Zghal, R. Twesten, F. Wu, P. Bellon, Acta Materialia 50 (2002) 4711-4726.

[69] F. Wu, P. Bellon, A. Melmed, and T. Lusby, Acta Materialia 49, 453-461 (2001).

[70] F. Wu, D. Isheim, P. Bellon, and D. Seidman, Acta Materialia 54, 2605-2613 (2006).

[71] M. Brocq, B. Radiguet, J.-M. Le Breton, F. Cuvilly, P. Pareige, and F. Legendre, Acta Materialia 58, 1806–1814 (2010).

[72] N. Tsuji, Y. Saito, S.-H. Lee, Y. Minamino, Adv. Eng. Mater. 5 (2003) 338–344.

[73] A. Zhilyaev, T. Langdon, Progress in Materials Science 53 (2008) 893-979.

[74] R. Pippan, S. Scheriau, A. Hohenwarter, M. Hafok, Materials Science Forum 584-586 (2008) 16-21.

[75] R. Valiev, Nature Materials 3 (2004) 511-6.

[76] A.P. Zhilyaev, T.R. McNelley, T.G. Langdon, Journal of Materials Science 42 (2006) 1517-1528.

[77] A. Révész, S. Hóbor, J.L. Lábár, A.P. Zhilyaev, Z. Kovács, Journal of Applied Physics 100 (2006) 103522.

[78] M.A. Meyers, A. Mishra, D.J. Benson, Progress in Materials Science 51 (2006) 427-556.

[79] Chokshi, A.H., A. Rosen, J. Karch, and H. Gleiter, Scripta Metallurgica, 1989. 23(10): p. 1679-1683.

[80] Schuh, C.A., T.G. Nieh, and H. Iwasaki, Acta Materialia, 2003. 51(2): p. 431-443.

[81] Nieman, G.W., J.R. Weertman, and R.W. Siegel, Scripta Metallurgica, 1989. 23(12): p. 2013-2018

[82] Dao, M., L. Lu, R.J. Asaro, J.T.M. De Hosson, and E. Ma, Acta Materialia, 2007. 55(12): p. 4041-4065.

[83] Suryanarayana, C., Advanced Engineering Materials, 2005. 7(11): p. 983-992.

[84] T.J. Rupert, D.S. Gianola, Y. Gan, K.J. Hemker, Science 326 (2009) 1686-1690.

[85] C.E. Carlton, P.J. Ferreira, Acta Materialia 55 (2007) 3749 – 3756.

[86] E.O. Hall, Proceedings of the Physical Society of London Section B 64 (1951) 747-753.

[87] N.J. Petch, Journal of the Iron and Steel Institute 174 (1953) 25-28.

[88] V. Yamakov, D. Wolf, M. Salazar, S.R. Phillpot, H. Gleiter, Acta Materialia 49 (2001) 2713-2722.

[89] T.G. Nieh, J. Wadsworth, Scripta Metall. Mater, 25 (1991), p. 955

[90] V. Yamakov, D. Wolf, S.R. Phillpot, A.K. Mukherjee, H. Gleiter, Philosophical Magazine Letters 83 (2003) 385-393.

[91] G. Palumbo, S.J. Thorpe, K.T. Aust, Scripta Metall. Mater, 24 (1990), p. 1347

[92] C.A. Schuh, T.G. Nieh, T. Yamasaki, Scripta Materialia 46 (2002) 735-740.

[93] R.L. Fleischer, Acta Metall, 11 (1963), p. 203

CHAPTER 3

EXPERIMENTAL PROCEDURES

This chapter details the experimental procedures of this dissertation and also discusses the related results. Cu-Ag is chosen as a model system to experimentally test the models of super-diffusive nature of shear induced mixing and self-organization. There are a number of reasons to choose the Cu-Ag system. The thermodynamic properties of Cu-Ag are well documented for example in Ref. [1]. This system can be categorized as a moderately immiscible binary system with a positive heat of mixing of ≈6 kJ/mol for a $Cu_{50}Ag_{50}$ alloy. This system has already shown two extremes in behavior during BM experiments (fully mixed at or below room temperature and fully phase separated at 473 K) [2] within a temperature range that is easily accessible in real experiments. Moreover, MD simulations performed at 100 K have shown that shear induced mixing in Cu-Ag proceeds by dislocation glide across interface similar to pure Cu [3]. Using the Cu-Ag system we also avoid complexities arising from a large positive heat of mixing, a large mismatch in elastic properties, and different crystalline structures of the two phases. Thus, using a comparatively simple Cu-Ag system allows to better correlate the experimental results to the previous simulation predictions. Another favorable outcome of using the Cu-Ag system is that these phases provide good contrast in X-ray diffraction (XRD) and Z-contrast scanning transmission electron microscopy (STEM) due to their quite different atomic numbers and lattice constants. These will be discussed later in the section on the characterization techniques. The phase diagram of the Cu-Ag system [4] in

Figure 3.1 shows three equilibrium phases: (1) Liquid phase eutectic, (2) Ag rich phase (fcc) with maximum solubility of 14.1 at. % Cu, and (3) Cu rich phse (fcc) with a maximum solubility of 4.9 at. % Ag. The solubilities at room temperature are very limited. The eutectic point is at a composition of 39.9 % Cu and temperature of 779.1 °C [5].

In short, the Cu-Ag system is expected to show super-diffusive mixing behavior based on previous MD simulation results and is expected to self-organize into nanometer length scale compositional patterns at temperatures (~200-300 °C) which are suitable for SPD experiments.

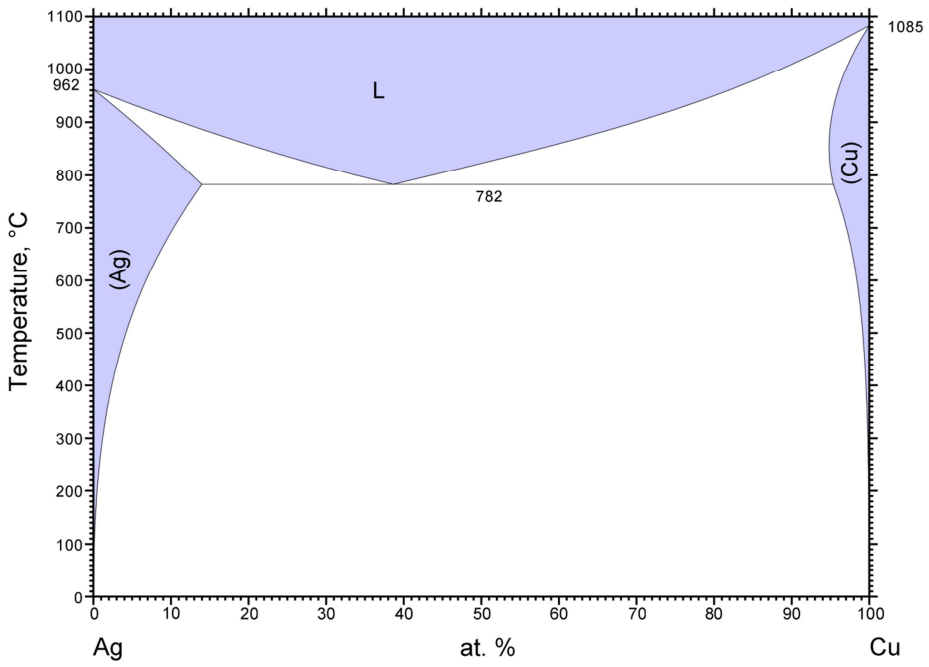

Figure 3.1. Ag-Cu binary equilibrium phase diagram [4]

3.1. SAMPLE PREPARATION

It has been shown by MD simulations that for super-diffusive nature of shear induced mixing the strain to mix scales linearly with the initial particle (or precipitate) size [6,7]. Also, we expect that the self-organization of a system under a given shearing rate and temperature is a dynamic steady state the system chooses regardless of the initial microstructural scale [8]. Therefore, to study the microstructural evolution in binary metal alloys by SPD it is critical to know the initial microstructural characteristics such as the grain size and second phase precipitate (or particle) size. Also there is a need to have varying initial microstructural length scales to study how shear induced mixing depends on the initial length scale and how the initial size affect the final steady state length scale the system chooses under steady state conditions of self-organization. For preparing such alloys high energy BM followed by hot pressing and annealing is used to prepare Cu-Ag binary alloys in bulk disk-shaped form. The details of each step are given in the following sections.

3.1.1. Ball milling at ambient and elevated temperatures

High energy BM was used to prepare the initial nanostructured powders of fully mixed Cu and Ag. Cu and Ag have already been shown to fully homogenize at or below room temperature BM [9]. Elemental powders of Cu (Alfa Aesar, 10 μm mesh size, purity 99.99 %) and Ag (Alfa Aesar 10 μm mesh size, purity 99.99 %) were mixed together in weight ratios corresponding to the composition of $Cu_{90}Ag_{10}$ by atomic percent. A dilute alloy is chosen so that the second phase Ag particles don't percolate and the length scales measured correspond to an individual particle, thus, avoiding

complexities arising from multiple connected particles. The $Cu_{90}Ag_{10}$ composition corresponds to Ag volume fraction of ≈0.14. The percolation threshold for site occupation in a 3D fcc lattice is 0.199 and for space occupation for spherical particles in a matrix is 0.15 (volume fraction) [10]. This mixture was subjected to high energy BM in a hardened steel grinding vial (Model # 8001 SPEX) using SPEX 8000M Mixer/Mill®. E52100 alloy steel hardened balls, 10 mm in diameter, were used as the grinding media. Roughly 5 grams of the powder mixture was ball milled in each batch and the ball to powder ratio was maintained at 4:1. Grinding vial body and cap liner are made of hardened tool steel which minimizes the iron contamination during BM. All powder handling and high energy BM experiments were carried out in a continuously purified argon glove box to minimize the oxygen contamination. Figure 3.2(a) shows the XRD scans of ball milled powder of Cu-Ag as a function of milling time. After 1 hour of BM, the Cu(111) peak is still close to pure Cu(111) peak indicating that very little Ag (< 1 %) has mixed into Cu. After 5 hours of BM the peak, however, has shifted very close to $Cu_{90}Ag_{10}$ solid solution position and, for 10 hours and above, the system is in fully mixed steady state. Figure 3.2(b) shows the solubility of Ag in Cu as estimated from peak shift of Cu (111). See Section 3.3.1. for experimental procedure detailing the crystallite size calculation from the peak broadening and estimation of solubility by the peak shift from the XRD data. All Cu-Ag samples to be compacted in this research were pre-mixed by 12 hours of BM to have a fully homogenized precursor powders.

High temperature BM of $Cu_{90}Ag_{10}$ powders at 125, 200, 300, and 400 °C was carried out in a glove box purified by continuously flowing nitrogen. The purpose was to compare the high temperature BM experiments (with unknown strain rate) with the HPT

experiments at the same temperature but with a known a strain rate. A 1-piece mica insulated band heater (Omega) was fitted tightly around the milling vial for heating purposes. A thermocouple was attached to the vial surface and a temperature controller was used to control the vial temperature. The temperature fluctuation was at most ± 10 °C at the highest milling temperature of 400 °C. The fluctuations were less at lower temperatures. The initial powders used in the high temperature BM experiments were either fully homogenized, 600 °C annealed, or as-received micron-sized powders. Nitrogen flowing through a liquid nitrogen reservoir was used to cool the vials immediately after the BM stopped.

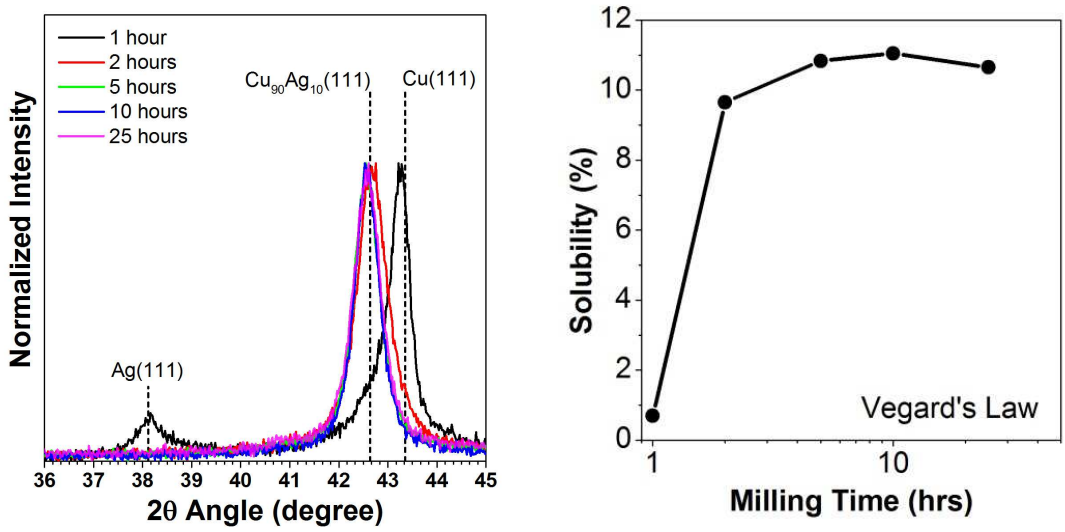

(a) (b)

Figure 3.2. (a) XRD scans of ball milled Cu-Ag powders as a function of milling time and (b) Ag solubility in Cu as a function of milling time as calculated from XRD (see Section 3.3.1.)

3.1.2. Hot pressing of samples

Bulk samples for HPT processing were fabricated from ball milled powders that were hot pressed under high vacuum. A compaction setup was custom built and connected with the argon glove box so that the ball milled powders can be transferred directly to the compaction setup without exposing them to the ambient atmosphere. This ensured that the powders are never exposed to the ambient atmosphere during any step of the process. The compaction setup consists of a hardened steel die with an inner diameter of 10 mm and a WC top and bottom punch. The top WC punch is attached to a steel bellow which allows it to move vertically while the whole setup remains hermetically sealed from the atmosphere. A side port is used to transfer the powder from the argon glove box to the die. The setup is pre-heated in argon atmosphere for about 2 hours using a heating tape wrapped around the die such that the temperature inside the die reaches ~300 °C. The ball milled powder is then transferred into the die and a turbo pump connected to the setup is used to achieve a high vacuum (2×10^{-6} Pa) within 10 – 1 5 minutes. A hydraulic pump is then used to press the powders under 1 GPa load for one hour. Roughly 5g of powder is used in each compaction cycle to give a ~10 mm diameter disk with ~6 mm height. This procedure gave bulk samples of $Cu_{90}Ag_{10}$ with relative densities of ≈98 % as measured from the Archimedes principle. During this procedure, the fully mixed ball milled powder undergoes chemical decomposition and Ag precipitates formed with a mean radius of ≈ 13 nm, as determined by STEM images (see Section 3.3.2. for experimental procedure for STEM). This as-pressed sample gives the smallest length scale in this research. Larger length scales were achieved by annealing these as-pressed samples at higher temperatures.

3.1.3. Annealing the as-pressed samples

For studying shear-induced mixing and self-organization behavior for different initial Ag precipitate sizes, the compacted samples were further annealed at 450, 600, and 750 °C for one hour in a tube furnace under a continuous flow of forming gas (95 % Argon, 5 % Hydrogen) using a heating rate of 10 °C/min. Figure 3.3 shows the as-pressed and annealed samples which are cut and polished. The Cu grain size and Ag particle size grew with the annealing temperature and, thus, the corresponding XRD scans in Figure 3.4(a) show the Cu and Ag peaks getting sharper. This annealing treatment leads to a number-averaged Ag precipitate radius of 22, 52, and 107 nm, respectively, as determined from STEM images (see Section 3.3.2. for experimental procedure). The corresponding volume-averaged initial precipitate radii, $R_{p,i}$, for the as-pressed and annealed samples were 16, 29, 61, and 131 nm. In this dissertation, these four samples will be identified by their initial volume-averaged precipitate (or particle) radius ($R_{p,i}$) or diameter ($D_{p,i}$)

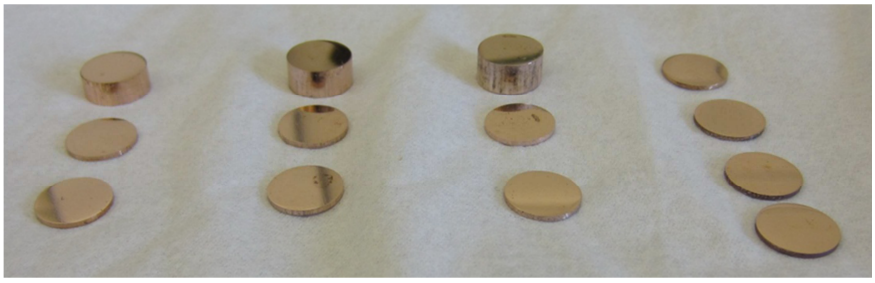

Figure 3.3. (from left to right) As-pressed and 450, 600, and 750 °C annealed samples of $Cu_{90}Ag_{10}$.

Figure 3.4(b) shows the Z-contrast STEM images of the as-pressed and annealed samples. The brighter particles are Ag and darker matrix is Cu. This contrast comes from

the different atomic number of Cu and Ag. The particle size distributions of each sample, determined by such Z-contrast STEM images by counting at least 200 particles, are shown in Figure 3.4(c). The distributions are characteristically log-normal. The mean particle sizes determined from the STEM images are consistent with those estimated by fitting of Ag(111) peak from the XRD data for the “as-pressed” and 450 °C annealed samples. For higher annealing temperatures, XRD underestimates particle sizes by as much as a factor of 2, suggesting that the Ag precipitates may be multi-grained. Moreover, presence of twins will underestimate the size by XRD.

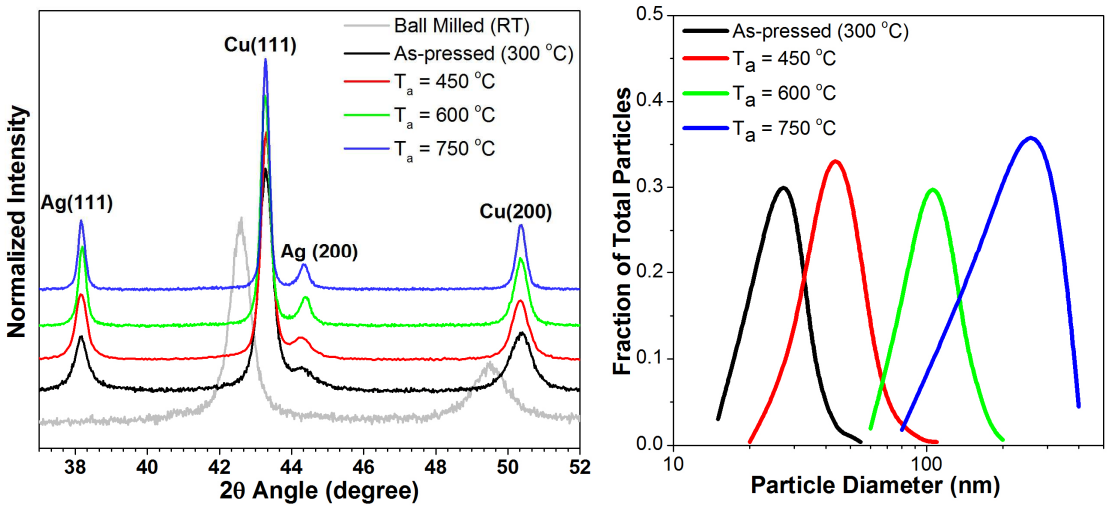

(a)

(b)

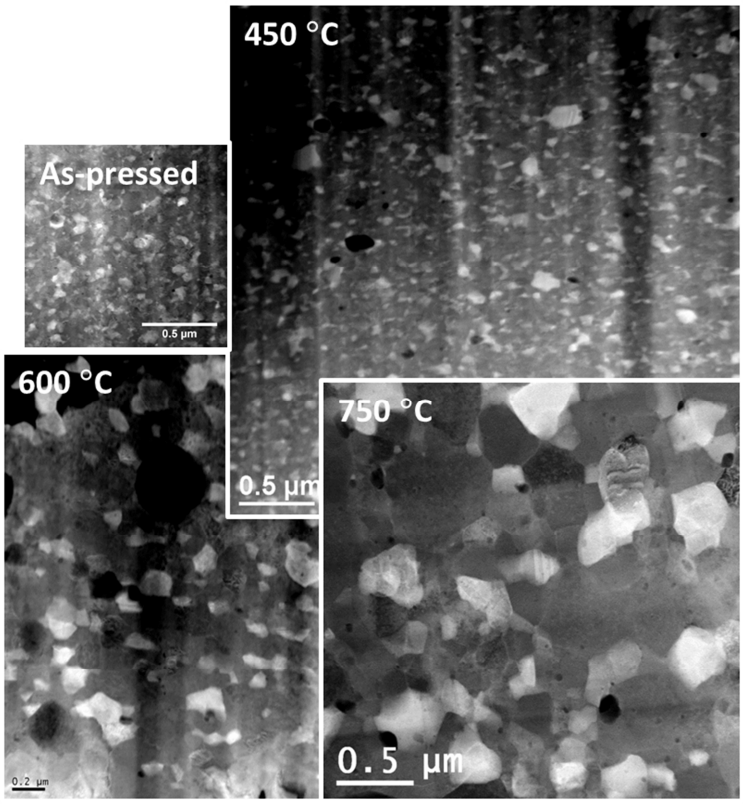

(c)

Figure 3.4. (a) XRD scans, (b) particle size distributions, and (c) Z-contrast STEM images (all images resized to same magnification) of the as-pressed and annealed $Cu_{90}Ag_{10}$ samples.

3.2. HIGH PRESSURE TORSION

The $Cu_{90}Ag_{10}$ samples were subjected to SPD by HPT in an unconstrained configuration. For this purpose, the samples were cut and polished into 250 µm thick disks. The choice of this sample geometry and unconstrained HPT configuration will be explained in the next section. The HPT was performed in a cyclic mode, i.e., rotating the anvils back and forth by 90° with an applied pressure of 4.5 GPa. One +90°/-90° back and forth anvil rotation constitutes one cycle. The number of cycles for room temperature HPT experiments ranged from 1.5 for the smallest initial Ag particle size ($R_{p,i}$ = 16 nm) sample to 9 for the largest initial Ag particle size ($R_{p,i}$ = 131 nm) sample. The rotation speed of anvil was 1.2 rpm for all room temperature experiments. Continuous cycle HPT was also employed to study the evolution of Ag size and shape with strain and to investigate which strain paths do Cu-Ag system follow to mix.

High temperature HPT experiments were done at 125, 200, 300, and 400 °C. The deformation rate was varied by changing the rotation speed of the anvil. Three deformation rates were used; 0.1, 1, and 6 rpm. The highest deformation rate was limited to 6 rpm due to the capability of the HPT machine. The slowest deformation rate of 0.1 rpm was limited by the time of the experiments as exposing the HPT anvils at high temperature for a long time was detrimental to the HPT setup. Nevertheless, these rotation speeds gave roughly a two orders of magnitude change in strain rate depending on the radial location selected on the samples. For the high temperature HPT experiments the number of cycles was 25 which corresponds to a total strain of ~1500 at a radial distance of r = 2 mm from the center of the disk. The choice of 25 cycles ensured that the samples were in steady state. Figure 3.5(a) provides a schematic of one half of the

sample. Shearing direction is along the transverse direction (TD). The other two directions are the radial (RD) and normal (ND) directions. Due to the unconstrained geometry, the initial sample thickness of 250 µm typically reduces to ~200 µm in the center, ~150 µm at r = 2 mm, and ~50 µm at r = 4 – 5 mm during HPT processing. The shear strain at any point is calculated according to:

Eq. 3-1 $\varepsilon = 2\pi rn/t$

where r is the radial position, n is the number of cycles, and t is the actual thickness of the sample at that position. A factor of 2 is not used for the back and forth cycle because it constitutes deformation by 180° which is one-half of the commonly used 360° continuous cycle of HPT. The samples thicknesses, measured in the scanning electron microscope (SEM), after room temperature HPT at different radial positions are shown in Figure 3.5(b). It should be noted that the samples are characterized from center to radial distances of at most ≈ 2 – 2.5 mm at which point the percent reduction in thickness is ~ 40 – 50 %. The samples near the edges had a percent reduction in thickness of at least 80 – 90 % and were not characterized to avoid uncertainties arising from a large thickness reduction. The origin of this variable sample thickness after HPT is not well known but it is reported that inhomogeneous elastic deformation of the anvil during high compression pressure contributes to this [11].

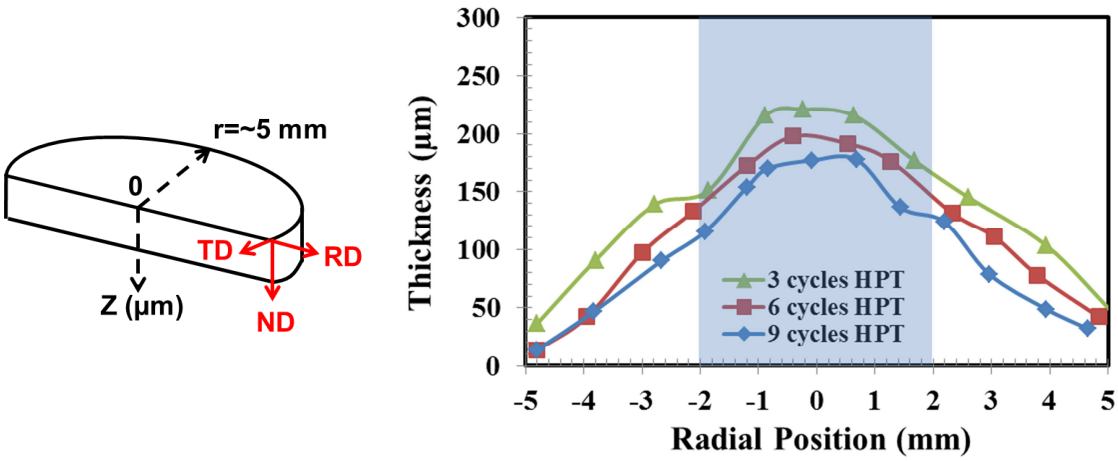

(a) (b)

Figure 3.5. (a) One half of the sample geometry showing transverse (shear) direction (TD), radial direction (RD), and normal direction (ND) of the sample deformed by HPT. (b) Sample thickness after HPT at room temperature for varying number of cycles. The characterization of the samples is done within the shaded region.

3.2.1. Optimization of the HPT

Accurate estimation of the strain in HPT processed samples at any given radial position requires that the sample is homogeneously deformed through thickness. As discussed in Chapter 2, constrained configuration during HPT results in inhomogeneous deformation through thickness with most of the deformation localized near surface. This limitation was overcome in this research by using unconstrained configuration. The homogeneity was confirmed using a series of through thickness TEM samples. Observation of the microstructure by STEM revealed that deformed particles exhibit uniform particle lengths (L_p) and morphology at all depths. Figure 3.6(a) shows the microstructures at different depths from the surface (given by the Z value in µm) and their corresponding Ag particle lengths. These TEM images were taken from the sample with $R_{p,i}$ of 61 nm deformed by 6 cycle of unconstrained HPT at room temperature. The

strain at this point is estimated to be 105. The shear strain is along the direction of the elongation of the Ag particles. Additionally, hardness measurements revealed uniformly high readings in these unconstrained samples independent of depth from the surface, whereas they showed negligible increase in hardness 15 – 20 μm below surface in samples processed in the constrained HPT geometry as shown in Figure 3.6(b). This clearly shows that the unconstrained sample has gone to much higher deformation and uniformly through thickness for the same number of cycles when compared to the sample deformed by the constrained configuration. One last comment to be made here is that the unconstrained HPT configuration resulted in a final sample thickness of about 200 μm at the center regardless of the initial sample thickness. So using an initially thick sample (e.g. 1 mm thickness) will result in significantly more compressive strain and material loss due to outward flow during torsion under compressive stress. It is reported [11] that an initial axial loading of the anvils (compression deformation) results in a small amount of material flow outwards with additional material flowing outward during torsional straining. During HPT in the constrained configuration, the amount the material flow depends on the initial sample thickness and the cavity size in HPT anvils. To minimize these effects, it was necessary to use initially thin samples (250 μm) as opposed to the thick samples (~1 mm) and deforming them by unconstrained configuration to have homogeneous deformation through thickness.

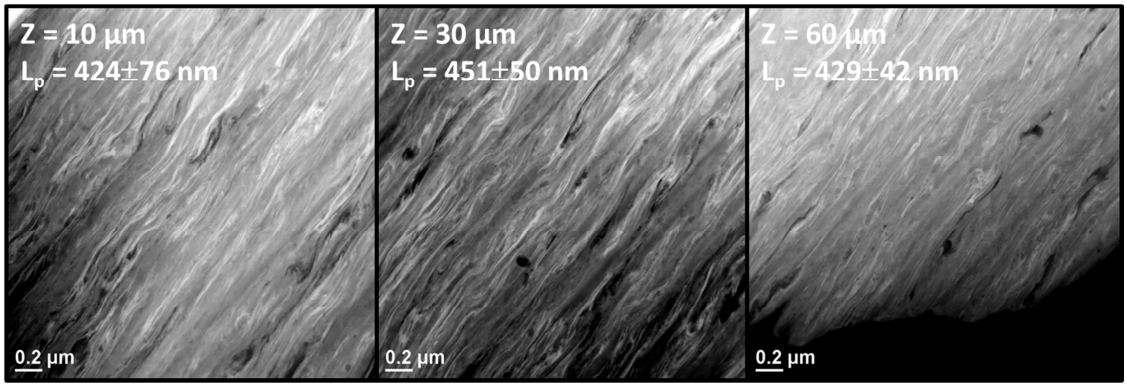

(a)

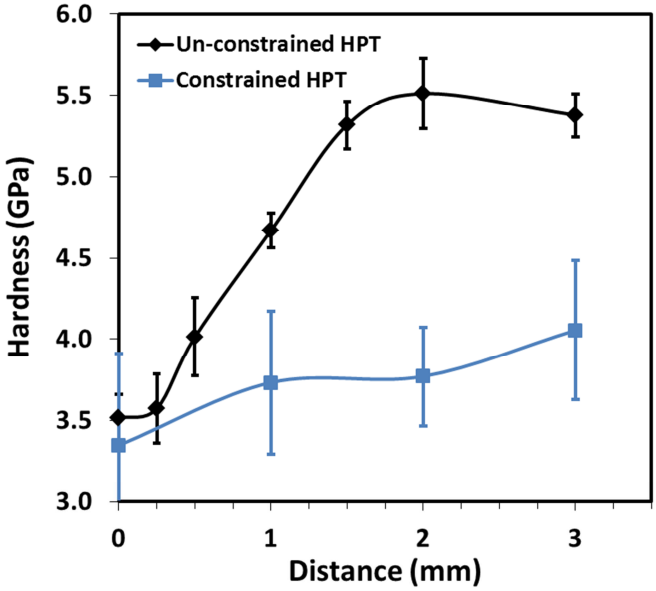

(b)

Figure 3.6 (a) Microstructural morphology in TD-ND plane of the sample with $R_{p,i}$ of 61 nm deformed by 6 cycles of unconstrained HPT at room temperature and (b) Mean hardness of the same alloy after unconstrained HPT at different radial positions.

3.3. CHARACTERIZATION

Accurate characterization of the microstructural morphology, length scales, and chemical composition is critical in this dissertation research. Typical microstructures are expected to be few tens of nanometer; therefore, characterization is a challenge. However, combination of a number of advanced characterization techniques, which complement each other, was useful. XRD probes a large volume of the sample and is useful to collect information statistically such as average crystallite size and solubility. Transmission electron microscopy (TEM) provide local structural and chemical composition with a very fine resolution (typically < 1 nm) but can be affected by averaging through thickness in case the length scales to be characterized (e.g. ~10 nm) are smaller than a typical TEM sample foil thickness (~ 40 – 100 nm). Atom probe tomography (APT) which provides a full 3D characterization of the sample will be used where it necessitates to study localized chemical information (which cannot be easily interpreted from TEM) e.g. during homogenization by SPD.

3.3.1. X-ray diffraction (XRD)

Characterization of the powder samples by XRD were done in SIEMENS/BRUKER D-5000 diffractometer using Cu K_α radiation in the Bragg-Brentano geometry. The X-ray source was operated at 40 kV tube voltage and 30 mA tube current. A small quantity of Si powder (Alfa Aesar, 10 μm mesh size, purity 99.9 %) was blended with the ball milled powders for the calibration of the peak positions during

analysis. The scans were typically done using an increment of 0.02° with a scan rate of 0.1 °/min.

Characterization of the bulk samples (compacted, annealed, and after HPT) by XRD were done using PANalytical/Philips X'pert MRD system using Cu K_α radiation with point focus optics. For HPT samples, the beam size was restricted to 1 mm x 1 mm and the scans were performed at different radial positions ranging from r = 0 mm to r ≈ 3 mm. The x-ray source was operated at 45 kV – 40 mA with a crossed-slit collimator in the primary optics, a parallel plate collimator in the secondary optics, a flat graphite monochromator and a proportional detector. The Ω-2θ scans were performed typically with a 0.02° step size with time at each step of 5 – 10 seconds. The sample stage rotates through an angle, Ω, while the detector rotates through an angle, 2θ. The offset angle defined as the difference between the Ω and θ angles is zero in these measurements so essentially these are θ-2θ scans. All samples were mechanically polished with a final vibrational polishing step using 0.02 μm SiC solution. Texture analysis was also done using the same machine using 1 mm x 1 mm beam. The axis conventions used in texture representation are shown in Figure 3.7. The shaded area is the measurement point and in this area the shear direction is nearly the same. The measured data was used to plot the pole figures, inverse pole figures, and orientation distribution functions using MTEX, which is a quantitative texture analysis tool for MATLAB [12]. The sample symmetry assumed is triclinic.

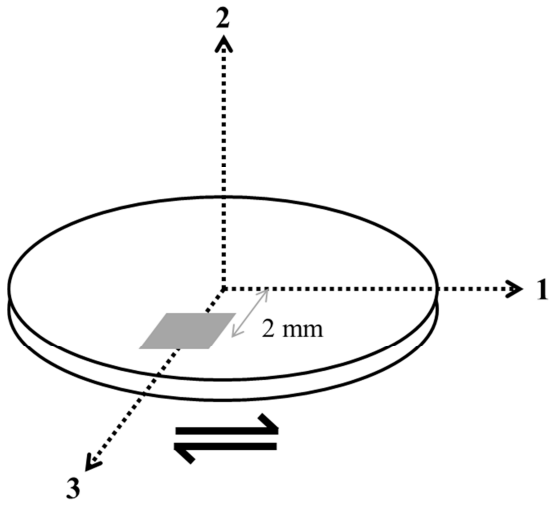

Figure 3.7. The axis convention used in the texture measurements with respect to the shear direction. The shaded region shows the area of measurement.

Crystallite size measurements and lattice constants were determined by peak fitting the data with MDI JADE 9.3. The peaks are fitted using a pseudo-Voigt function and crystallite sizes are measured using the Scherrer formula [13]:

Eq. 3-2 $$D = \frac{\kappa\lambda}{\beta \cos\theta}$$

where D is the mean crystallite size (diameter), κ is dimensionless shape factor of the crystallites taken to be 0.9, β is the full width at half maximum of the peak, λ is the X-ray wavelength and θ is the Bragg angle. The peak broadening can also be affected by the strain and other defects in the sample. Klassen et al. [9] worked on a similar system ($Cu_{50}Ag_{50}$) under variable temperature BM and found out that the powders ball milled at 316 K and 473 K had a root mean squared strain of only 1.0 % and 0.8 %, respectively, as determined by the Williamson and Hall method [14]. Because of the strain effect being so small it was ignored in the calculation of the crystallite size in this thesis. The

solubility is estimated by the peak position of Cu(111) using the modified Vegard's law [15]. Regular Vegard's law assumes that the lattice parameters do not deviate from that of an ideal solution. This assumption works well for systems such as Cu-Ag where the deviation from an ideal solution [16] is slightly positive. Nevertheless, the solubilities in this thesis are calculated from the modified Vegard's law which was calculated from rapidly quenched Cu-Ag alloys with varying composition [15].

3.3.2. Transmission electron microscopy (TEM)

TEM was performed by three different instruments. Bright field images and selected area electron diffraction patterns (SAED) were taken in JEOL (Japan Electron Optics Laboratory) 2010 LaB6. High angle annular dark field imaging (Z-contrast) and energy-dispersive X-ray spectroscopy (EDX) were carried out in JEOL 2010F STEM and an aberration-corrected JEOL 2200FS. 2010 LaB6 has a thermionic emission source whereas 2010F and 2200FS have a field emission source. The sample preparation technique for TEM is explained in section 3.3.5. All microscopes were operated at 200 kV.

The particle/precipitate radius for Ag in the as-prepared samples and after high temperature HPT were determined by Z-contrast STEM images. An image processing software, ImageJ [17], was used to trace out at least 200 particles and their area equivalent radii were calculated. The grain radius was measured from the bright field images using the linear intercept method [18] as $\frac{\omega \bar{l}}{2}$ where $\bar{l}$ is the length of the chord divided by the number of intersecting grain boundaries, and ω is a factor which depends

on the standard deviation of the grain sizes and their shape. In this thesis, it is assumed that $\omega = 1.5$ which is for monodisperse spherical grains [18]. The use of this shape factor is simplistic; however, the general trends of variation of grain radii with different conditions should remain the same.

3.3.3. Scanning electron microscopy (SEM)

High resolution SEM was performed in the Field Emission Inc. (FEI) dual beam focused ion beam (FIB) microscope (Helios NanoLab 600i) as a supplementary characterization technique e.g. to study microstructural homogeneity in high temperature HPT samples as a function of depth from the sample surface. Dual beam FIB microscope provided a convenient way of preparing a polished surface by ion milling at any radial or thickness position and in any orientation and immediately taking secondary electron and backscattered electron images. Cu and Ag provided a good contrast. This was very useful characterization technique for samples which had length scales ≈30nm or larger. A field emission JEOL 7000F SEM was also used to measure samples thicknesses after HPT.

3.3.4. Atom probe tomography (APT)

APT was performed at Northwestern University Center for Atom Probe Tomography (NUCAPT). This technique is based on the evaporation of an atom from a surface by an applied electric field which travels towards a position sensitive detector as shown schematically in Figure 3.8 for a local electrode atom probe (LEAP) which is the latest advancement of the APT technique. Needle shaped specimen allows large electric

field to develop at the tip causing atoms to ionize. This technique is very useful for studying 3D chemical composition of a sample and provides the atom's chemical identity and spatial coordinates for all the atoms detected from the sample with nearly atomic resolution. The spatial resolution of the LEAP® detection system is ~0.3 – 0.5 nm in the x-y plane and less than 0.1 nm along the tip axis (z-direction) [19]. The details of the APT can be found in these review articles [20,21].

APT data was collected on samples prepared by FIB milling. The samples were first transferred from atmosphere to the high vacuum buffer chamber. In the second step they were transferred to the ultra-high vacuum analysis chamber. APT tips with approximately 40 – 50 nm tip radii were analyzed at 60 K in a vacuum of ~5 x 10^{-11} using laser pulsing under a DC voltage of 1 – 4 kV. At least 10 – 15 million atoms were collected from each tip sample for statistical reliability. 1 nm^3 voxel based reconstructions for each tip were made from the raw data collected by LEAP® using Imago's (now Cameca) IVAS software.

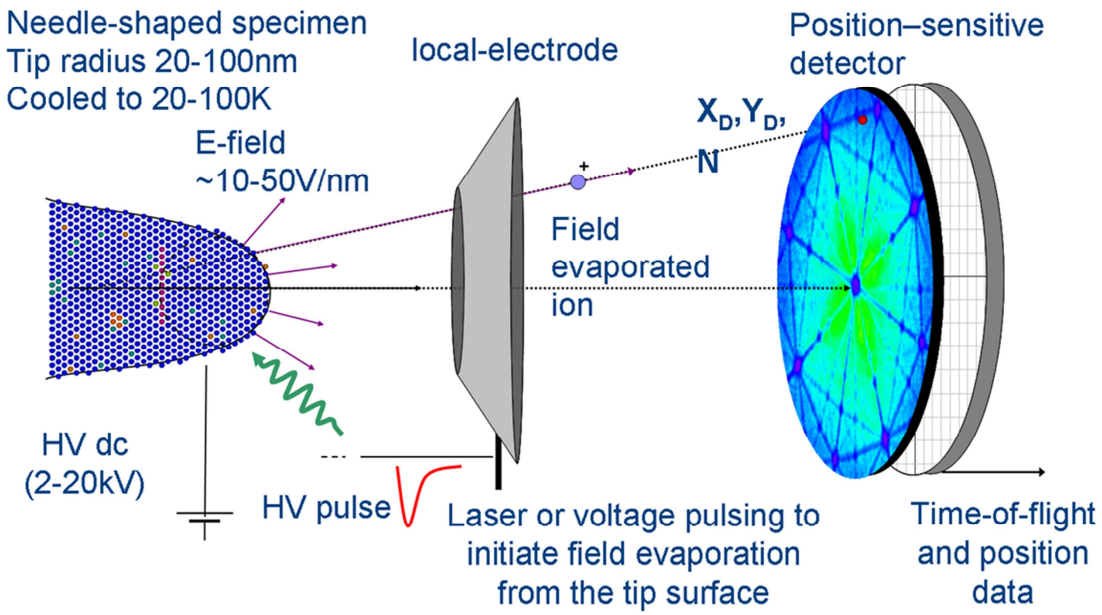

Figure 3.8. A schematic of local electrode atom probe (LEAP) [22].

3.3.5. Sample preparation for TEM and APT

Samples for TEM were prepared by either lift-off method [23] in FIB or by a combination of traditional mechanical polishing and FIB milling. The choice of method was dictated by the sample size, orientation of the TEM sample desired and the ease of obtaining multiple samples on a single HPT sample at different radial positions. For example, a single HPT sample was cut and polished into a wedge shape by using Allied MultiPrep^{TM} system. The top edge of the wedge was thinned down to approximately 15 – 30 μm. This wedge was mounted on a molybdenum TEM half grid using glue. FEI Dual Beam 235 or FEI Dual Beam Helios 600i FIB system was used to prepare location specific TEM samples on the wedge. This allowed using one TEM sample to characterize microstructure at varying strain and strain rates. These steps are illustrated in Figure 3.9(a). Cross-sectional TEM samples from HPT samples and annealed bulk samples were fabricated by the lift-off method in FIB. Similarly, for making APT tips, a diamond

cutting blade was used to make periodic cuts onto the edge of a wedge-polished sample revealing long pillars with width 50 – 100 μm. These pillars were subsequently thinned down to needle-shaped APT tips in FIB. Figure 3.9(b) illustrates these steps. The distance between tips on the same sample was typically 350 – 400 μm.

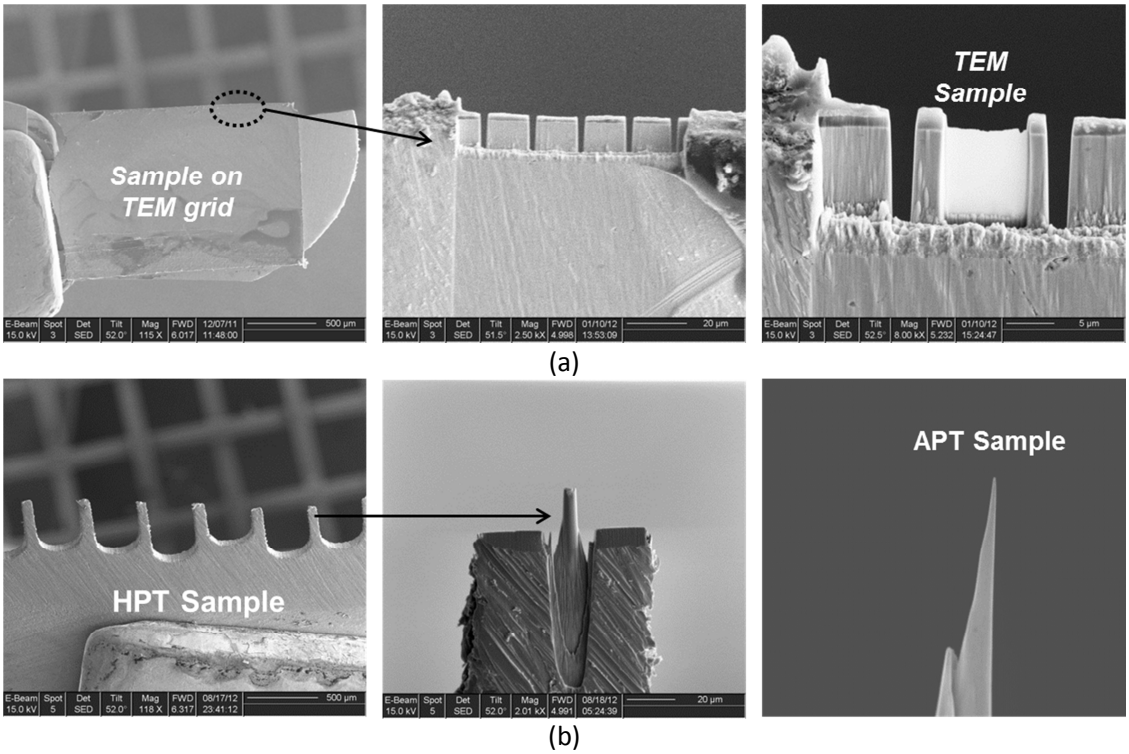

Figure 3.9. Typical steps involved in the preparation of (a) TEM sample and (b) APT sample using combination of traditional cutting/polishing and ion milling by dual beam FIB microscope.

3.3.6. Nanoindentation

Hysitron TI-950 Triboindenter was used to measure hardness by nanoindentation under load control. TI-950 is equipped with a patented three plate capacitive transducer which acts both as an actuator and a sensor. This transducer has a load resolution of < 1 nN with noise floor < 30 nN and a displacement resolution of < 0.02 nm with noise floor

< 0.2 nm. The drift is < 0.05 nm/sec. Electrostatic actuation needs very little current resulting in no drift due to heating. Displacement is concurrently measured by change in the capacitance. The instrument is fitted with a Berkovich diamond indenter. The samples were mechanically polished with a final vibrational polishing step using 0.02 μm SiC solution and mounted on steel pucks using a very thin layer of superglue which was cured overnight. Z-axis was calibrated by performing an air-indent before each session using 600 μN peak force. A standard Al(001) sample was used to calibrate optics-probe tip offset by indenting a H-pattern using peak force of 8000 μN and centering it in the current optics view. All testing was done from optics position with a peak load of 8000 μN, a loading and unloading time of 5 seconds, and a hold time at peak load of 5 seconds. Several indents were performed on a selected area. An automated method was setup to perform multiple indents on all the samples in a given session.

The hardness is calculated according to the equation:

Eq. 3-3 $$H = \frac{P_{max}}{A(h_c)}$$

where H is the hardness, P_{max} is the maximum load, and $A(h_c)$ is the contact area. The contact depth h_c is calculated according to:

Eq. 3-4 $$h_c = h_{max} - 0.75\frac{P_{max}}{S}$$

where S is the stiffness of the contact which is determined by the slope of the initial unloading part as shown in Figure 3.10. The tip area function $A(h_c)$ is calibrated by using a standard sample.

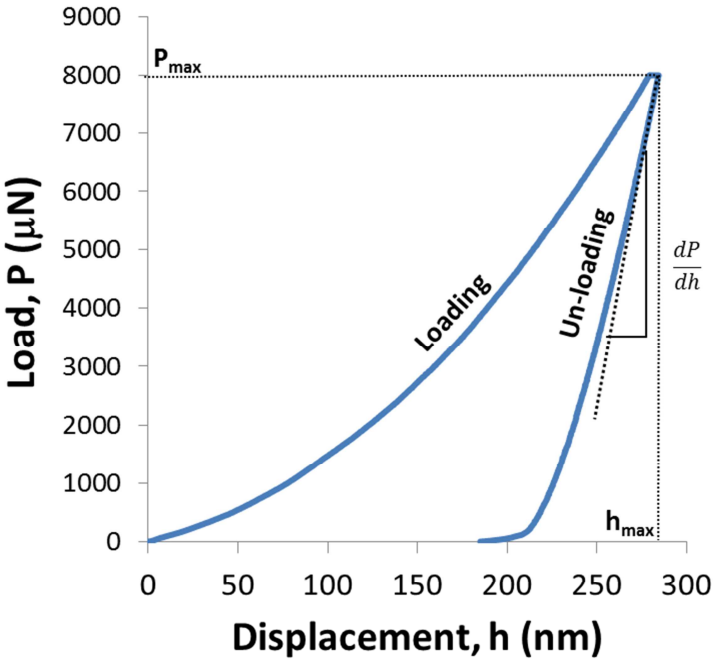

Figure 3.10. A typical loading and un-loading curve for the nanoindentation test of nanostructured $Cu_{90}Ag_{10}$ alloys in this thesis.

3.4. REFERENCES

[1] Najafabadi, R., Srolovitz, D. J., Ma, E. and Atzmon, M., J. Appl. Phys., 1993, 74, 3144.

[2] T. Klassen, U. Herr, R.S. Averback, Acta Mater. 45 (1997) 2921–2930.

[3] Y. Ashkenazy, N.Q. Vo, D. Schwen, R.S. Averback, P. Bellon, Acta Mater. 60 (2012) 984–993.

[4] ASM Alloy Phase Diagram Database.

[5] P.R. Subramanian, J.H. Perepezko, J. Phase Equil., 14 (1993), p. 62

[6] S. Odunuga, Y. Li, P. Krasnochtchekov, P. Bellon, and R. Averback, Physical Review Letters 95, 93-96 (2005)

[7] Y. Ashkenazy, N.Q. Vo, D. Schwen, R.S. Averback, and P. Bellon, Acta Materialia 60, 984–993 (2012).

[8] D. Schwen, M. Wang, R.S. Averback, and P. Bellon, In preparation.

[9] T. Klassen, U. Herr, and R. S. Averback, Acta Mater. 45, 2921 (1997).

[10] Harvey Scher and Richard Zallen, J. Chem. Phys. 53 (1970), 3759.

[11] R. Pippan, S. Scheriau, A. Hohenwarter, M. Hafok, Materials Science Forum 584-586, 16 (2008).

[12] http://code.google.com/p/mtex/

[13] A.L. Patterson, Phys. Rev. 56 (1939) 978–982.

[14] G.K. Williamson, W.H. Hall, Acta metall., 1 (1953), p. 22

[15] R.K. Linde, J. Appl. Phys. 37 (1966) 934.

[16] Najafabadi R., Srolovitz D.J., Ma E., Atzmon M., J. Appl. Phys. 74 (1993) 3144.

[17] http://rsb.info.nih.gov/ij/

[18] J.H. Han, D.Y. Kim, Acta Metall. Mater. 43 (1995) 3185-3188.

[19] D.N. Seidman, Annu. Rev. Mater. Res. 37 (2007) 127–158.

[20] T.F. Kelly, M.K. Miller, Rev. Sci. Instrum. 78 (2007) 031101.

[21] M.K. Miller, R.G. Forbes, Mater. Charact. 60 (2009) 461–469.

[22] Atom Probe Tomography, FIM and Atom Probe Group, Department of Materials, University of Oxford. http://www-fim.materials.ox.ac.uk/techniques.html

[23] Introduction to Focused Ion Beams, L.A. Giannuzzi and F.A. Stevie, 2005, pp 201-228. Springer.

CHAPTER 4

SHEAR INDUCED MIXING IN COPPER-SILVER

4.1. INTRODUCTION

As discussed in the Chapter 2, this dissertation research focuses on understanding the underlying mechanisms and evolution of the microstructure during processing of bulk nanocomposite alloys by severe plastic deformation (SPD) under controlled processing conditions. One key feature that will be discussed in this chapter is the forced chemical mixing of alloying elements. Sustained shearing is known to force chemical mixing and homogenization of immiscible elements in many alloy systems [1,2,3,4,5]. Forced chemical mixing refers to the athermal relocation of atoms induced by sustained shear deformation [6,7,8]. The mechanism explaining this mixing behavior is often attributed to the glide of dislocations [9,10,11], but the details of how such dislocation glide effects mixing remains an unresolved issue, and it is unlikely to be the same in all systems. Molecular dynamics simulations have shown, for example, that for systems such as Cu-Ag, dislocations transfer from one phase to the other and cause mixing while in others, such as Cu-Nb, this process does not occur [12]. While chemical mixing occurs in both systems, it is far more efficient in the former. In fact, it was pointed out that shear mixing is superdiffusive in systems like Cu-Ag, while merely diffusive in others [12]. By superdiffusive it is meant that the mean square relative displacements of pairs of atoms

increase faster than linearly with time (or strain). Superdiffusive mixing derives from the fact that the probability for a dislocation to pass between the two atoms, and cause their relative motion, is proportional to their distance apart, and this distance increases with time during shear deformation. For superdiffusive mixing, therefore, dislocations must transfer across phase boundaries.

One of the consequences of superdiffusive mixing behavior [12,13], is that the number of atoms leaving a precipitate of initial radius $R_{p,i}$, per unit strain, is proportional to $R_{p,i}^2$ rather than $R_{p,i}$, which is the case for diffusive processes. Accordingly, the characteristic plastic strain required to dissolve a monodisperse distribution of spherical particles, in absence of thermal diffusion, is [13]

Eq. 4-1 $$\Delta\varepsilon_{\mathrm{dis}} = \frac{16}{3}\frac{c_B(1-c_B)}{V_p}\frac{R_{p,i}}{b}$$

where c_B is the concentration of solute B, and V_p is the volume fraction of precipitates, b is the module of the Burgers vector. For diffusive processes, on the other hand, $\Delta\varepsilon_{dis}\ \alpha\ R_{p,i}^2$. For example, Eq. 4-1 suggests that the strain required to homogenize a two-phase $Cu_{90}Ag_{10}$ alloy with precipitate radii in the range 5 – 100 nm is 60 – 1200. It should be noted that Eq. 4-1 provides an upper bound for the strain required for dissolution as it includes only the dislocations geometrically necessary to achieve a given plastic strain [13].

In this thesis, the strain required for mixing in two phase $Cu_{90}Ag_{10}$ alloys as a function of initial precipitate radius ($R_{p,i}$) using high pressure torsion (HPT) experiments is measured, and confirm for this system both the linear dependence of $\Delta\varepsilon_{dis}$ on

precipitate size in Eq. 4-1 and its approximate magnitude. These experiments are done at room temperature so that the effects of thermal diffusion are negligible. The results will be discussed in light of the previous MD simulations and models [14,15,16,17] predicting the super-diffusive nature of mixing in Cu-Ag system in which the dislocations are expected to glide easily across coherent interfaces in response to applied shear. As discussed in the previous chapter $Cu_{90}Ag_{10}$ samples with four different initial Ag volume-averaged particle radii ($R_{p,i}$ of 16, 29, 61, and 131 nm) were prepared and deformed by HPT for 1.5 – 9 cycles. The selected number of cycles was dictated by the initial Ag radius; larger Ag particles require more cycles to fully mix. The strain at any radial position is given by $\varepsilon = \pi rn/t$. The thickness, t, also depends on the radial position, as demonstrated in chapter 3, decreasing with increasing r. Thus, the strain at any point should scale more than linearly with the radial position r. All strains were calculated by using the actual sample thickness at a given radial position. X-ray diffraction (XRD), Z-contrast scanning transmission electron microscopy (STEM) imaging and atom probe tomography (APT) were employed to quantify the mixing behavior. The experimental results will be interpreted in the context of previous MD simulation and model predictions.

4.2. MIXING BEHAVIOR WITH STRAIN

The strain dependence of mixing in $Cu_{90}Ag_{10}$ was initially measured by XRD since this technique probes a relatively large volume of the sample and is useful to collect information statistically such as average crystallite size and solubility. These results can be used to determine regions of interest for more detailed local TEM and APT

measurements. The scans were performed on the RD-TD plane at different radial positions from the center using 1 mm x 1 mm beam. A thin glass slide with a 1 mm x 1 mm window was used as a mask to block signal from the rest of the sample. The XRD scans on samples with $R_{p,i}$ of 16, 29, 61, and 131 nm deformed by 1.5, 3, 6, and 9 cycles of HPT, respectively, are shown in the Figure 4.1(a-d). The first thing to note is the shift of the Cu(111) peak position at different radial positions for all four samples. The shift of the Cu(111) peak with increasing radial distance results from variation in the lattice constant as Ag mixes into Cu. Using the modified Vegard's law [18], the condition for complete solubility was calibrated according to the lattice parameters of rapidly quenched metastable Cu-Ag alloys [19]. The Ag(111) peak, not shown Figure 4.1(a-d), also disappeared completely. In each sample, the Cu(111) peak measured from the center of the sample shows some shift toward the Ag(111), which is expected since the beam is scanning 1 mm x 1 mm area around the center has been deformed by shear. This also causes the samples with $R_{p,i}$ of 29, 61, and 131 nm to show an asymmetric peak from the center positions which is coming from a combination of a partially mixed Cu-Ag phase and a relatively un-mixed phase. With increasing radial distances (which corresponds to increasing shear strains) the peak shifts towards fully mixed $Cu_{90}Ag_{10}$ peak position. It should be noted that these scans were obtained after removing at least 20 – 30 μm surface layer, which was believed to show inhomogeneous deformation and damage from the HPT anvil surface. The samples were also shown to be homogeneously deformed through thickness as discussed in chapter 3.

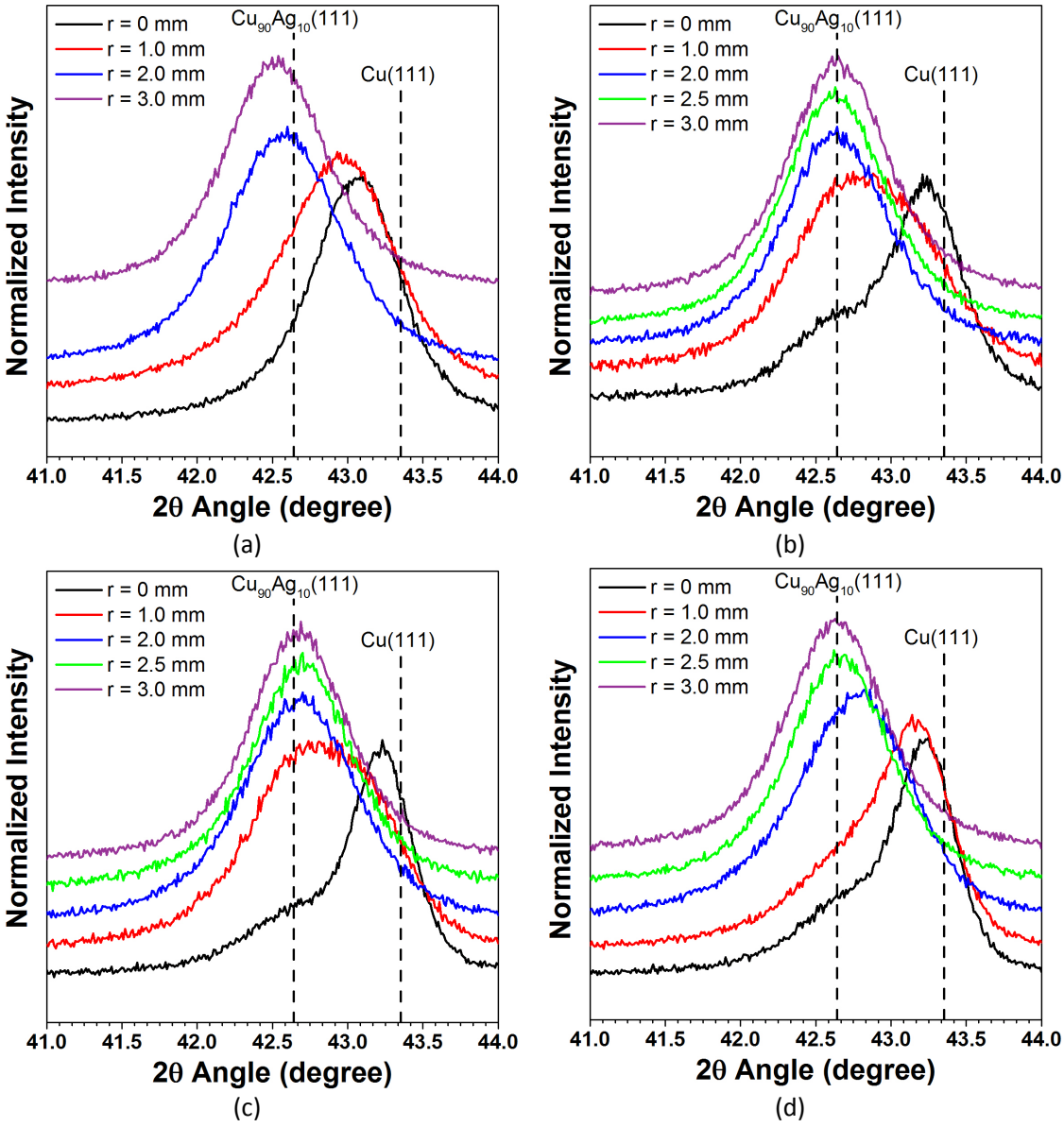

Figure 4.1. XRD scans at different radial positions, r, from the center for the samples with (a) $R_{p,i}$ of 16 nm with 1.5 cycles of HPT, (b) $R_{p,i}$ of 29 nm with 3 cycles of HPT, (c) $R_{p,i}$ of 61 nm with 6 cycles of HPT, and (d) $R_{p,i}$ of 131 nm with 9 cycles of HPT.

Figure 4.2 plots the solubility of Ag in Cu (%) as a function of strain as estimated from the shift of Cu(111) peaks in the XRD scans shown in Figure 4.1. The strain at each point was calculated by using the actual thickness of the sample at that point since the sample thickness decreases with the radial distance. A linear fit to these plots in the

unmixed region is shown as dashed lines and its intersection with a 10 % solubility horizontal line is taken as the approximate strain to mix. The characteristic strains for dissolving Ag precipitates deduced from these measurements are 60, 112, 280, and 712 for samples with initial $R_{p,i}$ of 16, 29, 61, and 131 nm, respectively. The copper grain size at these points estimated from the peak broadening and using Scherrer formula [20] is ≈11 nm for the samples with $R_{p,i}$ of 16 and 29 nm and ≈15 nm for the samples with $R_{p,i}$ of 61 and 131 nm, respectively. The Ag peak at r = 0 mm (center) after HPT becomes very small and completely disappears at r = 1 – 2 mm for all the samples.

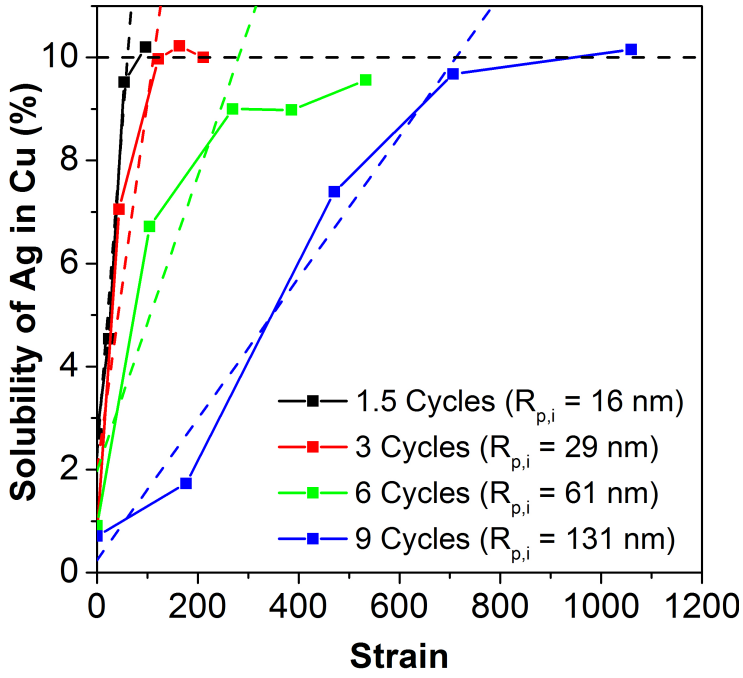

Figure 4.2. Solubility of Ag in Cu (%) versus strain for all four samples.

Another comment to be made here is about the rate of mixing of these particles, in terms of number of new Cu-Ag bonds per unit strain (or per unit time), which clearly depends on the initial particle size. It was shown in the MD simulations and the

geometrical calculations [21] that smaller particles mix faster than larger particles for the same volume fraction of particles. In fact, this mixing rate is proportional to $1/R_{p,i}$. Smaller particles have more interfacial area which is cut by dislocations, thus, the initial rate of A-B bond formation in the binary alloy is higher. This trend is shown in the Figure 4.2 where the slope in the unmixed region can be approximated as the rate of formation of new Cu-Ag bonds per unit strain (or time). This slope is inversely proportional to the initial Ag particle size.

4.3. GRAIN AND PARTICLE MORPHOLOGY WITH STRAIN

Figure 4.3 shows the bright field TEM images taken in RD-TD plane of the sample with $R_{p,i}$ of 61 nm sample deformed by 6 cycles of HPT. The refinement of the microstructure from a length scale on the order of 100 nm at $\varepsilon \sim 0$ to a length scale on the order of 10 nm at $\varepsilon > 174$ is clearly shown. The inset in each figure shows the selected area electron diffraction patterns (SAED) which change from a few brighter spots to more diffuse rings with increasing strain due to the refinement of the microstructure. The grain radii estimated from these images using the linear intercept method is 36, 27, 17, and 8 nm at strains of ~0, 48, 174, and 386, respectively. The final grain radius of 8 nm is consistent with that measured from the XRD.

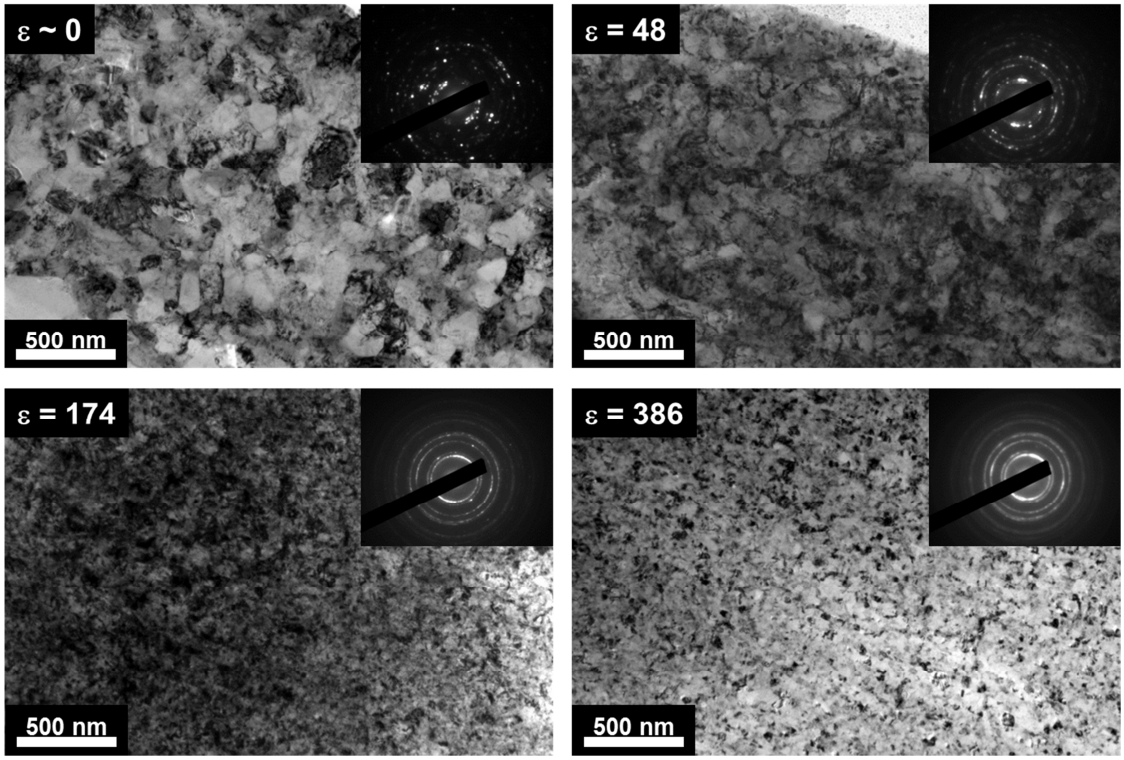

Figure 4.3. Bright field TEM images in RD-TD plane and the corresponding SAED patterns of the sample with $R_{p,i}$ of 61 nm deformed by 6 cycles of HPT at strains of ~0, 48, 174, and 386.

Figure 4.4 shows the Z-contrast STEM images (in RD-TD plane) of the sample with $R_{p,i}$ of 61 nm at different strains. The mixing of Ag particles is clearly evident with increasing strain, with complete mixing obtained at a strain of 269, which is close to that predicted by XRD. Some bright spots persist in the STEM images taken from samples at a strain of 269; however, EDX analysis confirms that the composition is constant across these regions. These results indicate that the samples mix to a degree that the alloy is homogenous over a length scale of 5 – 14 nm which is considerably smaller than the thickness of the TEM sample, typically ≈ 40 – 100 nm. However, it should be noted that the inner semi angle of the annular dark field detector in JEOL 2010F is 30 – 40 mrad which results in some diffraction contrast. In the next chapter, an aberration corrected

microscope (JEOL 2200FS) will be used for characterizing samples of high temperature HPT of Cu-Ag. This microscope has a much larger inner semi angle of 200 mrad for the annular dark field detector which significantly reduces the diffraction contrast. In this chapter, we are interested in calculating the strains at which the samples fully mix which requires characterization of the local chemical environment around a single Cu or Ag atom. The samples will be fully mixed when the maximum number of Cu-Ag bonds possible is formed. This level of resolution can be obtained by APT which was used for the samples with initial $R_{p,i}$ of 16 and 61 nm to confirm the strain to mix.

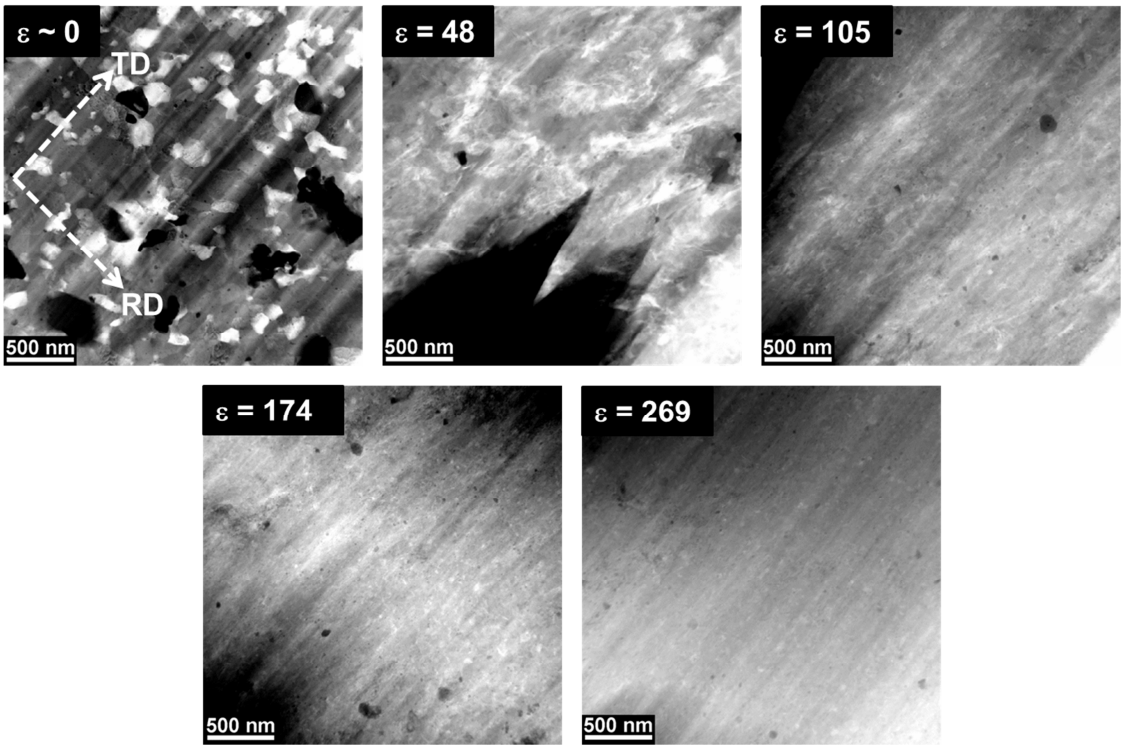

Figure 4.4. Z-contrast STEM images in RD-TD plane of the sample with initial $R_{p,i}$ of 61 nm deformed by 6 cycles of HPT at strains of ~0, 48, 105, 174, and 269. The RD and TD directions are indicated for the first image and they are same for all the images.

4.4. HOMOGENIZATION ON ATOMIC SCALE

Defining homogeneity depends on the length scale of observation. XRD and STEM are limited by the coherence length of the incident X-rays and averaging of electron scattering through thickness, respectively. For example, STEM images confirmed that the alloy is homogenous over a length scale of 5 – 14 nm which is considerably smaller than the thickness of the TEM sample, typically ≈ 40 – 100 nm. There was a need to examine the compositional homogeneity at finer length scales than that possible by either XRD or STEM. This was achieved by making use of APT which was carried out at Northwestern University Center for Atom-Probe Tomography (NUCAPT).

Imago (now Cameca) Visualization and Analysis Software (IVAS) software was used to create reconstructions from the raw data collected for each tip-shaped specimen. The initial data collected (typically one million atoms) was not used in the reconstructions. During initial collection the tip sometimes need fine tuning and alignment. There is also contamination near the surface such as oxides, moisture, and other gas adsorption. Milling in the FIB induces Ga contamination which is concentrated near the tip. Each reconstruction typically had 7 – 10 million atoms. After creation of the reconstructions which has coordinates and identity of all the atoms analyzed by binning the atomic positions into 1 nm^3 voxels. These voxels can be analyzed in terms of the density of atoms within them and their average composition. Figure 4.5 plots the distribution of the number of atoms in each voxel used in the reconstructions of all of the tips from samples with initial $R_{p,i}$ of 61 nm. Cu and Ag have atomic density of 85 and 59 atoms/nm^3, respectively. A $Cu_{90}Ag_{10}$ alloy should have 82 atoms/nm^3 and with a LEAP

detector efficiency of ≈50 % [22], the expected number of atoms per voxel distribution should peak around ≈ 41 atoms/voxel as shown in the Figure 4.5.

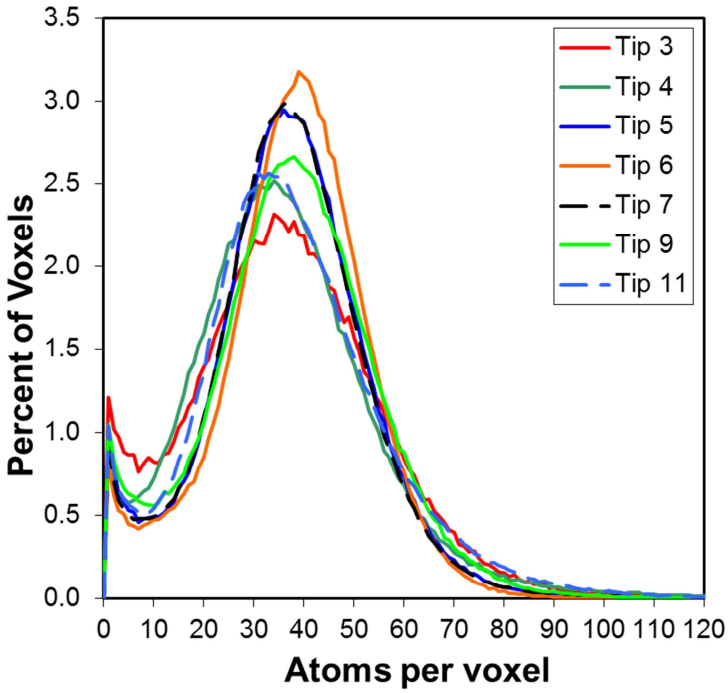

Figure 4.5. Distribution of the number of atoms in each voxel from the reconstructions of 7 tip-shaped samples taken from the sample with $R_{p,i}$ of 61 nm deformed by 6 cycles of HPT.

Similarly, local concentrations of Ag can be obtained from the 1 nm^3 voxels. Figure 4.6 plot the distribution of local Ag concentration for sample with $R_{p,i}$ of 61 nm deformed by 6 cycles of HPT. The inset shows the reconstruction of each tip, where the color in the reconstruction defines the average composition of the voxel. For example, red represent voxels with 94 – 100 % Ag atoms while blue voxels represent compositions of 0 – 6 % Ag atoms. The seven curves in Figure 4.6(a) can be roughly divided into four subgroups. Tips with strain of 79 and 130 display two peaks near 0 – 5 % and 95 – 100 % Ag indicating a decomposed microstructure with nearly pure Cu and Ag phases

persisting. The nominally ‘pure’ Ag disappears at a strain of 181, but significant chemical heterogeneity persists. Tips at strains of 253 and 340 produce similar distributions that contain no voxels with silver in excess of 45%, but display nanoscale heterogeneity. Finally, tips at strains of 556 and 1127 appear compositionally homogeneous and produce voxelized composition distributions similar to the Poisson distribution. The variation in the atomic density of the voxels, as noted in the Figure 4.5, was accounted for when calculating this Poisson distribution (dotted curve in Figure 4.6). Thus, with increasing strains, the decomposed microstructure evolves to fully mixed (random), approaching a Poisson distribution at strains of 556 and above. Consistent results at strains of 556 to 1127 indicate that steady state has been achieved with the sample being compositionally homogeneous on atomic scale.

Figure 4.7 plots the distribution of local Ag concentration for sample with $R_{p,i}$ of 16 nm deformed by 1.5 cycles of HPT. This sample initially shows increased mixing with increasing strain but the voxelized distribution never reaches a compositionally homogeneous steady state as for the sample with $R_{p,i}$ of 61 nm. This might be due to the fact that this sample is only deformed by 1.5 cycles and heterogeneity in strain may persist at larger radial distances. This sample was not used in further analysis but it does highlight the fact that there might be minimum number of cycles needed to achieve uniformly increasing deformation radially.

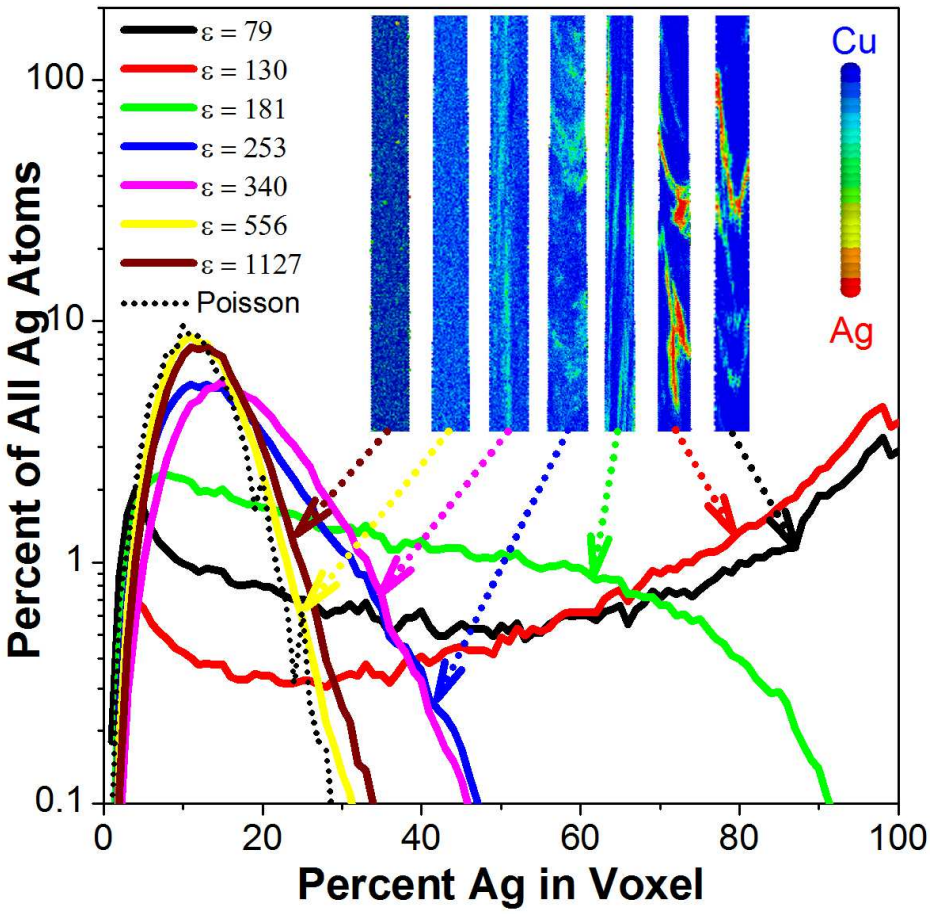

Figure 4.6. Percent of All Ag atoms versus percent Ag in voxels for different amount of strains for the sample with $R_{p,i}$ of 61 nm deformed by 6 cycles of HPT. Inset shows 1 nm^3 voxel based reconstruction of the tips corresponding to each plot.

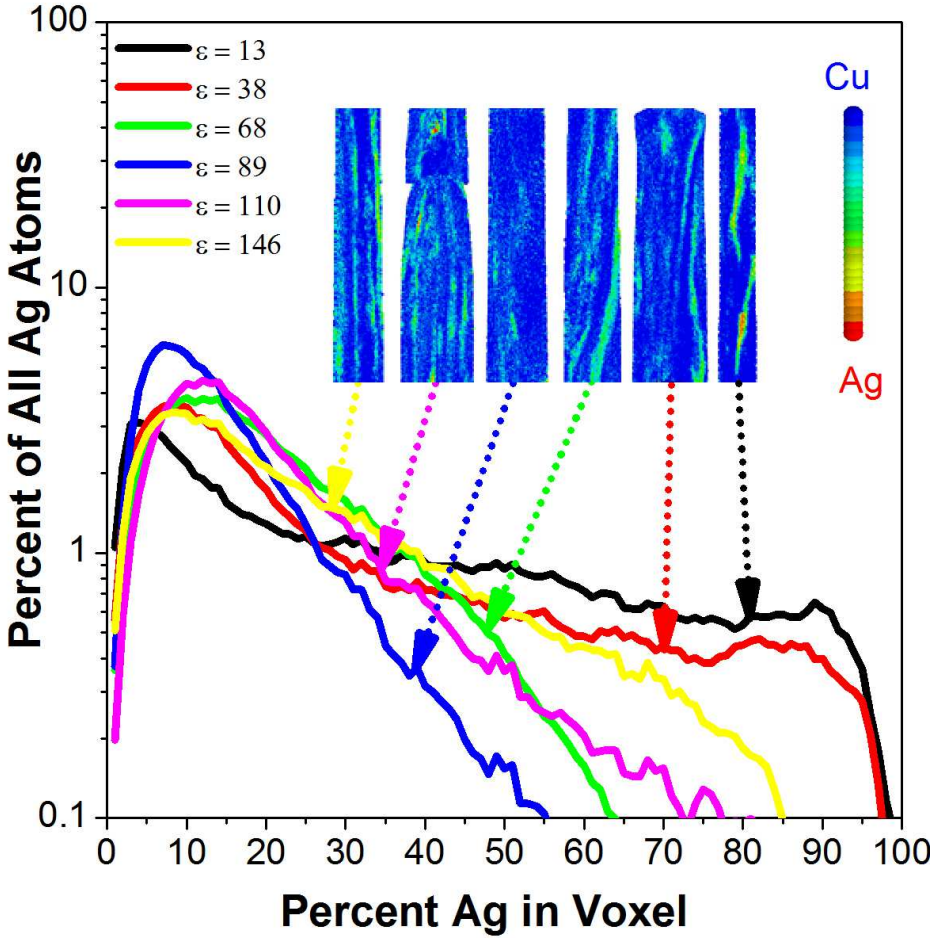

Figure 4.7. Percent of All Ag atoms versus percent Ag in voxels for different amount of strains for the sample with $R_{p,i}$ of 16 nm deformed by 1.5 cycles of HPT. Inset shows 1 nm^3 voxel based reconstruction of the tips corresponding to each plot.

Figure 4.8 plots the distribution of local Ag concentration for the sample with $R_{p,i}$ of 16 nm deformed by 3 cycles of HPT. It is seen that at strains of 184 and 268 the sample appears compositionally homogeneous and produce voxelized composition distributions similar to the Poisson distribution. Only 4 tips were analyzed in this case but they all represent different stages in the evolution of the sample to fully random state which was confirmed by the sample with strain of 268.

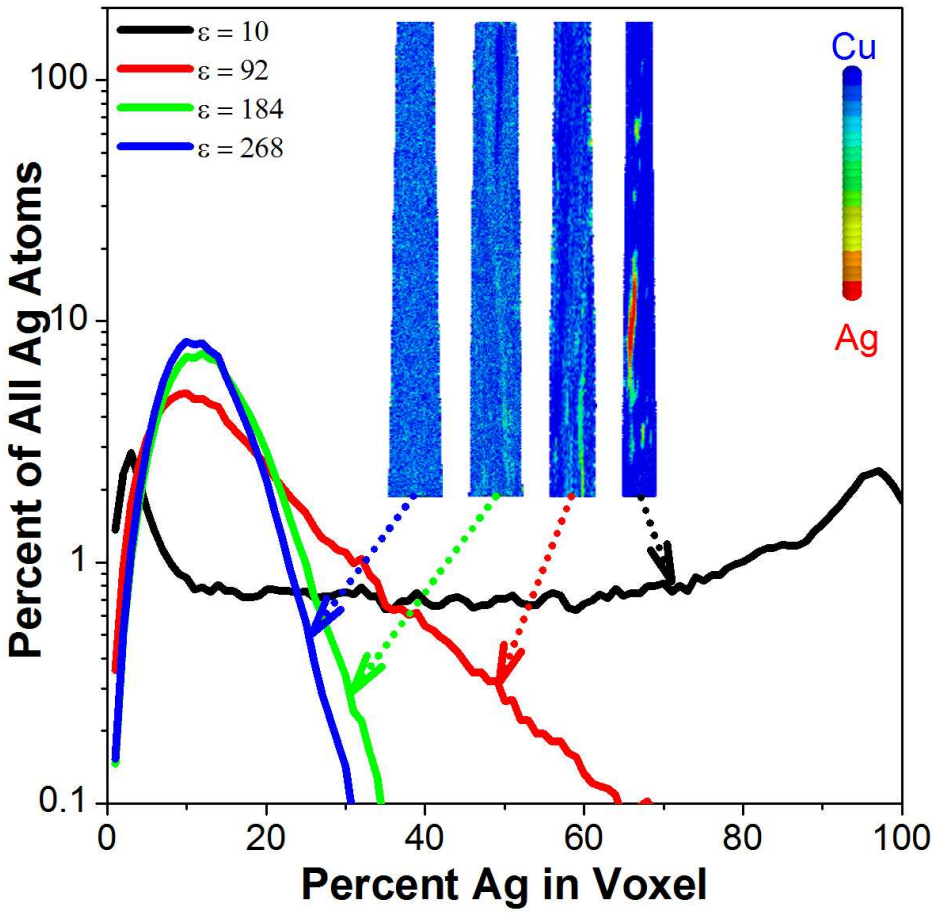

Figure 4.8. Percent of All Ag atoms versus percent Ag in voxels for different amount of strains for the sample with $R_{p,i}$ of 16 nm deformed by 3 cycles of HPT. Inset shows 1 nm^3 voxel based reconstruction of the tips corresponding to each plot.

4.5. STRAIN TO MIX

From the APT data it is confirmed that the samples fully mix and the distribution of the Ag atoms approaches Poisson distribution. Further analysis can be performed on the APT data such as determining the radial distribution of Cu and Ag atoms as a function of distance from either a Cu or Ag atom. This radial distribution is plotted as bulk normalized concentration as a function of distance from Ag atom for the sample

with $R_{p,i}$ of 61nm deformed by 6 cycles of HPT and is shown in Figure 4.9(a). Ag bulk normalized concentration of more than 1 and Cu bulk normalized concentration of less than 1 means the sample is not compositionally homogeneous in the localized environment around the Ag atoms. With increasing strains, these bulk normalized concentrations approach unity i.e. the number of Cu-Ag bonds maximize and the system is completely mixed. From such radial distributions the total number of nearest neighbor Cu-Ag bonds can be calculated as a function of strain, which is plotted in Figure 4.9(b), normalized by the total number of Cu-Ag bonds required for complete solid solution. The number of Cu-Ag bonds increases with increasing strain and saturates at a value consistent with a complete solid solution. We define the strain to mix ($\Delta\varepsilon_{dis}$) by the intersection of the two regimes (strain of 307 and 92 for the samples with $R_{p,i}$ of 61 and 16 nm, respectively). It should be noted again that the sample with $R_{p,i}$ of 16 nm deformed by only 1.5 cycles does not homogenize at larger strains but with 3 cycles it does. We attribute this anomalous behavior to an artifact associated with our unconstrained HPT geometry. Material at larger radial positions flows outward during the early stages of HPT. It is very likely therefore, that this region was not homogeneously strained for 1.5 cycles of HPT. It should be noted that all other specimens were deformed by more than 3 cycles.

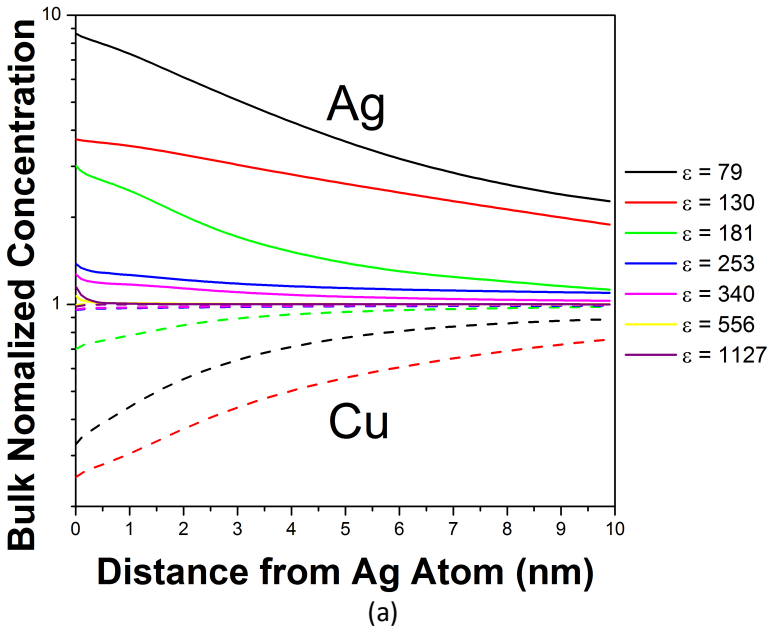

(a)

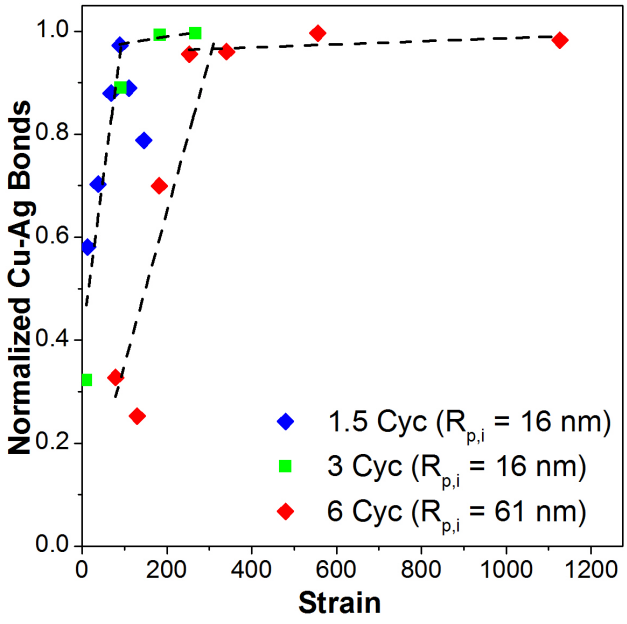

(b)

Figure 4.9. (a) Radial distribution of bulk normalized concentration as a function of distance from Ag atom for the sample with $R_{p,i}$ of 61nm deformed by 6 cycles of HPT and (b) Normalized number of Cu-Ag bonds as a function of strain for the sample with $R_{p,i}$ of 16nm with 1.5 cycles (♦) and 3 cycles (■), and the sample with $R_{p,i}$ of 61 nm with 6 cycles (♦) of HPT.

The strain to mix calculated from the XRD and APT technique is summarized in the Figure 4.10. Also shown is the comparison to the model prediction as given in Eq. 4-1.

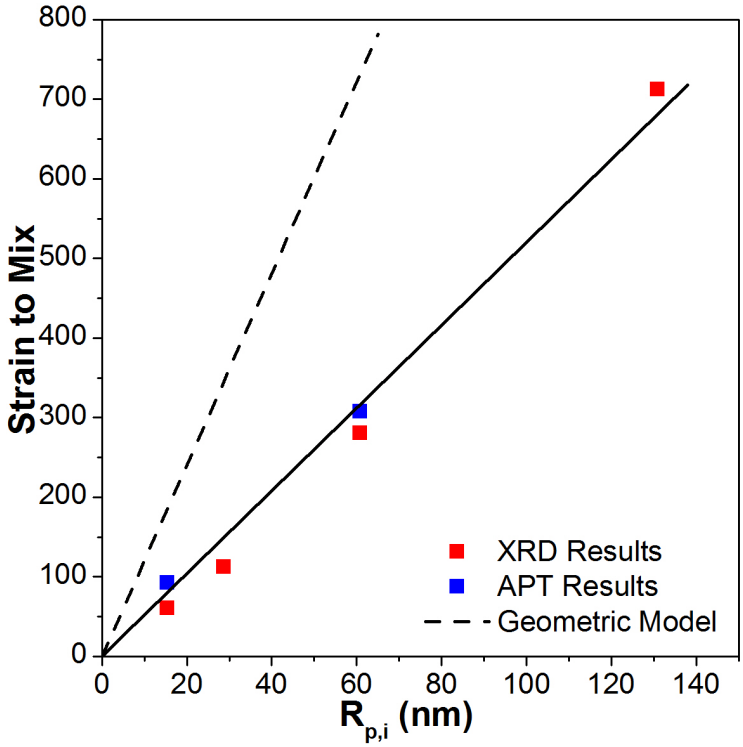

Figure 4.10. Strain to mix, $\Delta\varepsilon_{dis}$, versus initial particle radius, $R_{p,i}$. The dashed line is the model prediction from Eq. 4-1.

A number of things can now be concluded. It is seen that the experimental values of $\Delta\varepsilon_{dis}$ increase linearly with $R_{p,i}$ in accordance with the prediction of Eq. 4-1. The magnitude of these values are also seen to agree reasonably well with the prediction of Eq. 4-1, to within a factor of two. There are a number of reasons for this difference of a factor of two. Firstly, Eq. 4-1 provides an upper bound for $\Delta\varepsilon_{dis}$, as not all dislocations contribute to macroscopic strain. Secondly, Eq. 4-1 assumes random shearing, whereas the HPT strain path is predominantly cyclic simple shear in the RD-TD plane. No stable

crystal orientation exists for cubic crystals deformed by simple shear in materials with non-zero strain rate sensitivity [23]. As a consequence, it is expected that the crystallographic shear planes will be largely randomly oriented. Nevertheless, deviations from random shearing may play some role. Eq. 4-1 assumes the precipitates are compact spheres, but Figure 4.4 shows that the shapes are somewhat distorted. Lastly, the formula for HPT strain overestimates the actual strain due to sample thickness reduction and material flow outwards. The possible effect of the initial precipitate shape on the rate of mixing is derived geometrically below in a simplistic way.

4.6. NUMBER OF NEW A-B BONDS PER UNIT STRAIN ON SHAPE

The shape of the initial Ag particle will affect the rate of mixing and the total strain to mix it. For example, we expect the initial rate of mixing of a spherical particle, which has a minimum surface area to volume ratio, to be less than for example an ellipsoid. The Ag particle has compressed to about 40% at a radial distance of ≈2 mm. Let's estimate the effect of the initial shape of the precipitate on the initial rate of mixing. The Figure 4.11 shows a cube precipitate with edge length 'a' within a cube grain of edge length 'L'. Also shown is a distorted precipitate; let's assume an orthorhombic shape of the precipitate with dimensions na x na x ma within an orthorhombic grain of dimensions nL x nL x mL. mn^2 is 1 so volume is preserved. The number of bonds per unit strain is estimated for each shape below when a dislocation passes randomly through the grain in one of the randomly selected three orthogonal directions.

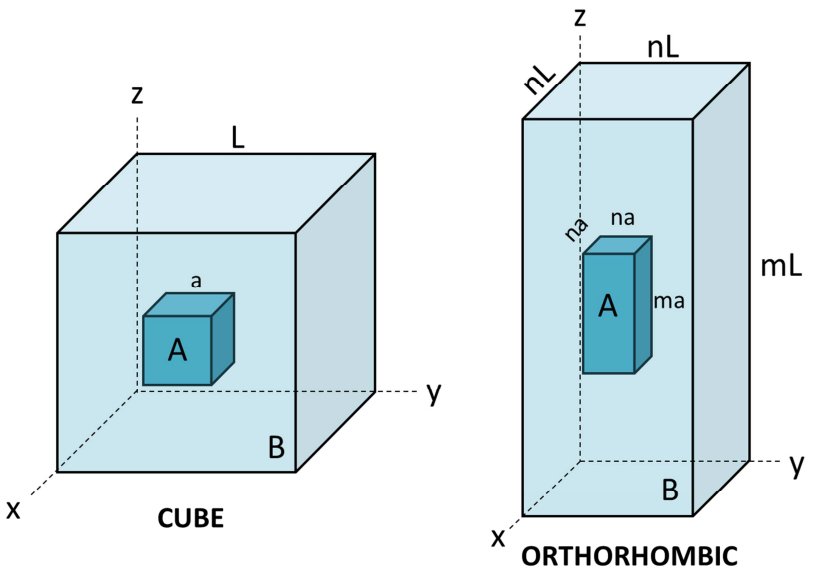

Figure 4.11. A cube precipitate with edge length 'a' inside a cube grain of edge length 'L'. The same cube stretched into an orthorhombic such that the precipitate now has dimensions of na x na x nL and the grain has dimensions of nL x nL x mL. $mn^2 = 1$ so volume is preserved.

CUBE:

For each passage of dislocation through the cube, the average strain $\varepsilon = \frac{a}{L}\left(\frac{b}{L}\right)$ where b is the magnitude of the Burgers vector and the factor a/L accounts for the probability of the dislocation cutting the cube precipitate. The strain is the same whether the dislocation is cutting in the x, y or z-directions. The number of new A-B bonds formed due to the passage of this dislocation through the cube precipitate is $N_{b,cube} = 2\left(\frac{a}{b}\right)$.

Thus, the number of bonds per unit strain is:

Eq. 4-2 $$\frac{N_{b,cube}}{\varepsilon} = \frac{2a^2}{b^2}$$

ORTHORHOMBUS:

For each passage of dislocation through the orthorhombus, the corresponding strains in all three directions are:

$$P_z\varepsilon_z = \left(\frac{mL}{(m+2n)L}\right)\left(\frac{a}{L}\right)\frac{b}{mL}, \quad P_x\varepsilon_x = \left(\frac{nL}{(m+2n)L}\right)\left(\frac{a}{L}\right)\frac{b}{nL}, \quad P_y\varepsilon_y = \left(\frac{nL}{(m+2n)L}\right)\left(\frac{a}{L}\right)\frac{b}{nL}$$

Where P_x, P_y and P_z are the probabilities of the dislocation cutting the precipitate in x, y, and z-directions, respectively. $P_x\varepsilon_x$ and $P_y\varepsilon_y$ are equal. Thus, the average strain per dislocation $\varepsilon = \left(\frac{b}{L}\right)\left(\frac{1}{(m+2n)} + \frac{2}{(m+2n)}\right) = \left(\frac{b}{L}\right)\left(\frac{3}{(m+2n)}\right)$. For a cube (m = n = 1) this relationship would reduce to Eq. 4-2.

The number of new A-B bonds formed due to the passage of this dislocation

$$N_{b,ortho} = P_z\left(N_{b,ortho}\right)_z + 2P_x\left(N_{b,ortho}\right)_x$$

$$\left(N_{b,ortho}\right)_z = \frac{mL}{(m+2n)L}\left(\frac{a}{L}\right)\frac{2na}{b} = \left(\frac{m}{m+2n}\right)\left(\frac{2a^2}{bL}\right)n$$

$$2\left(N_{b,ortho}\right)_x = 2\frac{nL}{(m+2n)L}\left(\frac{a}{L}\right)\frac{(m+n)2a}{2b} = \left(\frac{n}{m+2n}\right)\left(\frac{2a^2}{bL}\right)(m+n)$$

Therefore, $N_{b,ortho} = \left(\frac{2a^2}{bL}\right)\left[\frac{mn}{m+2n} + \frac{mn}{m+2n} + \frac{n^2}{m+2n}\right] = \left(\frac{2a^2}{bL}\right)\left[\frac{n(2m+n)}{m+2n}\right]$

The number of bonds per unit strain $\frac{N_{b,ortho}}{\varepsilon} = \left(\frac{\left(\frac{2a^2}{bL}\right)\left[\frac{n(2m+n)}{m+2n}\right]}{\left(\frac{b}{L}\right)\left(\frac{3}{m+2n}\right)}\right) = \left(\frac{2a^2}{b^2}\right)\left[\frac{n(2m+n)}{3}\right]$

Eq. 4-3 $$\frac{N_{b,ortho}}{\varepsilon} = \left(\frac{2a^2}{b^2}\right)\left[\frac{2}{3}\sqrt{m} + \frac{1}{3m}\right]$$

The Figure 4.12 plots Eq. 4-3 and its first derivative as a function of m. For example, if the value of m = 0.2, the number of bonds per unit strain increases by a factor of 2. The shaded portion in the Figure 4.12 represents m values in the range 0.1 – 0.4 in which the number of bonds per unit strain increases rapidly with decreasing m. The first derivative in this region shows the sensitivity of number of bonds per unit strain to the shape of the Ag precipitate. The behavior is also more sensitive when the particles are compressed (values of m less than 1) as is encountered in the present high pressure torsion experiments.

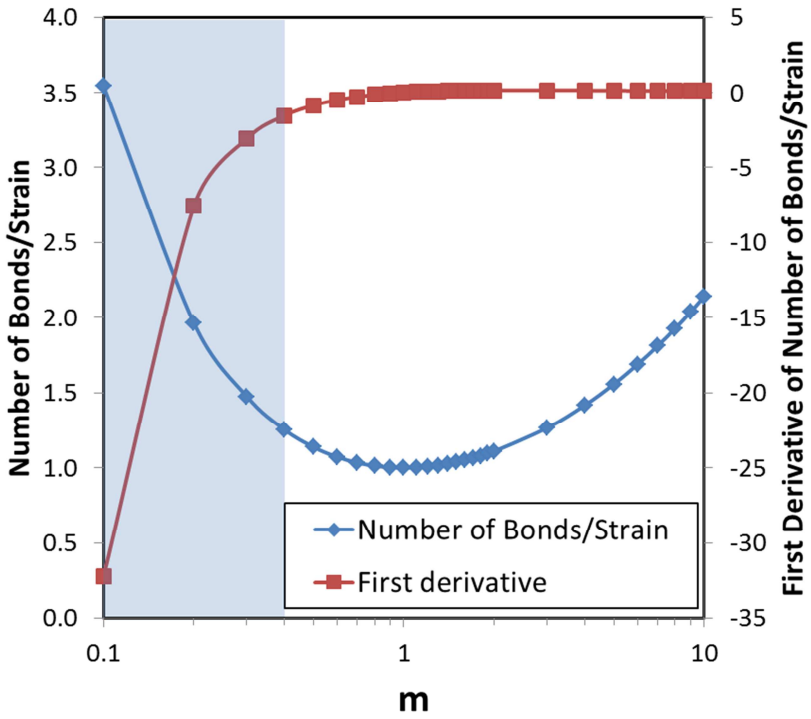

Figure 4.12. The number of new A-B bonds per unit strain and its first derivative as a function of m plotted from Eq. 4-3 for a orthorhombic precipitate in a orthorhombic grain.

The possible effect of such distortions was also estimated by KMC simulations assuming that the precipitates were dense, oblate ellipsoids. If, for example, the ratio of the semi-major to semi-minor axes were two, it was estimated using KMC simulations that this would affect the dissolution rate by a factor 30-40% [24].

While all of the above factors are not strong their sum could reasonably explain the factor of two difference between the experimental findings and the Eq. 4-1.

4.7. COMPARISON TO OTHER REPORTED RESULTS

Sun et al. [25] reported a critical strain of 592, using HPT, to mix millimeter size Cu and Ag samples corresponding to a composition of $Cu_{59}Ag_{41}$ by atomic percent. This is in contrast to the results reported in this thesis. In the reference study, the samples were deformed by constrained geometry in which the deformation is possibly localized near the surface. So, the actual strain experienced by the sample near the surface could be multiple times of the reported value of 592. In this thesis, the shear induced mixing was studied with four different initial length scales and HPT processed samples showed homogeneous deformation through thickness. In another recent study, Mohsen et al. [26] reported a shear strain of ≈350 to completely homogenize an $Ag_{60}Cu_{40}$ eutectic alloy with an initial lamellar structure having a wavelength of ≈ 165 nm. However, an initially 1.0 mm thick sample was used in the un-constrained configuration which reduced to 0.1 mm within the first cycle and reducing the lamellar structure at the center of the disk to ≈30 nm wavelength. The experimental strain to mix matched well with the simulated strain to mix using KMC simulations considering an initial length scale of ≈30 nm. The critical

strain to mix in these KMC simulations scaled linearly with the wavelength of the layered lamellar structure with a proportionality constant of ≈13 nm^{-1} for $Ag_{70}Cu_{30}$ alloy. The geometrical model described in Eq. 4-1 for spherical precipitates of radius $R_{p,i}$ gives a proportionality constant of 17 nm^{-1} for similar alloy. This thesis studied shear mixing for four different initial length scales and experimentally verified the superdiffusive nature of mixing.

4.8. STRAIN PATHS DURING MIXING OF PARTICLES

Another unanswered question related to shear induced mixing behavior in a model immiscible system such as Cu-Ag system is the strain path it follows during evolution from a phase separated to a fully mixed state. For example, simple shear strain will elongate the particle in the direction of the shear but the occurrence and nature of instabilities during particle elongation, the degree of co-deformation, and the role of grain boundaries and triple lines are not well understood. Layered structures have been observed in sliding wear tests [27]. Cu-Ag sample with the largest initial particle size ($R_{p,i}$ of 131 nm) was deformed at room temperature with strain ranging from an factor of 1 to few hundred. Continuous HPT deformation mode was used so that the complexity arising from strain reversal in a back and forth cycle are avoided.

Figure 4.13 shows the Ag morphology at low strains imaged in the RD direction (TD-ND plane). The shear direction is as shown in the images. The shape of Ag at $\varepsilon = 1.5$ is representative of predominantly simple shear deformation and it agrees with the strain of 1.8 calculated from the shape of the Ag. Also, the aspect ratios should be simply

proportional to the level of strain and they agree well within a factor of 2. At strains of 1.5, 2.5, and 6 the aspect ratios of particles are ~3, ~4.5, and ~10, respectively. With increasing strain the particles elongate further along the direction of the shear as expected. It is not well understood if there are any instabilities during particle elongation i.e. if they break up at some point and what is the level of mixing during these initial stages.

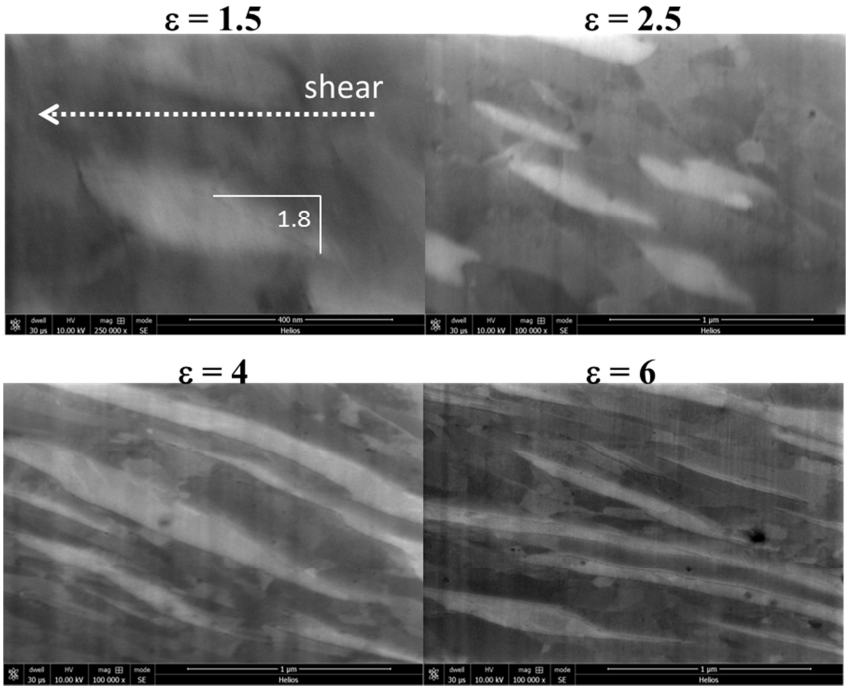

Figure 4.13. SEM images taken in the TD-ND plane (looking into RD) of the sample with $R_{p,i}$ of 131 nm deformed for very low strains.

A better understanding can be obtained by imaging the particles in at least 2 directions to study morphological evolution. Figure 4.14 and Figure 4.15 shows the SEM images at varying strains in two directions (RD-TD plane and TD-ND plane). At ε = 7 the particles are compact and equiaxed in the RD-TD plane but show elongation in the TD-ND plane. It should be noted that the particle axis in the TD-ND plane is not aligned

with the shear direction. This is expected for simple shear deformations. Thus, the RD-TD plane is imaging sections which are cutting through the particles. In this sense, the RD-TD planes do not represent the shape of the actual particles. At $\varepsilon = 11$ and above the particle shape doesn't remain compact in RD-TD plane. The interface structure becomes irregular and distorted possibly due to roughening of the Cu-Ag interface. This establishes that multiple slip systems are active. The TD-ND planes show continuous thinning and elongation of the particles until at $\varepsilon = 60$ they appear broken into smaller fragments. Figure 4.16(a) shows the mean particle length estimated from the TD-ND plane along the shear direction. Also shown is the particle length assuming simple shear deformation. The instability occurs in the strain range of 20 – 60 when Ag of mean length ~3500 nm breaks down to ~650 nm long fragments. For a 262 nm initial Ag diameter a strain of 20 by simple shear would result in a ~5200 nm long particle. Taking into account the uncertainty in the measurement from using SEM images the agreement between the actual mean particle length and the expected one within a factor of two is reasonable. Thus, this instability could very well be the very first instability during particle shearing. There could potentially be more instabilities at higher strains and it needs to be investigated further using advanced electron microscopy techniques.

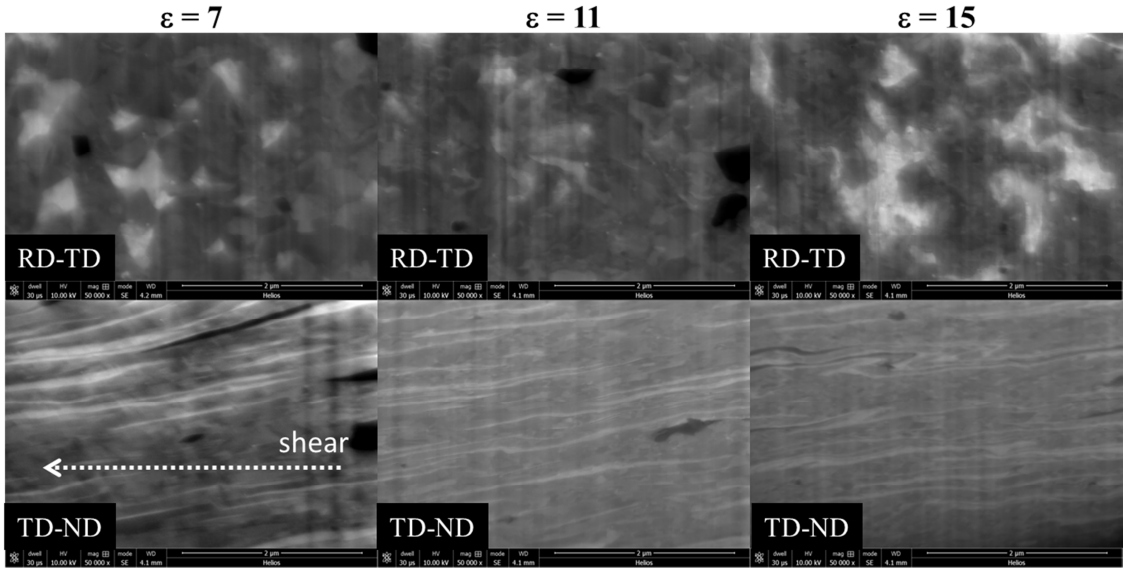

Figure 4.14. SEM images in RD-TD and TD-ND planes of the sample with Rp,i of 131 nm deformed by HPT for strains of 7, 11, and 15.

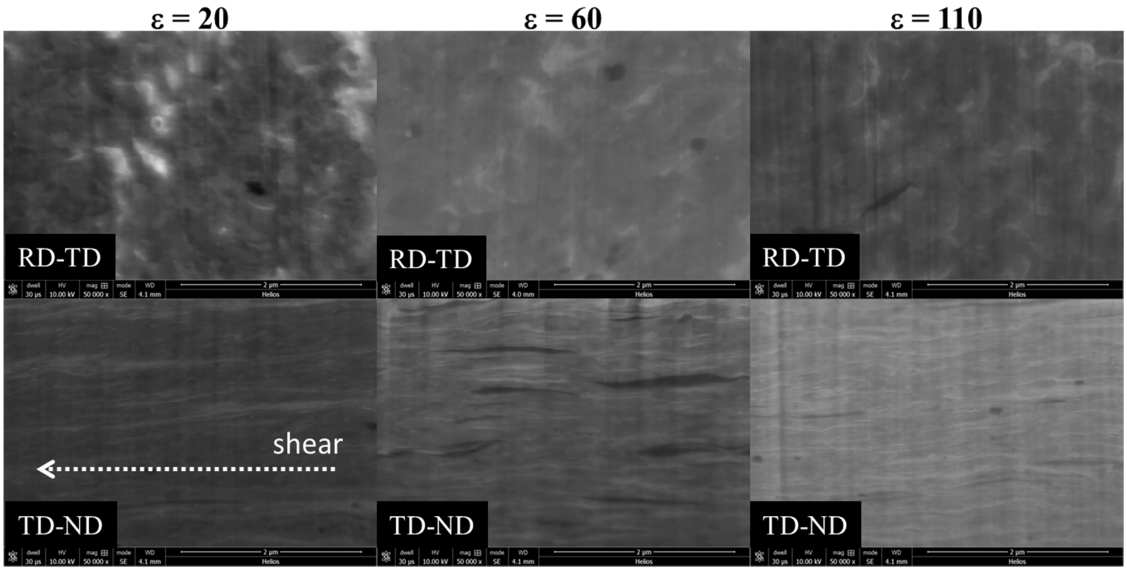

Figure 4.15. SEM images in RD-TD and TD-ND planes of the sample with Rp,i of 131 nm deformed by HPT for strains of 20, 60, and 110.

The thinning of the Cu and Ag grains with strain was investigated by XRD by tracking the crystallite sizes, which represent the thicknesses of these layers. This is shown in Figure 4.16(b). Both Cu and Ag thicknesses decrease within the strain range investigated. Interestingly, the solubility (~0.8 %) is constant during the thinning and break up of these layers. This suggests the limited intermixing during the inhomogeneous codeformation of the Cu and Ag. The shapes in the RD-TD plane become distorted and decrease in size with increasing strain. MD simulation of Cu-Ag [12] showed that a spherical precipitate first becomes distorted at $\varepsilon = 6$ with little intermixing similar to planar interfaces, but at $\varepsilon = 60$ they eventually mix and the system homogenizes. Similarly, in KMC simulations [9] of a binary A-B alloy subjected to shearing at 400 K it was shown that at low shearing rates the initial sharp interface becomes unstable and develops undulations (roughness) with mutual solubility increasing only by ~ 0.1 %. In this case, new Cu-Ag bonds would mostly be associated with creation of new interface area at low strains rather than intermixing. The rate of creation of new A-B bonds during homogeneous co-deformation will scale with the same exponent as shear mixing. These results suggest that co-deformation should indeed affect the microstructural evolution during HPT and influence the rate of shear mixing as described in section 4.5.a. However, it should be noted that the difference in HPT processing, continuous versus, back and forth, will influence the details of the analysis.

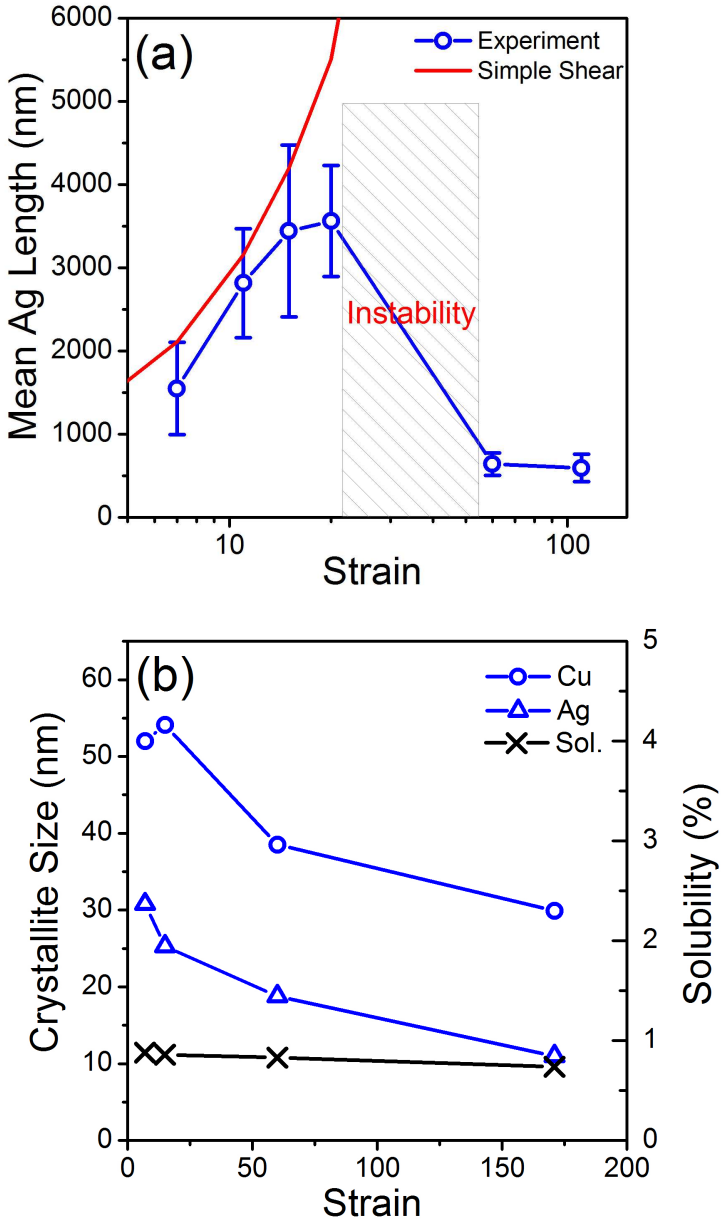

Figure 4.16. (a) Mean particle length along the shear direction estimated from the SEM images. (b) Cu size, Ag size, and solubility (estimated from XRD) for the sample with $R_{p,i}$ of 131 nm deformed by HPT. These measurements were taken while probing primarily in the normal direction of the sample.

4.9. CONCLUSIONS

It was already known that SPD results in mechanical alloying and can be used to process far from equilibrium materials. How atoms intermix during SPD is poorly understood and part of this is due to the lack of quantitative measurements on the dependence of shear induced mixing on strain and on the length scale of heterogeneities. The results presented in this chapter experimentally support the prediction of a 'superdiffusive' model for shear induced mixing in Cu-Ag system, where the dissolution rate of particles is controlled by the rate of dislocation glide across interfaces. Superdiffusive means the mixing efficiency increases with the pair separation distance. This behavior was predicted previously by MD simulations only and no experimental study existed to verify the dependence of shear induced mixing on varying initial length scales which was needed to confirm the nature of mixing. Another interesting system, found in MD simulation, is the Cu-Fe system in which dislocations initially accumulate at the interface and rotates the particle into fcc coherent interface with Cu at strain ~ 10. Beyond this point the mixing is superdiffusive similar to Cu-Ag. A detailed investigation on Cu-Fe system using experiments similar to Cu-Ag system in this study would give further insight into such mechanisms.

The superdiffusive nature of mixing offers a direct rationalization of the self-organization in the system during shearing at elevated temperatures. The pair diffusion coefficient in superdiffusive mixing scales with the pair separation distance, however, the thermal diffusion is independent of pair separation distance. The competition between these two will be length scale dependent. At small length scales, thermal diffusion will be dominant and at large length scales shear mixing will be dominant. The competition

between the two mechanisms under appropriate conditions is expected to result in a steady state length scale. This will enable to tune the microstructures of the system and control the properties. High temperature ball milling (BM) experiments on Cu-Ag system has shown self-organization behavior but little is known about the processing conditions. Limited experimental effort has focused on quantifying the effect of strain rate and the interrelationship between strain rate and temperature, which hinders our ability to predictively engineer the process.

These results also provide a means to control the extent of solid solution desired in systems such as Cu-Ag. The grains are refined as well in SPD processing, thus, designing high strength alloys by refining the grain size and enhancing the solid solution strengthening effect in a controlled way is possible.

An unknown factor in BM experiments is the total strain and strain rate experienced by the powders. Using the present study we can roughly estimate the magnitude of these parameters. It is found in the present study that a 10 μm Cu and Ag powders require about 5 hours of BM to fully mix them. The results in this chapter have shown that the strain to mix scale with particle radius with a proportionality constant ~ 5.5. This would correspond to an average strain rate in BM of ~1.5 s^{-1}. This is just an estimate since BM corresponds more to a random mixing process, whereas, HPT is dominantly simple shear deformation. It should be noted that the strain rate in HPT experiments can be controlled by changing the rotation speed of the anvil. As will be shown in the next chapter, the strain rate can be controlled easily within 0.1 to 10 s^{-1} range. The estimated strain rate in BM lies in this range, thus, direct comparisons and calibration between BM and HPT experiments can be made.

A fully mixed Cu-Ag system can also be used to trace shear mixing in more complex systems such as ternary alloys. In fact, Wang et al. [28] recently showed that Cu can transfer from a fully mixed Cu-Ag phase into Ni phase by shearing but Ni and Ag do not intermix and Cu was enriched at the interphase boundaries. This study ruled out the possibility of strain localization preventing mixing and illustrated the importance of chemical effects in phase formation by SPD and helped to explain why some alloys with high positive heat of mixing do no mix.

4.10. REFERENCES

[1] C. Suryanarayama, Prog. Mater. Sci. 46 (2001) p.1.

[2] A. Yavari, P. Desré, T. Benameur, Phys. Rev. Let. 68 (1992) p.2235.

[3] E. Ma, M. Atzmon, Mat. Chem. and Phys. 39 (1995) p.249.

[4] T. Klassen, U. Herr, and R.S. Averback, Acta Mater. 45, 2921 (1997).

[5] C. Gente, M. Oehring and R. Bormann, Phys. Rev. B 48 (1993) p.13244.

[6] C.C. Koch and J.D. Whittenberge, Intermetallics 4, 339-355 (1996).

[7] F. Delogu, M. Pintore, S. Enzo, F. Cardellini, V. Contini, A. Montone, V. Rosato, Philosophical Magazine 76 (1997) 651-662.

[8] P. Bellon, R. Averback, Physical Review Letters 74 (1995) 1819-1822.

[9] P. Bellon and R.S. Averback, Phys. Rev. Letters 74 (1995) p.1819.

[10] S. Odunuga, Y. Li, P. Krasnochtchekov, P. Bellon, R. Averback, Physical Review Letters 95 (2005) 93-96.

[11] D. Raabe, S. Ohsaki, and K. Hon, Acta Materialia 57 (2009) 5254–5263

[12] Y. Ashkenazy, N. Q. Vo, D. Schwen, R. S. Averback, and P. Bellon, Acta Mater. 60, 984 (2012).

[13] P. Bellon, R. S. Averback, S. Odunuga, Y. Li, and P. Krasnochtchekov, A. Caro, Phys. Rev. Lett. 99, 110602 (2007).

[14] P. Bellon, R. Averback, Physical Review Letters 74 (1995) 1819-1822.

[15] S. Odunuga, Y. Li, P. Krasnochtchekov, P. Bellon, and R. Averback, Physical Review Letters 95, 93-96 (2005).

[16] Y. Ashkenazy, N.Q. Vo, D. Schwen, R.S. Averback, and P. Bellon, Acta Materialia 60, 984–993 (2012).

[17] P. Bellon, R. Averback, S. Odunuga, Y. Li, P. Krasnochtchekov, and A. Caro, Physical Review Letters 99, 1-4 (2007).

[18] A.R. Denton, N.W. Ashcroft, Physical Review A **43** (1991) 3161-3164.

[19] R.K. Linde, Journal of Applied Physics **37** (1966) 934.

[20] A.L. Patterson, Phys. Rev. 56 (1939) 978–982.

[21] P. Bellon, R. Averback, S. Odunuga, Y. Li, P. Krasnochtchekov, and A. Caro, Physical Review Letters 99, 1-4 (2007).

[22] David N. Seidman, Annu. Rev. Mater. Res. 37, 127 (2007).

[23] L.S. Tóth, K.W. Neale, J.J. Jonas, Acta Metallurgica **37** (1989) 2197–2210.

[24] D. Schwen, private communication.

[25] Y.F. Sun, H. Fujii, T. Nakamura, N. Tsuji, D. Todaka, M. Umemoto, Scr. Mater. 65 (2011) 489–492.

[26] M. Pouryazdan, D. Schwen, D. Wang, T. Scherer, H. Hahn, R.S. Averback, P. Bellon, Phys. Rev. B 86 (2012) 144302.

[27] F. Ren, S. N. Arshad, P. Bellon, R. S. Averback, M. Pouryazdan, H. Hahn (in preparation)

[28] M. Wang, Acta Mater. 66 (2014), 1–11.

CHAPTER 5

SELF-ORGANIZATION IN COPPER-SILVER

5.1. INTRODUCTION

Nanostructured alloys have been widely studied in recent decades owing to their potential to exhibit remarkable properties relative to their traditional engineering alloy counterparts. Nanostructuring is particularly attractive for developing new high-strength alloys, which are inherently strong due to the high density of grain boundaries and interfaces [1,2,3,4,5]. The relative simplicity of single phase materials make them ideal for investigation of basic mechanisms associated with processing and performance. Interfaces in multiphase alloys can be tailored with greater flexibility to obtain specific properties [6] and the inclusion of multiple components provides the opportunity to engineer additional functionality, such as corrosion resistance [7] or thermal stability [8]. Nanostructured multiphase thin film alloys have also been investigated in a number of model systems, typically produced by physical vapor deposition or electrochemical deposition. Nanostructure design in bulk multiphase materials has been slower to develop and their processing remains a challenge. Severe plastic deformation (SPD) has attracted practical interest as it offers a simple yet efficient means to synthesize nanostructured alloys with highly non-equilibrium microstructural and chemical constituents [9,10,11]. The most popular approach to SPD, high-energy ball milling,

[12,13,14] has been used to process a variety of nanostructured powders that can be sintered into bulk alloys [15]. Ball milling easily accesses high strains and strain rates and is simple and inexpensive. However, critical information about total strain and strain rate cannot be quantified during these experiments. Some alternative approaches, such as equal channel angular compression or accumulative roll bonding, typically have difficulty achieving the high levels of strain characteristic of ball milling [16,17]. The majority of SPD studies have investigated materials response near room temperature. While the effects of temperature on nanostructural evolution have been investigated in a number of studies [18,19,20,21], limited experimental effort has been devoted to characterizing strain rate effects during SPD [22]. Precise knowledge and understanding of the process parameters, temperature and strain rate, are important for both fundamental studies and process engineering.

SPD typically involves two key processes; forced chemical mixing and thermodynamically driven relaxations [23,24,25]. Forced chemical mixing refers to the athermal relocation of atoms down composition gradients induced by sustained shear deformation [26,27,28,29]. At fixed temperature and strain rate, compositional inhomogeneities resulting from the thermodynamically driven relaxations will occur over characteristic spatial wavelengths associated with the diffusivity and relaxation time. The process of self-organization into compositionally patterned nanostructures occurs in immiscible systems where the two mechanisms of shearing and thermal diffusion of vacancies act in competition. Shearing tends to homogenize the alloy, while thermally activated diffusion tends to decompose it. The effect of these two competing mechanisms on the final microstructure was studied by Monte Carlo simulations [25] in a FCC $A_{50}B_{50}$

alloy by changing the shearing rates at 400 K. It was shown that at intermediate strain rates the system exhibits nanoscale compositional patterning at a length scale that may be controlled by varying the strain rate and temperature. Such a scheme could provide a route to tune the microstructures of engineering materials at nanometer length scales in systems processed far from equilibrium. However, limited experimental effort has focused on quantifying the effect of strain rate and the interrelationship between strain rate and temperature, which hinders our ability to predictively engineer the process.

Shear-induced mixing can be quantified by characterizing the mean square relative displacement (MSRD) between pairs of atoms [30,31], which describes the relocation of atoms in terms of their relative coordinates. Molecular dynamics simulations suggests that shear-induced mixing in immiscible systems such as Cu-Ag is superdiffusive in nature [41,46,32,33], because the relative pair diffusion coefficient, defined as the change of MSRD with time, during shearing is a linear function of the pair separation. This was experimentally verified in a previous investigation [34] of shear-induced mixing in nanocrystalline Cu-Ag alloys and was presented in Chapter 4. The superdiffusive nature of shear induced mixing helps explain self-organization during sustained shearing at elevated temperatures. The thermal pair diffusion coefficient is independent of pair separation since the movement of atoms is uncorrelated. We hypothesize that the characteristic steady state length scale for self-organization will occur at the length scale where the competing pair diffusion coefficients are approximately equal [35]. At small length scales, the thermally activated diffusion coefficient dominates and phase separation occurs. At larger length scales shear-induced mixing dominates and the system randomizes. At low temperatures the length scale will

approach that of a single atom and the system will tend to homogenize, and at high temperatures thermal diffusivity will dominate and the system will approach a state characteristic of pure thermal annealing. Increasing the strain rate should enhance shear mixing and tend to randomize the microstructure.

The predictions of characteristic patterning length scales based on the simple hypothesis described above were, more recently, tested by the rigid lattice KMC simulations (similar to [25]) of a crystal under shear in presence of thermal diffusion [54]. The shear induced pair diffusion coefficient was equated with the thermally activated pair diffusion coefficient to yield the steady state length scale, r, as:

$$r = \frac{a_o}{d^2}\frac{F_{vac}}{F_{shear}} \quad (1)$$

where F_{vac} is the frequency of vacancy jumps, F_{shear} is the frequency at which dislocations are inserted in the simulation cell, a_o is the nearest neighbor distance and d is the number of atomic planes. The effects of temperature and strain rate on steady-state self-organization still lack experimental validation and quantification. The simple arguments derived from computational studies are complicated by the fact that shearing produces vacancies [36,37] that have not been accounted for in any model of the process. The relative effect of excess vacancies is quite sensitive to temperature and interface density which makes accounting for them challenging. The models also do not account for important factors such as interfaces, grain boundary diffusion, crystallographic texture, recovery, or recrystallization, which could play an important role in microstructural development in real materials.

Experimental evidence of self-organization during high energy ball milling at elevated temperatures exists in studies by X-ray diffraction & differential scanning calorimetry [38], transmission electron microscopy [39], atom probe field ion microscopy [40], and atom probe tomography [41,42]. Ball milling experiments and x-ray diffraction (XRD) on $Cu_{50}Ag_{50}$ [18] indicated that various steady state microstructures can be stabilized between a homogeneous FCC alloy at room temperature and a fully decomposed two-phase mixture at 473K. The apparent activation energy for milling induced decomposition was 0.114 ± 0.004 eV which is much smaller than for vacancy migration in either Ag (0.66 eV) or Cu (0.80 eV). The result suggests that self-organization should not simply be the sum of the independent processes of shearing and thermal decomposition by equilibrium vacancies, assuming that the average shear rate associated with ball milling is temperature independent. Shorter decomposition times during milling suggest that diffusion is enhanced by milling [18]. This is attributed to the excess concentration of vacancies created by shearing [55,56] and it was concluded that the decomposition reaction occurring during milling displays a weak temperature dependence. Related atom probe tomography analysis of ball milled powders of $Cu_{50}Ag_{50}$ showed that the compositional patterns exhibited length scales of about 1 nm, 3-5 nm, and 5-10 nm at milling temperatures of 120, 150, and 180 °C, respectively [41].

The use of ball milling as a route to SPD presents a major challenge in that the strain rate and total strain are not well defined. This limits the ability to quantitatively interpret the results in the context of known materials properties such as vacancy diffusivity and shear-induced mixing rate, and hinders the validation of an appropriate model. This work utilizes high pressure torsion (HPT) [43,44,45] as a means to study the

effects of temperature on self-organization in Cu-Ag system under controlled strain and strain rate. The associated results will allow us to validate or refine the models for self-organization during high temperature SPD.

Homogenized powders of $Cu_{90}Ag_{10}$ were fabricated by high energy ball milling micron-sized elemental Cu and Ag powders which were hot pressed at 300 °C in vacuum (2×10^{-6} Pa) under 1 GPa pressure, in a press attached to the glovebox. This resulted in >98% dense Cu samples containing Ag precipitates with volume averaged initial diameter, $D_{p,i}$ of 31 +/- 7 nm. Annealing the as-pressed samples at 600 and 750 °C for 1 hour in Ar produced samples with $D_{p,i}$ of 122 +/- 25 nm and 252 +/- 58 nm, respectively. The associated error bars are one standard deviation of the particle diameter distributions measured from over 200 particles imaged by high-angle annular dark field scanning transmission electron microscopy (HAADF-STEM). The particle size distributions of as-prepared samples display characteristic log-normal distribution [34]. Preheating the anvils, whose thermal mass far exceeds the samples, to the appropriate temperature controlled the processing temperature. HPT was performed quickly after inserting the samples, which were also quenched rapidly at the end of the cycle. Samples were thermally annealed at the same temperature for the same times as the HPT experiments for comparison. High temperature ball milling was also performed at 125, 200, 300 and 400 °C using fully mixed $Cu_{90}Ag_{10}$ powders, 600 °C annealed powders, and micron-sized powders as the starting material. A thermal band heater around the ball milling vial and a control thermocouple was attached to the outer surface.

The sample reference frame is described relative to the surface normal (ND for normal direction, RD for radial direction, and TD for transverse or shear directions) as shown in [34]. HAADF STEM (JEOL 2200FS) and atom probe tomography (APT, Cameca LEAP 4000X Si) were performed on samples prepared by focused ion beam (FIB, FEI company) milling. X-ray diffraction (PANalytical/Philips X'pert MRD system) was performed in the ND direction on the RD-TD plane using a 1 mm x 1 mm beam. The anisometric shapes of Cu grains and Ag particles in the HPT processed samples require measurements in both in-plane and perpendicular directions. The in-plane Ag particle diameters were determined in RD-TD plane from HAADF-STEM images by measuring over 200 particles and Cu grain diameters were determined by linear intercept method [46] performed on bright-field STEM images. The crystallite sizes in the perpendicular direction were estimated from XRD by peak fitting and using Scherrer's equation [47]. Both Ag and Cu sizes reported in this study are average sphere-equivalent diameters using $D_p=\sqrt[3]{(D_{TEM}^2)\cdot D_{XRD}}$. Additional HAADF-STEM images were taken in TD-ND planes, or RD direction, for selected samples to investigate the 3D shapes of the Ag precipitates. The particle and grain thicknesses measured by HAADF-STEM were consistent with XRD crystallite size, supporting the validity of the approach used to calculate the average diameters. This analysis was also applied to ball milled powders, which were composed primarily of millimeter scale disk-shaped particles. Note that in subsequent discussion, particle and grain diameter measured as described above will be distinguished from crystallite diameter, measured solely from XRD performed primarily through thickness, ND.

5.2. EVOLUTION TO STEADY STATE

Figure 5.1 shows the effect of total strain at 200 and 300 ^{o}C on the Ag and Cu crystallite sizes, and solubility for the sample with $D_{p,i}$ of 122 nm deformed at 1 rpm. The samples exhibit steady-state Ag diameter well below a strain of 1500, which is utilized for all subsequent data. The Cu grain size reaches steady state at higher strains than Ag, but still well below 1500. The solubility saturates to a steady state value at roughly the same strain as the Cu approaches a steady state size.

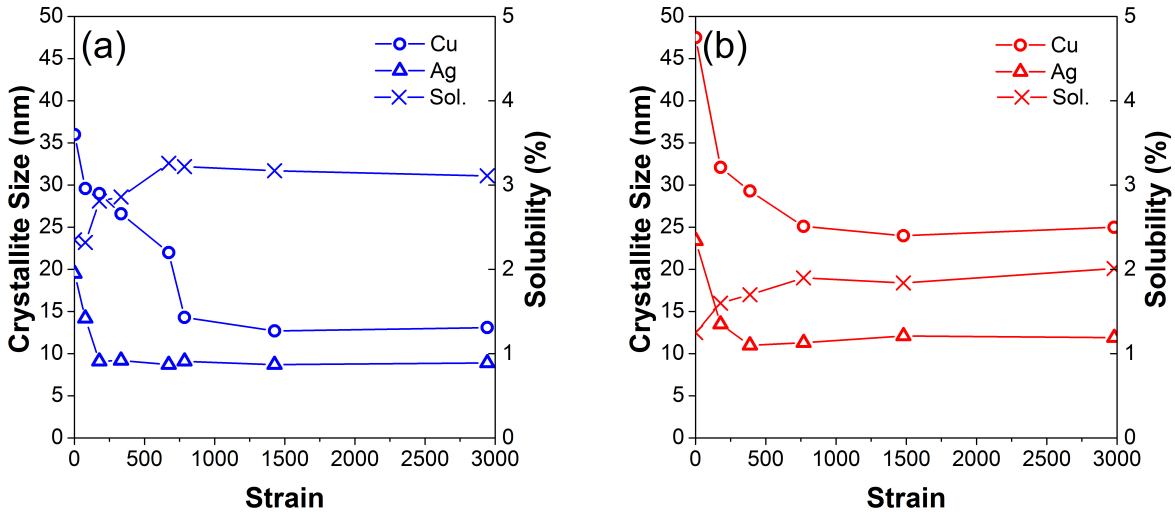

Figure 5.1 Evolution of the Cu grain diameter, Ag particle diameter, and solubility with strain at (a) 200 ^{o}C and (b) 300 ^{o}C for the sample with $D_{p,i}$ of 122 nm deformed at 1 rpm. All data estimated from XRD.

5.3. TEMPERATURE AND STRAIN RATE EFFECTS

Figure 5.2 shows the effect of temperature on the microstructures of samples with $D_{p,i}$ of 31 and 122 nm subjected to HPT at low (0.1 s^{-1}) and high (6.25 s^{-1}) strain rates. Reducing the temperature results in enhanced mixing, smaller Ag particles, and Ag

particles with interfaces that appear more chemically diffuse. These samples are all imaged in the ND direction (RD-TD plane).

5.4. STEADY STATE CU & AG SIZES AND SOLUBILITY

Figure 5.3 compares the Ag and Cu diameters, and Ag solubility for all the samples studied. There is negligible strain rate dependence to both the particle and grain sizes, within the experimental error. With the exception of the samples processed at 125 ^{o}C, there is also negligible strain rate dependence to solubility. As a comparison, samples were also ball milled at high temperatures and the diameters are reasonably consistent with those processed by HPT. The particle and grain diameters are approximately the same. The solubility of Ag in the ball milled samples is slightly higher than that of the HPT samples at low temperatures. It should be noted that due to difficulties calibrating the local temperature within the ball milling vial, the actual temperatures of the HPT and ball milled samples might differ slightly.

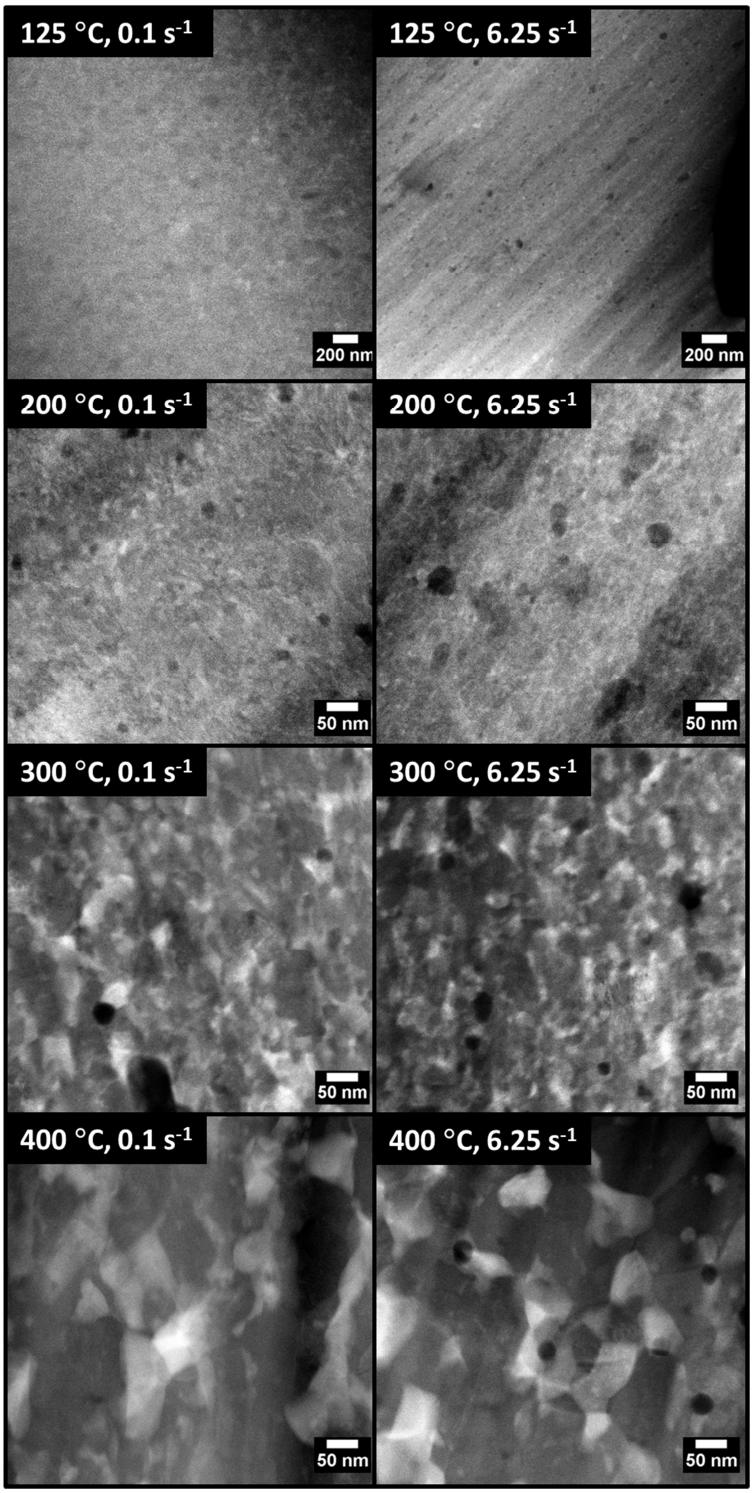

Figure 5.2: HAADF-STEM images of the sample with $D_{p,i}$ of 122 nm after HPT at 125, 200, and 300 °C and the sample with $D_{p,i}$ of 31 nm after HPT at 400 °C at low and high strain rates shown. All images are taken in the ND direction (RD-TD plane).

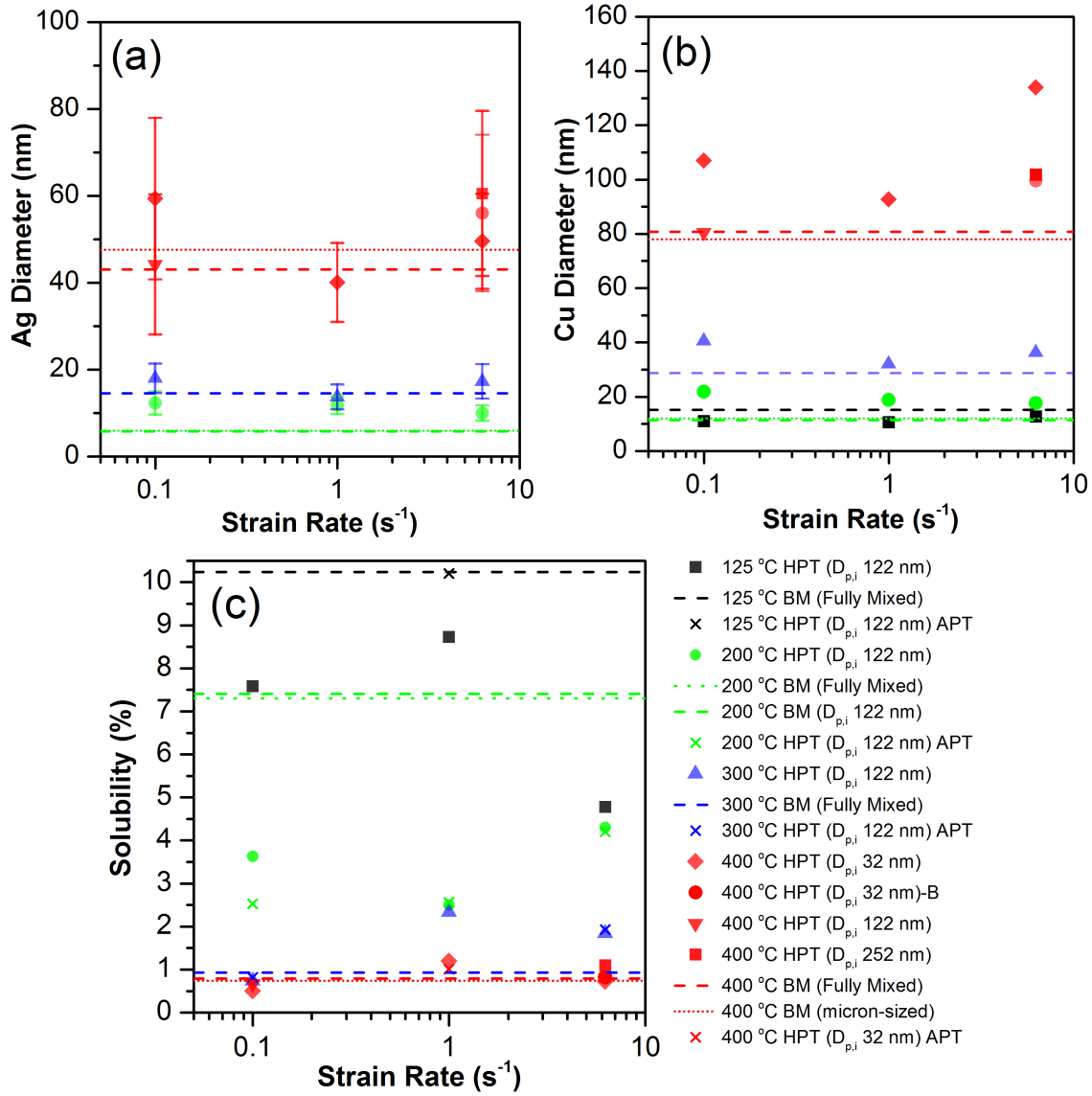

Figure 5.3: (a) Ag and (b) Cu diameters calculated from the in plane STEM images and corrected for thickness by XRD measurement, and (c) Solubility of Ag in Cu (all data determined from Cu(111) peak shift in XRD except the 'x' labels which is from APT). The dashed lines correspond to data taken from high temperature ball milling experiments. The legend applies to all three plots (a-c).

Selected APT data was acquired to confirm the Ag solubility measurements determined from XRD and generally characterize the Ag distribution in different types of samples. Figure 5.4(a) contains the reconstructed images of the APT tips where the color scale is based on the average Ag concentration in 1 nm^3 voxels. The figure also plots a histogram of Ag in all of the 1 nm^3 voxels. At room temperature, the sample with $D_{p,i}$=122 nm is completely randomized at strains exceeding 500 [34]. The quoted solubility values are measured as the mean Ag concentration in cuboidal regions sampled in the matrix region only. Figure 5.4(b) shows the distribution of Ag in such regions. At 125 ^oC, the solubility is 10.2 % at 1 s^{-1}. No distinct Ag-rich particles are present, but the distribution is not completely random. At 200 ^oC, Ag particles are clearly observed, and have relatively diffuse interfaces when compared to the samples prepared at 300 ^oC. The solubility of Ag in Cu at 200 °C is 2.53, 2.56, and 4.2 % at strain rates of 0.1, 1, and 6.25 s^{-1}, respectively. These solubilities are consistent with what was calculated from XRD for 1 and 6.25 s^{-1}. At 300 ^oC the Ag solubility varies from 0.82 to 1.93 % for strain rates between 0.1 and 6.25 s^{-1}. At 400 ^oC, no particles were observed, because the average inter-particle distance exceeds the size of the APT tip, and the average solubility is 1.01 %. Interconnected planes of Ag rich material are observed within the 400 ^oC sample. This is presumed to indicate Ag segregation at the Cu grain boundaries. APT also revealed Fe and O contamination typically less than 0.1 and 1 atomic percent, respectively.

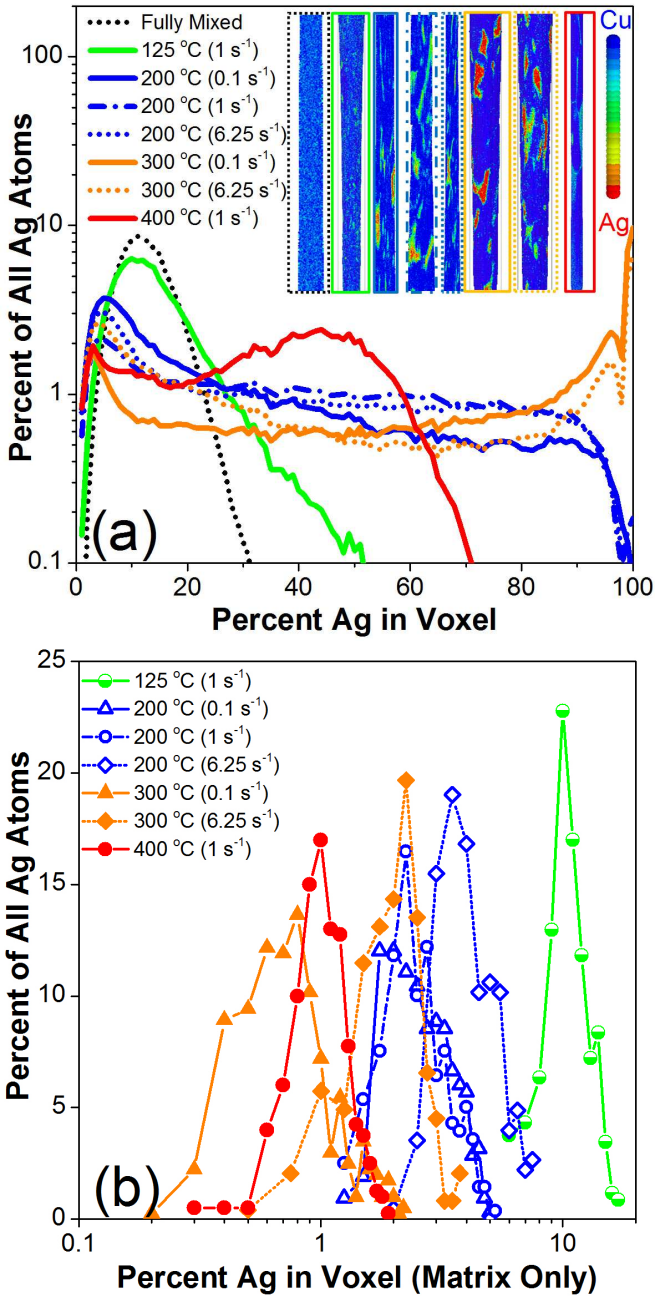

Figure 5.4: (a) Percent of All Ag atoms versus percent Ag in voxels for different temperatures and deformation rates. Inset show 1 nm^3 voxel based reconstruction of the tips corresponding to each plot. Data for fully mixed (random) sample is shown from previous study [34]. (b) Percent of All Ag atoms versus percent Ag in voxels located in the matrix region only (excluding Ag-rich particles). Approximately 10^5 atoms were sampled in each case.

5.5. TEXTURE ANALYSIS AT LOW AND HIGH STRAIN RATES

Figure 5.5 shows the inverse pole figures for Cu in the ND direction for the as-pressed sample and select samples processed by HPT at 125 and 400 °C. The as-pressed sample exhibits (001) and (111) texture in the ND direction with I_{max} of 2.09 MRD (multiples of a random distribution). The 400 °C HPT sample shows only a strong (111) texture with I_{max} of 4.01 and 3.94 MRD at 1 and 6.25 s^{-1} strain rates, respectively, suggesting a negligible strain rate effect on the texture. The Ag texture at 400 ^{o}C is similar to that of the Cu and also shows no significant strain rate dependence. The 125 °C HPT sample shows an even stronger (111) texture with I_{max} of 5.30 MRD at 1 s^{-1} strain rate. However, there is a slight decrease in (111) intensity to I_{max} of 4.23 MRD at 6.25 s^{-1} strain rate at 125 °C. No Ag peak was present in XRD scans at 125 ^{o}C.

5.6. SHEAR INDUCED COARSENING VERSUS THERMAL ANNEALING

Figure 5.6 compares shearing by HPT and thermal annealing of samples processed for equivalent times from the same initial condition ($D_{p,i}$ of 31 nm) at 400 ^{o}C. The HPT samples were processed at different strain rates, such that the total strain was equivalent in each. Samples in Figure 5.6 are imaged in the normal direction (RD-TD plane). For short processing times (4 min) thermal annealing results in smaller Ag diameters (30 +/- 6 nm) as compared to HPT (50 +/- 11 nm). This difference is evident in the images in Figure 5.6(a&d). The coarsening at higher shearing rate was confirmed by repeating the experiment, which resulted in similar Ag diameters (57 +/- 18 nm). For intermediate processing times (25 min) the Ag particle diameters of the two samples is

comparable and longer processing times (250 min) the particle sizes in both sets of samples are comparable within experimental error. Thermal annealing results in coarsening while HPT for different times at equivalent total strain (i.e. varying the strain rate) results in more or less similar particle sizes. Thermal annealing follows cubic Ostwald ripening kinetics (Figure 5.6(h)) [48,49].

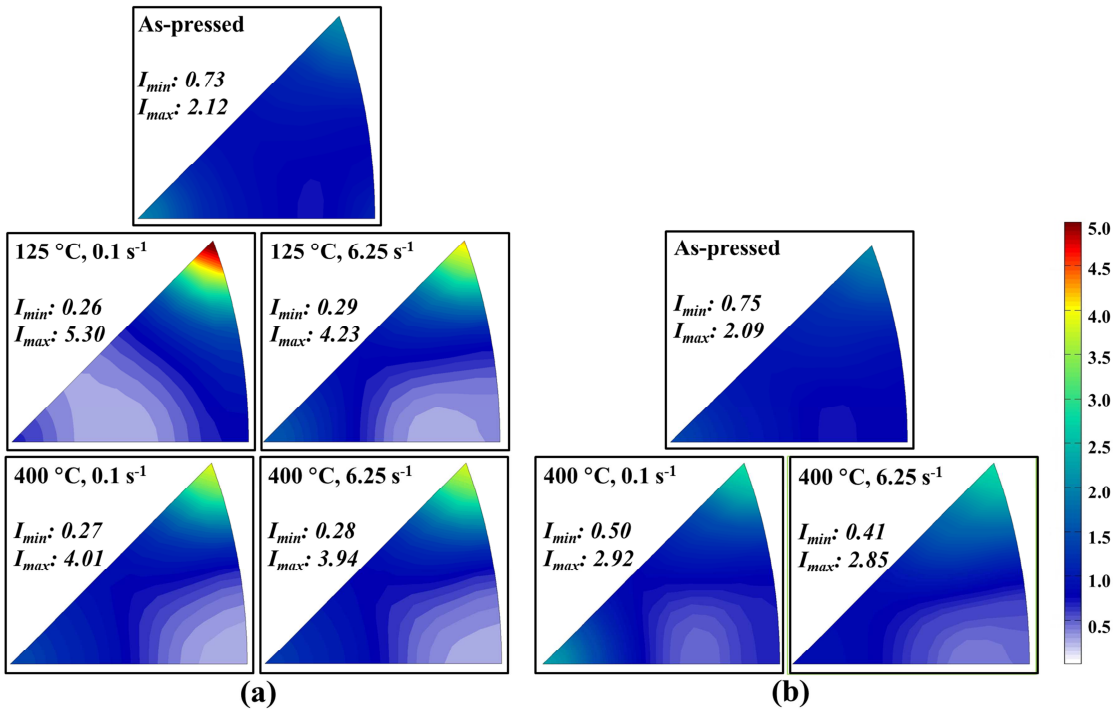

Figure 5.5: Inverse pole figures of Cu and Ag in the ND direction for the as-pressed, 125 °C HPT, and 400 °C HPT samples. The intensity scale is in the MRD units.

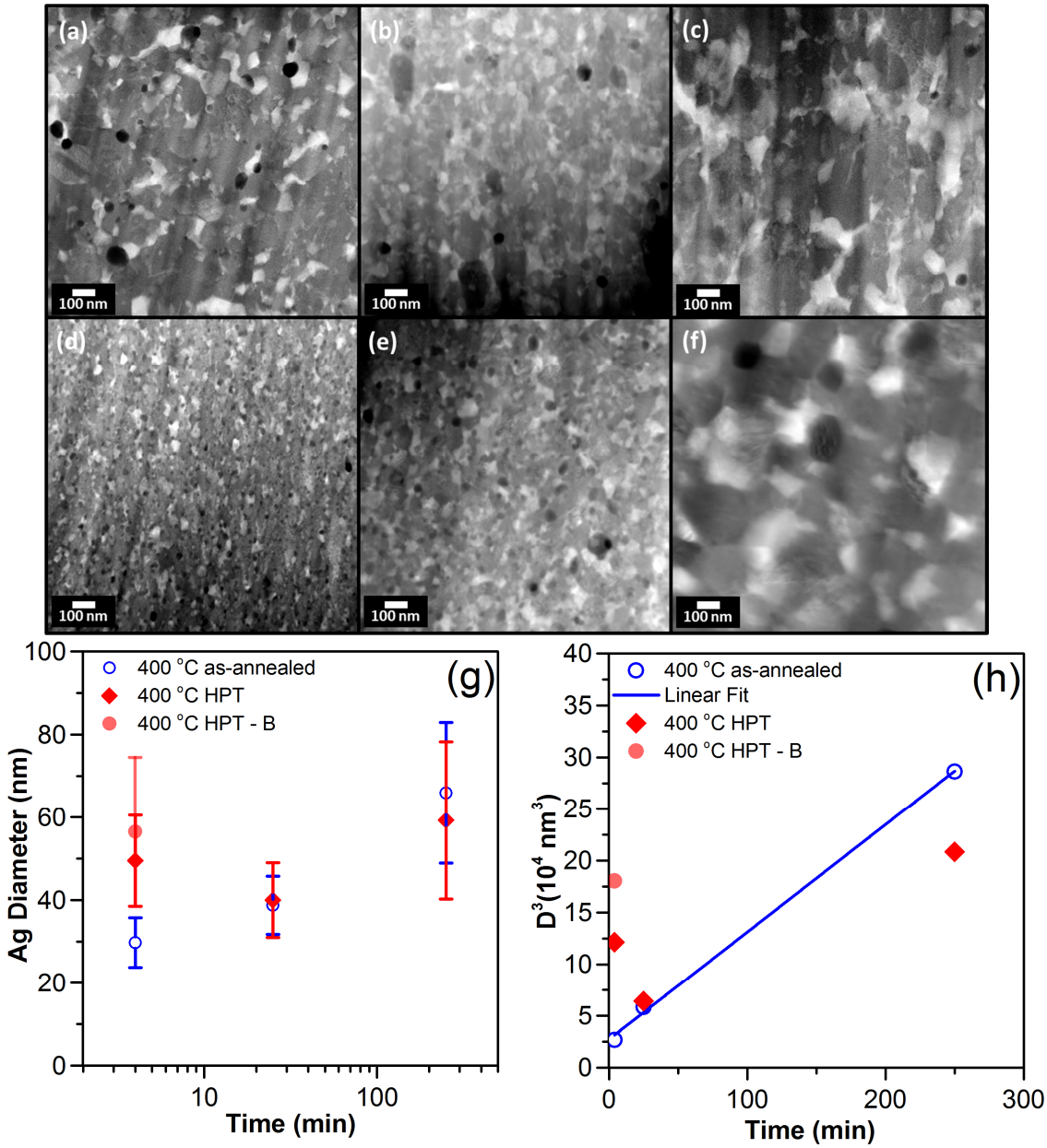

Figure 5.6: HAADF-STEM images of the sample with $D_{p,i}$=31 nm deformed at 400 °C by 25 cycles of HPT at (a) 6.25 s^{-1}, (b) 1 s^{-1}, and (c) 0.1 s^{-1}. The same sample when annealed at 400 °C for (d) 4 min, (e) 25 min, and (f) 250 min. The corresponding times in both experiments are equal and the images a – c are taken in RD-TD plane. (g) The Ag diameters calculated from the STEM Images for annealing and HPT at 400 °C. (h) Relationship between cubic of the average Ag diameter and time for 400 °C as-annealed and HPT sample. Note that directly comparing the Ag particle size from the images is not reasonable, because of their anisometric shape (see Figure 7).

5.7. 3-D GRAIN AND PARTICLE SHAPES

Cu grain and Ag particle shape depend on strain rate, as shown in Figure 5.7, for samples deformed at 400 °C. At the lowest strain rate, the Ag particles and Cu grains are most anisometric, on average exhibiting plate-like morphologies whose normal vectors align approximately with the sample normal. At the highest strain rate, the Ag and Cu grains are relatively equiaxed. At intermediate strain rate, the Ag and Cu grains shapes are intermediate to the shapes at higher and lower strain rates. The average ratio of Ag particle lengths parallel and perpendicular to the strain axis at 400 °C are 3.7, 2.1, and 1.4 at 0.1, 1, and 6.25 s^{-1}, respectively. This effect is also seen at 300 °C, as shown in Figure 5.8, but to a lesser extent; the average aspect ratio changes from 1.8 to 1.4 for strain rates between 0.1 and 6.25 s^{-1}.

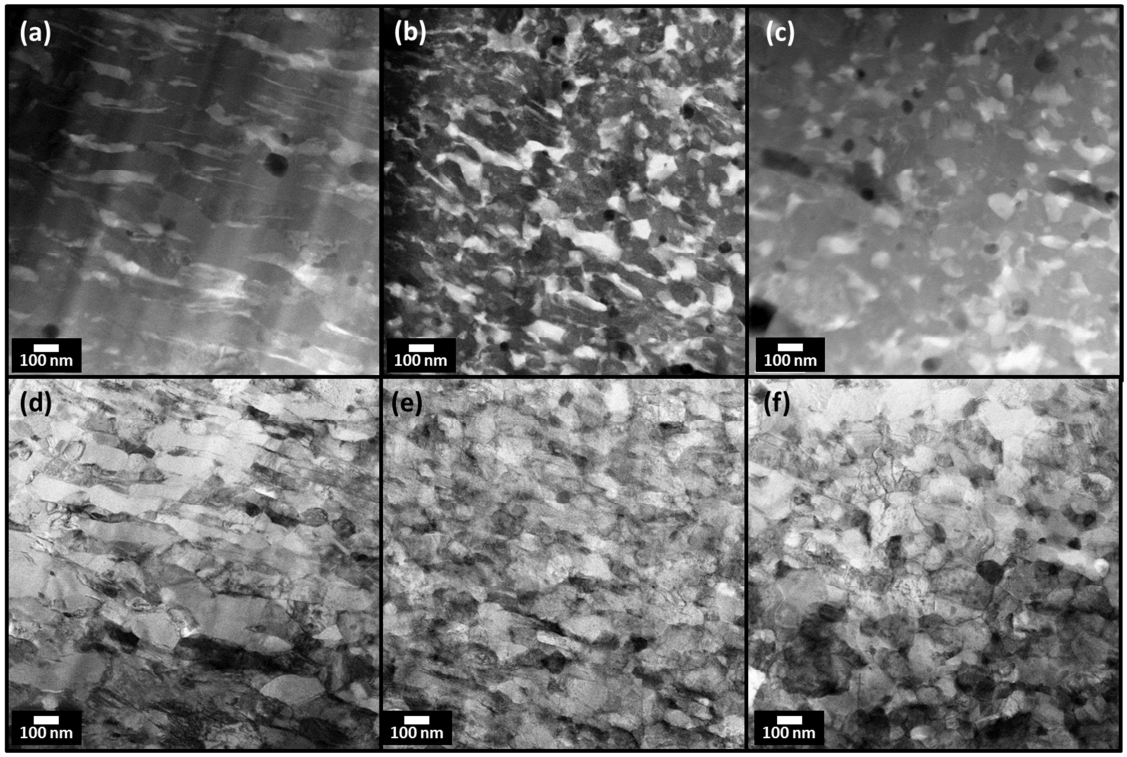

Figure 5.7: HAADF-STEM images in TD-ND plane of the sample with $D_{p,i}$ of 31 nm sample after 25 cycles of HPT at 400 °C deformed at (a) 0.1 s^{-1},(b) 1 s^{-1}, and (c) 6.25 s^{-1}, and their corresponding bright field STEM images (d, e, and f), respectively.

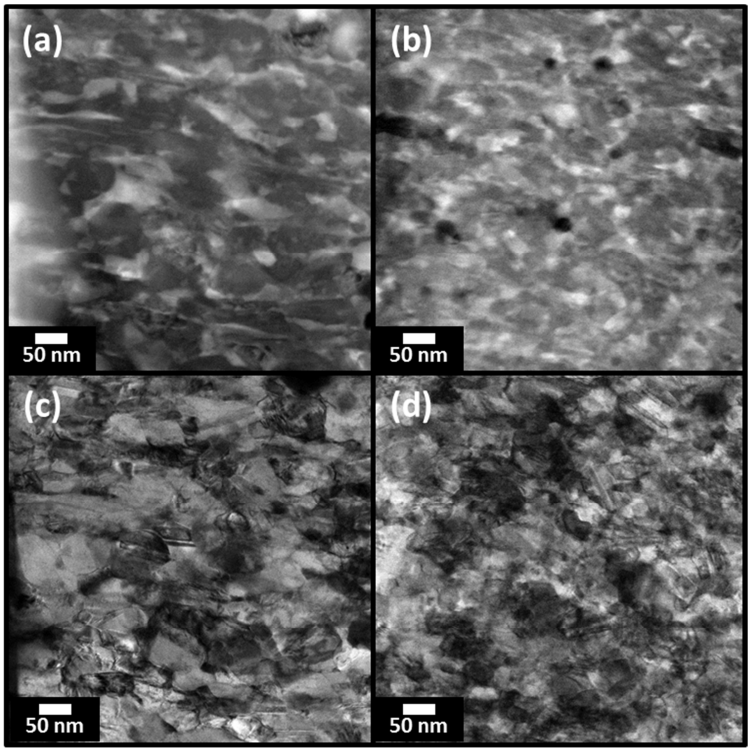

Figure 5.8: HAADF-STEM images in the TD-ND plane of the sample with $D_{p,i}$ of 122 nm sample after 25 cycles of HPT at 300 °C deformed at (a) 0.1 s^{-1} and (b) 6.25 s^{-1}, and their corresponding bright field STEM images (c and d), respectively.

5.8. STEADY STATE INDEPENDENT OF INITIAL CONDITION

Figure 5.9 depicts the steady state Ag particle diameters for samples with $D_{p,i}$ of 31 and 252 nm strained at 6.25 s^{-1} and 400 ^{o}C. The final Ag particle diameters are 65 +/- 19 nm and 75 +/- 20 nm, respectively. The final steady state values are approximately equivalent, within experimental error, and intermediate to the two initial conditions. The result demonstrates that the steady state microstructure is independent of the dominant evolution pathway; either coarsening or mixing. Ball milling of fully random solutions and decomposed microstructures performed at 200 ^{o}C, 300 ^{o}C, and 400 ^{o}C also results in the same steady-state microstructural length scales (see Figure 3).

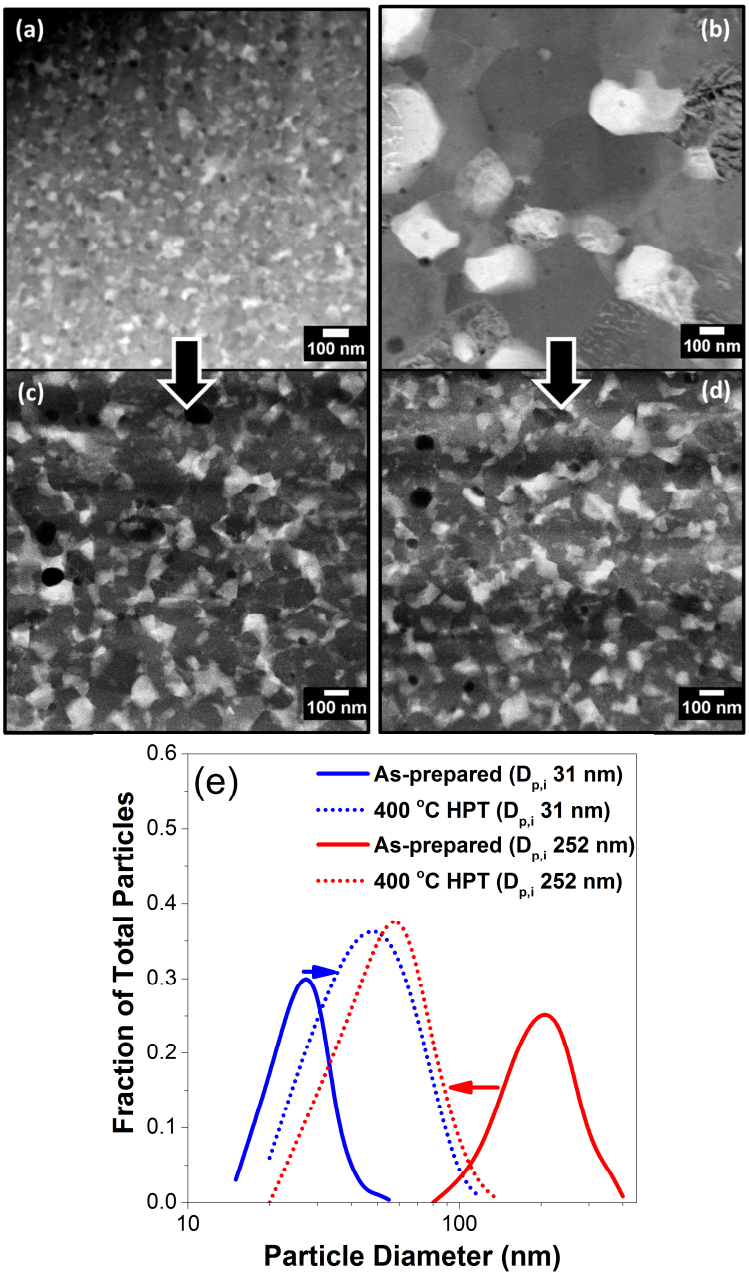

Figure 5.9: HAADF-STEM images of the sample with $D_{p,i}$ of 31 nm (a & c) and $D_{p,i}$ of 252 nm (b & d) before and after 25 cycles of HPT at 400 °C at 6.25 s^{-1} strain rate, respectively. The images c & d are taken in RD-TD plane. (e) Particle size distributions before and after HPT for the two samples.

5.9. DISCUSSION

Based on the results of prior simulation and experimental efforts, it is anticipated that the competition between shear induced mixing and thermally induced phase decomposition in binary alloys with a positive heat of mixing will evolve to a steady state after a critical amount of deformation [50,38,41]. The Ag and Cu crystallite sizes and non-equilibrium solubility reach steady state, shown in Figure 5.1, beyond which the values of these parameters do not vary. Sample with $D_{p,i}$ of 122 nm reach steady state at a strain of ~ 300 at 200 and 300 °C, respectively. The Cu grain diameters and solubility approaches a steady state concurrently at strains roughly 2 – 3 times greater than required for Ag. The entire system approaches steady state at the point when the Cu grain size and solubility reach steady state. Steady state should exist at a local minima in the energy landscape and it is not clear that it will be independent of the microstructural evolutionary pathway. However, the result in Figure 5.3 and Figure 5.9, demonstrate that steady state in Cu-Ag is independent of the initial particle size, either larger or smaller than the final value. In steady-state particles tend to homogenize at low temperatures < 125 ^{o}C and self-organize during decomposition at higher temperatures > 125 ^{o}C. Prior work observed ~1 nm clusters in $Cu_{50}Ag_{50}$ at 120 ^{o}C [41].

The Ag particle and Cu grain diameters for all the samples studied, shown in Figure 5.3, exhibit negligible strain rate dependence. The balanced steady state fluxes of Ag from precipitates into solution in Cu by shear mixing and Ag solute back into Ag particles through vacancy mediated diffusion must be approximately equivalent at each strain rate despite the variation in the rate of shear mixing. The rate of ballistic mixing under shearing scales approximately linearly with the strain rate [46], however, the

thermally activated diffusional flux must be approximately constant with strain rate. At 400 ^{o}C and 6,25 s^{-1}, shearing enhances the coarsening rate of the precipitates relative to the thermal annealing, as shown in Figure 5.6, where the average Ag diameter is almost twice as large as that of the annealed sample. This is despite the fact that the samples had been exposed to strain (~1500) large enough to fully mix the steady-state particle size more than 10 times over [34] if the thermal diffusion is absent. The lack of strain rate dependence in the characteristic steady-state length scale and the accelerated coarsening rate observed at 400 ^{o}C, both support the notion that strain at high strain rates enhances thermally activated transport. For a constant total strain, the amount of strain enhanced thermally activated transport is hypothesized to be approximately equivalent. KMC simulations [54] suggest that the critical factor affecting the microstructural length scale in steady state is the ratio of vacancy mediated atomic relocations to shear mediated atomic relocations. In the temperature range where recovery dominates, we hypothesize that non-equilibrium excess vacancies generated during shearing will primarily contribute thermally activated thermodynamic relaxations. Assuming that the total number of excess vacancies generated is independent of strain rate, for equivalent strain, the results may be rationalized on the basis of accounting for the total number of vacancy mediated atomic jumps and shear induced atomic jumps. Recrystallization in Cu alloys typically occurs at 200 – 300 ^{o}C [39,51,52]. Therefore, we anticipate that early stages of recrystallization might be active at ~ 200 °C with more significant recrystallization effect at 300 and 400 °C. The role of recrystallization will be discussed in more detail below.

Deformation results in enhanced self-diffusivity through pipe diffusion along the mobile dislocation cores as suggested by Cohen [53]. Cohen established an inequality

($T/T_m < 4.9/(2.2 - \log \dot{\varepsilon})$), which provides the minimum strain rate necessary to produce a dynamic diffusivity at least twice the static diffusivity. Nakajima [54] reported strain enhanced precipitate coarsening in magnesium alloy AZ80 which was explained in the context of dislocations scavenging solute and providing rapid short-circuit diffusional pathways. The present experiments are done at strain rates orders of magnitude greater than described in Cohen's criterion and Nakijama results, suggesting that pipe diffusion and scavenging effect alone cannot explain the enhanced transport observed here. KMC simulation [54] showed that shearing can also alter the vacancy jump rate. Vacancies can localize to trap sites and shearing at low rates can act to de-bind them. At high shearing rates ($>10^{-6}$ s^{-1}), the local environment changes faster than the fastest vacancy jump rate, and thus, vacancy jump rate becomes independent of the shearing rate [54]. Prior studies suggest that shearing can enhance thermally activated transport [55,56] and the rate of generation of excess vacancies is directly proportional to the shearing rate [55,56]. Our experimental strain rates exceed this strain rate by many orders of magnitude and thus we anticipate that this de-binding interaction may not be critical. The effect of shear enhanced diffusional transport has not been widely studied in the strain rate regime investigated in this work. The results lead us to hypothesize that the enhanced diffusional transport between 200 ^{o}C and 300 ^{o}C results primarily from an increase in the excess vacancy concentration with increasing strain rate. A phenomenological model for deformation induced vacancies was developed for Fe which showed that excess vacancy concentration can be several orders of magnitude higher than equilibrium concentration at strain rates > 10 s^{-1} [55] This effect also accounts for the low apparent activation

energy measured here and in prior studies [41], because the generation of non-equilibrium excess vacancies is relatively athermal.

At 400 ^{o}C, strain rate significantly impacts particle and grain shape, despite the fact that the average volumes of these features are approximately strain rate independent. Particles elongate in the direction of shear, adopting a plate-like morphology, with the largest aspect ratio grains and particles occurring at the lowest strain rate. The effect of particle shape is not expressed in the crystallographic texture, which suggests that the difference in shape does not result from a different deformation mode (e.g. grain boundary sliding versus crystal plasticity) [57]. Prior work demonstrates that recrystallization will be appreciable at this temperature [39] and recrystallization favors equiaxed grains in Cu alloys [58] and the frequency of recrystallization events should increase with increasing strain rate and mobile dislocation density [59], resulting in more equiaxed grains at higher strain rates. It is suggested that at high strain rates subgrain rotations assist recrystallization with limited thermal assistance [60]. Since the diffusivity of Ag far exceeds that of Cu [61], Cu will recrystallize at some critical temperature and level of stored energy, and Ag particles may reorganize via rapid diffusion to accommodate the Cu.

KMC simulations in [54] predict that the solubility can be completely tuned between equilibrium and complete solid solution by changing the strain rate at a given temperature in the compositional patterning regime. XRD and APT (Figure 5.3(c)) indicate that generally the solubility decreases with increasing temperature as expected based on reference [38]. However, the strain rate dependence is weak between 200 °C and 400 °C, with a general trend, especially in the APT data (Figure 5.4(b)), that the

solubility increases slightly with increasing strain rate. At 125 °C sample shows a significant drop in solubility from 1 to 6.25 s^{-1}. 125 ^{o}C is close to the regime where thermally activated vacancy jumps become active enough to affect microstructural evolution. At this temperature, thermally activated transport will be particularly sensitive to factors such as the excess vacancy concentration and sample self-heating during deformation. One discrepancy to note is the solubility of 200 °C ball milled powders which is almost twice that of 200 °C HPT samples. Klassen [38] showed for $Cu_{50}Ag_{50}$ ball milled powders that for temperatures below 200 °C, the two terminal solid solutions co-exist with an equiatomic solid solution. However, at 200 °C they fully phase separate. The actual temperature inside a vial could be lower than the measured temperature outside vial. The difference between the actual temperatures of the two experiments could explain this discrepancy. The KMC simulations do not account for the shear induced excess vacancies, which likely accounts for the differences observed between the experiments and computation. Another discrepancy is between solubility determined from APT and XRD for 125 °C at 1 s^{-1}. This can potentially be related to the atomic scale clustering that could be present at 125 °C, particularly in the grain boundaries. The Ag distribution (Figure 5.4) is not fully random which suggests the presence of such small clusters, which can also be noticed in the reconstruction. The scale of these clusters/particles in $Cu_{50}Ag_{50}$ system ball milled at 120 °C was 1 nm [41]. XRD will not account for these clusters, if they are present at the grain boundaries.

5.10. CONCLUSIONS

HPT experiments at high temperatures are employed to analyze the effects of temperature and strain rate on self-organization in dilute Cu-Ag. The competition between shear induced mixing and thermally induced phase separation led to the self-organization of the Cu-Ag system at length scales which varied from nearly fully mixed at 125 °C to 40 – 60 nm diameter Ag particles at 400 °C. The characteristic steady state length scale associated with compositional patterning is approximately independent of the shearing rate. The apparent activation energy is low (0.39 eV) between 200 and 400 °C. Moreover, shear-enhanced coarsening, relative to thermal annealing, was observed at 400 °C. The three observations all indicate that the excess non-equilibrium shear induced vacancy concentration dominates transport during in this temperature range. Steady state was reached via both mixing and coarsening mechanisms, which is quite practical from point of view of processing alloys regardless of their initial states. The shapes of Ag particles and Cu grains were strain rate dependent at 400 °C with highest deformation rate promoting rapid dynamic recrystallization at 400 °C.

5.11. REFERENCES

[1] Chokshi, A.H., A. Rosen, J. Karch, and H. Gleiter, Scripta Metallurgica, 1989. 23(10): p. 1679-1683.

[2] Schuh, C.A., T.G. Nieh, and H. Iwasaki, Acta Materialia, 2003. 51(2): p. 431-443.

[3] Nieman, G.W., J.R. Weertman, and R.W. Siegel, Scripta Metallurgica, 1989. 23(12): p. 2013-2018

[4] Dao, M., L. Lu, R.J. Asaro, J.T.M. De Hosson, and E. Ma, Acta Materialia, 2007. 55(12): p. 4041-4065.

[5] Suryanarayana, C., Advanced Engineering Materials, 2005. 7(11): p. 983-992.

[6] Koch, CC, R.O. Scattergood, K.L. Murty, JOM (2007) 59, p. 66-70.

[7] Raducanu, D et al., Journal of the Mechanical Behavior of Biomedical Materials 4 (2011) 1421.

[8] Chookajorn, T., Science 337 (2012) 951.

[9] R. Z. Valiev, N. A. Krasiinikov and N. K. Tsenev, Materials Science and Engineering A137 (1991) 35-40.

[10] R.Z.Valiev ,T.G.Langdon,Prog.Mater. Sci. 51 (2006) 881.

[11] R.Z.Valiev, R.K.Islamgaliev and I.V.Alexandrov, Prog Mater Sci 45 (2000) 103

[12] Gilman PS, Benjamin JS. Annu Rev Mater Sci 1983;13:279.

[13] Ma E, Atzmon M. Mater Chem Phys 1995;39:249.

[14] Suryanarayana C. Prog Mater Sci 2001;46:1.

[15] Libardi, S., Materials Science and Engineering A 478, (2008), 243.

[16] N. Tsuji, Y. Saito, S.-H. Lee, Y. Minamino, Adv. Eng. Mater. 5 (2003) 338–344.

[17] R.Z.Valiev, R.K.Islamgaliev and I.V.Alexandrov, Prog Mater Sci 45 (2000) 103

[18] D.G. Morris, M.A. Muñoz-Morris, Intermetallics 23, (2012) p. 169.

[19] A. Vorhauer, S. Kleber, R. Pippan, Mater. Sci. Eng. A 410–411, (2005) p. 281.

[20] G. Sha, K. Tugcu, X.Z. Liao, P.W. Trimby, M.Y. Murashkin, R.Z. Valiev, S.P. Ringer, Acta Mater. 63, (2014) p. 169.

[21] K. Regina Cardoso, M.A. Muñoz-Morris, K. Valdés León, D.G. Morris, Mater. Sci. Eng. A 587, (2013), p. 387.

[22] Aries Setiawan, Daisuke Terada, Nobuhiro Tsuji, Mater. Sci. Forums 403, (2010), p. 667.

[23] Martin, G. and P. Bellon, Driven alloys, in Solid State Physics - Advances in Research and Applications, Vol 50. 1997, Academic Press Inc: San Diego. p. 189-331.

[24] J. Ye, J.-wen Liu, R. a. Enrique, P. Bellon, Scripta Materialia **49** (2003) 969-975.

[25] P. Bellon and R. Averback, Scripta Materialia **49**, 921-925 (2003).

[26] C.C. Koch and J.D. Whittenberge, Intermetallics **4**, 339-355 (1996).

[27] C. Suryanarayana, Progress in Materials Science **46**, 1-184 (2001).

[28] F. Delogu, M. Pintore, S. Enzo, F. Cardellini, V. Contini, A. Montone, V. Rosato, Philosophical Magazine **76** (1997) 651-662.

[29] P. Bellon, R. Averback, Physical Review Letters **74** (1995) 1819-1822.

[30] S. Odunuga, Y. Li, P. Krasnochtchekov, P. Bellon, and R. Averback, Physical Review Letters **95**, 93-96 (2005).

[31] P. Bellon, R. Averback, S. Odunuga, Y. Li, P. Krasnochtchekov, and A. Caro, Physical Review Letters **99**, 1-4 (2007).

[32] D. Raabe, S. Ohsaki, and K. Hono, Acta Materialia **57**, 5254–5263 (2009).

[33] Y. Ashkenazy, N.Q. Vo, D. Schwen, R.S. Averback, and P. Bellon, Acta Materialia **60**, 984–993 (2012).

[34] S.N. Arshad, T.G. Lach, M. Pouryazdan, H. Hahn, P. Bellon, S.J. Dillon, and R.S. Averback, Scripta Materialia **68** (2013) 215-218.

[35] D. Schwen, M. Wang, R.S. Averback, and P. Bellon, J. Mater. Res. 28 (2013) p. 2687.

[36] M. Militzer, W.P. Sun, and J.J. Jonas, Acta Metallurgica Et Materialia **42**, 133–141 (1994).

[37] S.-H. Song, X.-M. Chen, and L.-Q. Weng, Materials Science and Engineering: A **528**, 7196–7199 (2011).

[38] T. Klassen, U. Herr, and R.S. Averback, Acta Materialia **45**, 2921-2930 (1997).

[39] S. Zghal, R. Twesten, F. Wu, P. Bellon, Acta Materialia **50** (2002) 4711-4726.

[40] F. Wu, P. Bellon, A. Melmed, and T. Lusby, Acta Materialia **49**, 453-461 (2001).

[41] F. Wu, D. Isheim, P. Bellon, and D. Seidman, Acta Materialia **54**, 2605-2613 (2006).

[42] M. Brocq, B. Radiguet, J.-M. Le Breton, F. Cuvilly, P. Pareige, and F. Legendre, Acta Materialia **58**, 1806–1814 (2010).

[43] A. Zhilyaev, T. Langdon, Progress in Materials Science 53 (2008) 893-979.

[44] R. Pippan, S. Scheriau, A. Hohenwarter, M. Hafok, Materials Science Forum 584-586 (2008) 16-21.

[45] R. Valiev, Nature Materials 3 (2004) 511-6.

[46] J.H. Han, D.Y. Kim, Acta Metall. Mater. 43 (1995) 3185-3188.

[47] A.L. Patterson, Physical Review 56 (1939) 978-982.

[48] I. M. Lifshitz and V. V. Slyozov: J. Exp. Theor. Physics 35 (1958) 479.

[49] I. M. Lifshitz and V. V. Slyozov: J. Phys. Chem. Solids 19 (1961) 35–50.

[50] Nhon Q. Vo, Samson Odunuga, Pascal Bellon, Robert S. Averback, Acta Mater. 57, (2009) p. 3012.

[51] L. Meng, S.P. Zhou, F.T. Yang, Q.J. Shen, M.S. Liu, Materials Characterization 47, (2001), p. 269.

[52] Soumya N., Kristopher C. M., Arun D., Smita G., Pushan A., Rajarshi B., J. Mater. Sci. 44, (2009), p. 3393.

[53] M. Cohen, Trans. Japan Inst. Metals 11, 145 (1970).

[54] Nakajima, T., Materials Transactions 47 (2006), 1098.

[55] W.P. Sun, M. Militzer, J.J. Jonas, Metallurgical Transactions A 23, (1992), p. 3013.

[56] X.L. He, Y.Y. Chu, J.J. Jonas, Acta Metallurgica 37, (1989), p. 2905.

[57] N. Q. Vo, R. S. Averback, P. Bellon, S. Odunuga, and A. Caro, Physical Review B 77, (2008), p. 134108.

[58] Lee, Seong-Hee; Lee, Chung-Hyo; Yoon, Suk-Ja; Han, Seung-Zeon; Lim, Cha-Yong, Journal of Nanoscience and Nanotechnology 7, (2007), p. 3872.

[59] Q. Li, Y.B. Xu, Z.H. Lai, L.T. Shen, Y.L. Bai, Mater. Sci. Eng. A 276, (2000), p. 250.

[60] J.A. Hines, K.S. Vecchio, Acta Mater. 45, (1997), p. 635.

[61] Seeger A., Mehrer H. Analysis of self-diffusion and equilibrium measurements, in: Seeger A., Schumacher D., Schilling W., Diehl J., (Eds.). Vacancies and Interstitials in Metals. New York: John Wiley & Sons, Inc.; 1970.

CHAPTER 6

CONCLUSIONS AND FUTURE DIRECTIONS

6.1. CONCLUSIONS

This dissertation research focused on understanding the underlying mechanisms and evolution of the microstructure during processing of bulk nanocomposite alloys by SPD [1,2,3] under controlled processing conditions. A simple model system of Cu-Ag has been investigated to better understand the mechanisms by which different steady states are achieved during forced chemical mixing of moderately immiscible alloys [4,5,6] and self-organization during thermodynamic relaxation [7,8,9]. The goal of this PhD thesis research was to experimentally study these two processes under controlled processing conditions and advance the science of processing of nanostructured metal alloys by SPD.

6.1.1. Demonstrating superdiffusive mixing during SPD in Cu-Ag

The results presented in this thesis experimentally support the prediction of a 'superdiffusive' model for shear induced mixing in the immiscible Cu-Ag system, where the dissolution rate of particles is controlled by the rate of dislocation glide across interfaces. Superdiffusive means the diffusivity increases with the pair separation distance and this derives from the fact that the probability for a dislocation to pass

between the two atoms, and cause their relative motion. This is proportional to their pair separation distance, which increases with time or strain during shear deformation. The Cu-Ag served as a model for tracking this behavior, since dislocations are anticipated to efficienctly cut interfaces in this system.. The consequence of super-diffusive mixing is that the critical strain to mix monodisperse spherical precipitates in the absence of thermal diffusion scales linearly with initial precipitate size. This behavior was confirmed by a combination of XRD, TEM, and APT, which all indicated that dislocation occurred at strains that were within a factor of two of what would be predicted by ideal superdiffusive mixing.

6.1.2. Quantifying strain rate and temperature effects during self-organization in Cu-Ag

The superdiffusive nature of mixing offered a direct rationalization for self-organization during shearing at elevated temperatures. The pair diffusion coefficient in superdiffusive mixing scales with the pair separation distance, however, the thermal diffusion is independent of pair separation distance. The competition between these two will be length scale dependent. At small length scales, thermal diffusion dominates and at large length scales shear mixing dominates. At low temperatures the length scale will approach that of a single atom and the system will tend to homogenize, and at high temperatures thermal diffusivity will dominate and the system will approach a state characteristic of pure thermal annealing. The competition between the two mechanisms under appropriate conditions is expected to result in a steady state length scale. If thermal

vacancy mediated diffusion is independent of strain rate, then it should be possible to control the microstructural length scale via either temperature or strain rate.

The strain required to reach steady-state was established and it was shown that the same steady state was reached via both mixing and coarsening mechanisms. The length scale of steady state compositional patterning is nearly independent of the shearing rate. The apparent activation energy associated with the steady-state microstructureal length scale was 0.39 eV. The results are rationalized based on the hypothesis that the thermal vacancy diffusivity is not strain rate independent. Assuming that the total number of excess vacancies generated is independent of strain rate, for equivalent strain, the results may be rationalized on the basis of accounting for the total number of vacancy mediated atomic jumps and shear induced atomic jumps. If the excess vacancy concentration significantly exceeds the equilibrium concentration and the vacancy sink density is equivalent (i.e. grain size, which is confirmed by the results), then the total number of vacancy mediated and shear induced atomic jumps will be equivalent regardless of strain rate. At the intermediate temperatures studied here, shear enhanced diffusion resulting from significant concentrations of non-equilibrium shear induced excess vacancies dominate the establishment of a steady state compositional patterning length scale. This results in the low apparent activation energy and the limited strain rate dependence of the particle size. It also accounts for the observation of shear enhanced coarsening, relative to thermal coarsening, observed at 400 ^{o}C and 6.25 s^{-1}.

The observed strain rate insensitivity helps explain why relatively consistent results may be achieved through ball milling in different laboratories under different conditions. The results also provide a useful quantitative framework for understanding

how to better control self-organization during SPD, in order to fabricate nanostructured alloys far from equilibrium.

6.1.3. Ball milling compared to HPT

An unknown factor in BM experiments is the total strain and strain rate experienced by the powders. Using the present study we can roughly estimate the magnitude of these parameters. It is found in the present study that a 10 μm Cu and Ag powders require about 5 hours of BM to fully mix them. The results in this chapter have shown that the strain to mix scale with particle radius with a proportionality constant ~ 5.5. This would correspond to an average strain rate in BM of ~1.5 s^{-1}. This is just an estimate since mixing by BM is approximately random, whereas, mixing during HPT is primarily via simple shear deformation.

6.2. FUTURE DIRECTIONS

6.2.1. Strain paths during mixing of particles

A related question during shear induced mixing is the strain paths the model systems follow to mix immiscible phases with low heats of mixing. For example, simple shear strain will elongate the particle in the direction of the shear but the occurrence and nature of instabilities during particle elongation, the degree of co-deformation, and the role of grain boundaries and triple lines are not well understood. In the preliminary experiments in this thesis, a Cu-Ag sample with the largest initial particle size ($R_{p,i}$ of 131

nm) was deformed at room temperature with strain ranging from an factor of 1 to few hundred. Both Cu and Ag thicknesses decrease within the strain range investigated. Interestingly, the solubility (~0.8 %) is constant during the thinning and break up of these layers. This suggests the limited intermixing during the inhomogeneous codeformation of the Cu and Ag. At small strains ($\varepsilon \sim 10$) the initially compact particles become distorted and irregular in shape possibly due to roughening of the Cu-Ag interface. Instability was observed in the strain range of 20 – 60 when Ag of mean length ~3500 nm breaks down to ~650 nm long fragments. Thus, this instability could very well be the very first instability during particle shearing. There could potentially be more instabilities at higher strains and it needs to be investigated further using advanced electron microscopy techniques and is one of the suggested future work of this thesis.

6.2.2. Mechanical properties appraching theoretical limits

Nanostructuring is attractive for developing new high-strength alloys with superior strength-to-weight ratios, which are inherently strong due to the high density of grain boundaries and interfaces [10,11,12]. Below a critical grain size, inverse Hall-Petch relation has been reported [13,14,15] which limits on how strong the nanostructured material can be.

This thesis has shown that by using the principles of forced chemical mixing and self-organization, a variety of microstructures can be obtained at nanometer length scales. For example, a complete solid solution, a completely phase-separated or an intermediate state (where fine second phase particles are present in addition to some solid solubility)

can potentially be fabricated by controlling the SPD conditions. Preliminary hardness data was collected to investigate the dependence of their mechanical properties on their microstructural features and length scales and is presented in Figure 6.1.

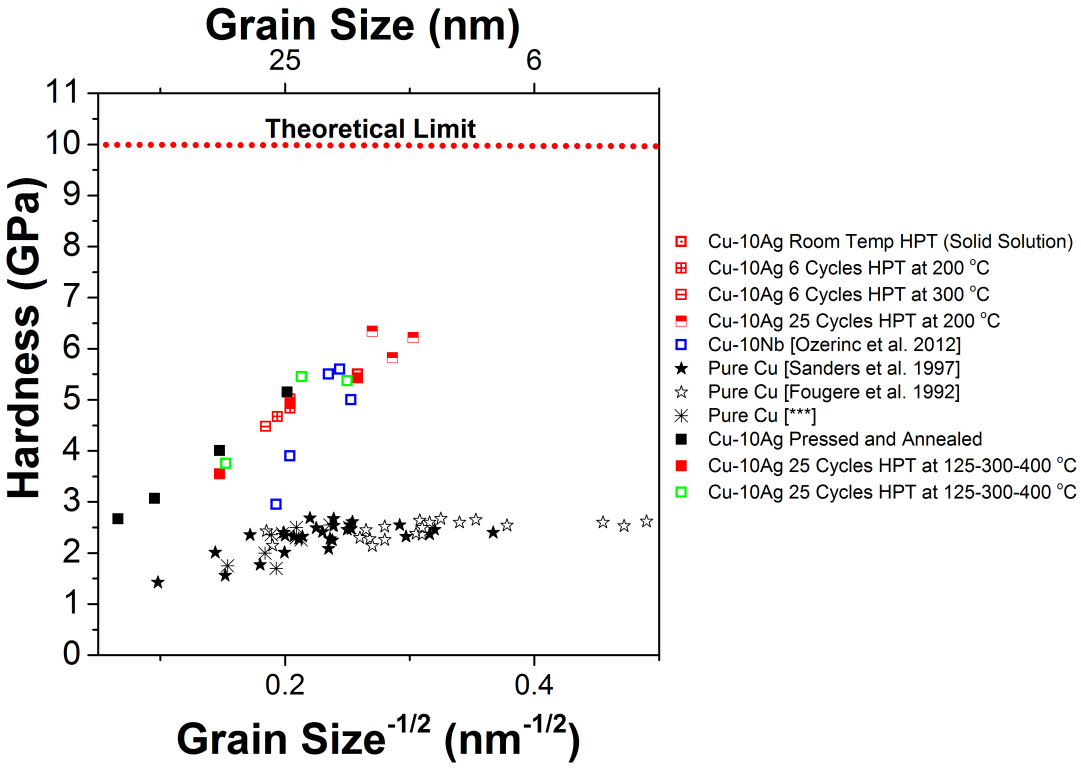

Figure 6.1. Hardness data of various samples processed by HPT at room and elevated temperatures in this dissertation research.

The first observation is that the hardness of all Cu-Ag samples is well defined by the Hall-Petch relationship and it approaches the theoretical limit of ~10 GPa [16,17]. In pure Cu, shown in Figure 6.1, inverse Hall-Petch has been reported. The presence of Ag in Cu extends this range down to 10 nm (the smallest grain size fabricated in this thesis) and there is no indication of breakdown of Hall-Petch relationship yet. The exact mechanism is unclear but it could be related to grain boundary strengthening caused by the solute atoms. Vo et al. [18] have suggested from MD simulations that softening is not

an intrinsic property of nanocrystalline metals, and that it can be suppressed by lowering the GB energy through various relaxation treatments. Solute segregation to GBs can reduce GB energies, and therefore should lead to hardening [19]. Nanoindentation experiments on nanocrystalline Cu-Nb and Cu-Fe systems [20] were in good agreement with the simulation predictions.

Amorphous materials have been investigated to explore hardness approaching theoretical limit. In one such study [21], it is shown than crystalline Cu/Zr multilayers soften at 10 nm grain size, whereas, Cu(crystalline)/Zr(amorphous) multilayers show higher peak hardness without softening. This is due to absence of dislocation activity in the amorphous layers. The fact that Hall-Petch relation doesn't breakdown in the Cu-Ag studied in this thesis down to scales of 10 nm motivates to further investigate such systems at even smaller length scales and understanding of the associated mechanisms could be interesting.

6.3. REFERENCES

[1] R. Z. Valiev, N. A. Krasiinikov and N. K. Tsenev, Materials Science and Engineering A137 (1991) 35-40.

[2] R.Z.Valiev ,T.G.Langdon,Prog.Mater. Sci. 51 (2006) 881.

[3] R.Z.Valiev, R.K.Islamgaliev and I.V.Alexandrov, Prog Mater Sci 45 (2000) 103

[4] C.C. Koch and J.D. Whittenberge, Intermetallics 4, 339-355 (1996).

[5] F. Delogu, M. Pintore, S. Enzo, F. Cardellini, V. Contini, A. Montone, V. Rosato, Philosophical Magazine 76 (1997) 651-662.

[6] P. Bellon, R. Averback, Physical Review Letters 74 (1995) 1819-1822.

[7] Martin, G. and P. Bellon, Driven alloys, in Solid State Physics - Advances in Research and Applications, Vol 50. 1997, Academic Press Inc: San Diego. p. 189-331.

[8] J. Ye, J.-wen Liu, R. a. Enrique, P. Bellon, Scripta Materialia 49 (2003) 969-975.

[9] P. Bellon and R. Averback, Scripta Materialia 49, 921-925 (2003).

[10] Schuh, C.A., T.G. Nieh, and H. Iwasaki, Acta Materialia, 2003. 51(2): p. 431-443.

[11] Nieman, G.W., J.R. Weertman, and R.W. Siegel, Scripta Metallurgica, 1989. 23(12): p. 2013-2018

[12] Dao, M., L. Lu, R.J. Asaro, J.T.M. De Hosson, and E. Ma, Acta Materialia, 2007. 55(12): p. 4041-4065.

[13] T.G. Nieh, J. Wadsworth, Scripta Metall. Mater, 25 (1991), p. 955

[14] V. Yamakov, D. Wolf, S.R. Phillpot, A.K. Mukherjee, H. Gleiter, Philosophical Magazine Letters 83 (2003) 385-393.

[15] G. Palumbo, S.J. Thorpe, K.T. Aust, Scripta Metall. Mater, 24 (1990), p. 1347

[16] Nhon Q. Vo, Robert S. Averback, Pascal Bellon, Alfredo Caro, Scripta Mater. 61, (2009), p. 76.

[17] M.A. Tschopp, D.L. McDowell, Appl. Phys. Lett. 90 (2007), p. 121916.

[18] N.Q. Vo, R.S. Averback, P. Bellon, A. Caro, Scripta Mater., 61 (2009), p. 76.

[19] N.Q. Vo, J. Schaefer, R.S. Averback, K. Albe, Y. Ashkenazy, P. Bellon, Scripta Mater. 65 (2011), p. 660.

[20] Sezer Özerinç, Kaiping Tai, Nhon Q. Vo, Pascal Bellon, Robert S. Averback, William P. King, Scripta Mater. 67, (2012), p. 720.

[21] J.Y. Zhang et al., Mater. Sci. and Eng. A 552 (2012) 392– 398.